Technische Universität München
Max-Planck-Institut für Biochemie
Abteilung für Molekulare Strukturbiologie

Strategies for cryo-electron tomography of the mycobacterial cell envelope and its pore proteins and functional studies of porin MspA from *Mycobacterium smegmatis*

Christian Werner Hoffmann

Vollständiger Abdruck der von der Fakultät für Chemie der Technischen Universität München zur
Erlangung des akademischen Grades eines Doktors der Naturwissenschaften
genehmigten Dissertation.

Vorsitzender:	Univ. – Prof. Dr. J. Buchner
Prüfer der Dissertation:	1. Hon. – Prof. Dr. W. Baumeister
	2. Univ. – Prof. Dr. S. Weinkauf
	3. Univ. – Prof. Dr. W. Liebl

Die Dissertation wurde am 28.04.2010 bei der Technischen Universität München eingereicht und durch die Fakultät für Chemie am 14.07.2010 angenommen.

A Table of contents

B Abbreviations

2D	Two-dimensional
3D	Three-dimensional
aa	Amino acid
ART	Algebraic reconstruction techniques
BCA	Bichinonic acid
BCG	Bacillus Calmette Guerin
BHI	Brain heart infusion
BSA	Bovine Serum Albumine
CCD	Charge coupled device
CCR	Combined polymerase chain reaction
CET	Cryo-electron tomography
Ch.	Chapter
C.	*Corynebacterium*
CMN	*Corynebacterium, Mycobacterium and Nocardia*
CTF	Contrast transfer function
Diph-PC	1,2-diphytanoyl-sn-glycero-3-phosphocholine
DMPC	1,2-dimyristoyl-sn-glycero-3-phosphocholine
DNA	Desoxyribonucleic acid
DPPC	1,2-dipalmitoyl-sn-glycero-3-phosphocholine
dsDNA	Double strand deoxyribonucleic acid
E.	*Escherichia*
EDTA	Ethylenediaminetetraacetic acid
EM	Electron microscope
ET	Electron tomography
FEG	Field emission gun
FIB	Focussed ion beam
Fig.	Figure
FSC	Fourrier shell correlation
GUV	Giant unilamellar vesicles
HEPES	2-(4-(2-Hydroxyethyl)-1-piperazine)-ethansulfonic acid
HIV	Human immunodeficiency virus
ITO	Indium tin oxide
λ	Wavelength
LB	Lysogeny broth
LN_2	Liquid nitrogen

MDR	Multi drug resistant
MOM	Mycobacterial outer membrane
M.	*Mycobacterium*
MspA	*Mycobacterium smegmatis* porin A
MTF	Modulation transfer function
MWCO	Molecular weight cutoff
N_2	Nitrogen
OD	Optical density
OPOE	Octyl polyoxyethylene
ORF	Open reading frame
PAA	Poly acrylamide
PAGE	Poly acrylamide gelelectrophoresis
PBS	Phosphate-buffered saline
PC	Phosphatidylcholine
PCR	Polymerase chain reaction
PSF	Point spread function
RNA	Ribonucleic acid
RT	Room temperature
SDS	Sodiumdodecylsulfate
SEM	Scanning electron microscope
SIRT	Simultaneous iterative reconstruction technique
SNR	Signal to noise ratio
ssDNA	Single strand desoxyribonucleic acid
ssRNA	Single strand ribonucleic acid
Tab.	Table
TB	Tuberculosis
TEM	Transmission electron microscope
TEMED	N,N,N‘,N‘-Tetramethylethylendiaminetriphosphate
Tris	Tris-(hydroxymethyl)aminoethane
v/v	Volume per volume
WHO	World Health Organization
wt	Wildtype
w/v	Weight per volume
XDR	Extensively drug resistant

Units

A	Ampere
Å	Ångström
bp	Base pair
°C	Degree Celsius
Da	Dalton
e^-	Electron
F	Farad
g	Gram
g	Acceleration of gravity
h	Hour
Hz	Hertz
K	Kelvin
L	Liter
m	Meter
M	Molar
min	Minute
Ω	Ohm
pH	Power of hydrogen
sec	second
S	Siemens
V	Volt

Nucleotides

A	Adenosine
C	Cytosine
G	Guanosine
T	Thymidine

Dimensions

G	giga (10^9)
M	mega (10^6)
k	kilo (10^3)
m	milli (10^{-3})
µ	micro (10^{-6})
n	nano (10^{-9})
p	pico (10^{-12})

C Zusammenfassung

Kryo-Elektronentomographie (CET) in Kombination mit 3D Klassifizierung und Mittelung ist eine leistungsfähige Methode zur Analyse der Struktur und Interaktion von makromolekularen Komplexen in ihrer natürlichen Umgebung. Am Beispiel des Porins MspA aus *Mycobcaterium smegmatis* zeigt diese Arbeit mit welchem Ergebnis Kryopräparation, adaptierte Datenakquisition sowie die fortentwickelte Analyse und Rekonstruktion der Daten für die *in situ* Untersuchung von Membranproteinen mittlerer Größe angewendet werden kann. Neben den strukturellen Aspekten werden außerdem funktionelle Eigenschaften von membran-eingebettetem MspA untersucht.

Zunächst galt das Interesse der natürlichen Umgebung von MspA, der Klärung der *in situ* Struktur der mycobakteriellen Zellhülle. Bis dahin bestehende Modelle nahmen als äußere Membran eine dicke asymmetrische Doppelschicht an, welche sich jedoch nicht mit der Kristallstruktur von MspA in Einklang bringen ließ. CET sowie die Untersuchung von ultradünnen, vitrifizierten Kryoschnitten von *M. smegmatis*, *Mycobacterium bovis* BCG und *Corynebacterium glutamicum* enthüllten die native Organisation der Zellwand und identifizierten die äußere Schicht als morphologisch symmetrischen Bilayer. Verbesserte Modelle der mycobakteriellen äußeren Membran werden vorgeschlagen und diskutiert.

Auf Grund der Abmessungen von mycobakteriellen Zellen ist das Verringern der Probendicke unumgänglich wenn MspA mittels CET *in situ* analysiert werden soll. Kompressionsartefakte schränken die Nutzbarkeit von Kryoschnitten für hochauflösende Tomographie erheblich ein. Ein alternativer Ansatz ist die Verwendung eines fokussierten Ionenstrahls (FIB) um die eingefrorenen Proben durch Ätzungauszudünnen. Verschiedene ‚Milling‘ Geometrien wurden getestet, wobei sich eine Keilform als am besten geeignet herausstellte. 3D Rekonstruktionen von entsprechend präparierten *M. smegmatis* Zellen zeigen eine deformationsfreie Erhaltung der Struktur und einen bisher unerreichten Grad an Details. ‚FIB-Milling‘ erweist sich als vielversprechende Methode um die für verlässliche *in situ* Studien mittels CET benötige hohe Qualität der Probenpräparation zu erreichen.

Für die Entwicklung eines Datenaufnahmeschemas welches letzlich auf die Abbildung von Membranproteinen in ihrem natürlichen Kontext angewendet werden kann, wurde MspA in die Membran von definierten Lipidvesikeln rekonstitutiert. Eine neue Methode zur Korrektur der Kontrasttransferfunktion (CTF) in Projektionen von Kippserien verbesserte die durch Mittelung von Subtomogrammen erreichte Auflösung erheblich. Der membrandurchspannende Bereich von MspA ist deutlich aufgelöst und kann von der umgebenden Lipiddoppelschicht unterschieden werden. Die Ergebnisse stellen eine methodische Erweiterung der Kryo-Elektronentomographie dar, welche generell für eine Analyse von Membranproteinen eingesetzt werden kann.

Die Struktur von MspA unterscheidet sich von der klassischer Porine und ist wegen ihrer hohen Symmetrie besonders für die Untersuchung funktioneller Aspekte der Ionen- und Substrattranslokation geeignet. Die Auswirkungen geladener Reste im Inneren der Pore und der periplasmatischen Domäne wurden durch Konstruktion entsprechender Mutanten anhand von Leitfähigkeitsmessungen in planaren Lipidmembranen analysiert. Die Entfernung der Ladungen reduzierte die Eigenschaft des spannungsabhängigen Schließens deutlich, während die zusätzliche Deletion des periplasmatischen Loops die Frequenz von Schließ- und Öffnungsereignissen wieder erhöhte. Die Ergebnisse werden hinsichtlich des Schließmechanismus und gegenwärtig vorgeschlagener biotechnischer Anwendungen diskutiert.

D Summary

Cryo-electron tomography (CET) combined with 3D image classification and averaging becomes an increasingly powerful method aiming at the analysis of the structure and interactions of macromolecular complexes in their natural context. By means of the porin MspA from *Mycobacterium smegmatis* this study evaluates to what extent cryopreparation, adapted data acquisition and further developed data analysis and reconstruction can be applied to the *in situ* analysis of medium sized membrane proteins. Furthermore, besides the structural investigations, functional properties of membrane-embedded MspA are assessed.

The first point of interest was the natural environment of MspA, the *in situ* structure of the mycobacterial cell envelope. The models at that time assumed the outer membrane to be a thick assymetrical bilayer, an arrangement which did not fully accommodate to the crystal structure of MspA. CET and the investigation of ultrathin frozen-hydrated cryosections of *M. smegmatis*, *Mycobacterium bovis* BCG and *Corynebacterium glutamicum* revealed the native organization of the cell envelope and identified the outermost layer as a morphologically symmetrical bilayer. Revised models of the structure of the mycobacterial outer membrane are proposed and discussed.

The dimensions of mycobacterial cells make thinning a prerequisite to analyze MspA *in situ* by CET. Compression artifacts severely hamper the usability of cryosections for high resolution tomography. An alternative approach is the use of focused ion beam (FIB) instrumentation. Different milling approaches were tested resulting in a wedge-shaped preparation as the most useful. 3D reconstructions of accordingly prepared *M. smegmatis* cells indicate a deformation-free structural preservation and a so far unmatched level of detail. Sample preparation by FIB-milling holds great promise to achieve the high quality which is needed for reliable *in situ* studies by CET.

To develop a data acquisition scheme aiming at resolution of membrane proteins in their natural context by CET, purified MspA was reconstituted into the membrane of defined lipid vesicles. A novel method for correction of the contrast transfer function in projections of tilt series significantly improved the resolution of the structure as obtained by sub-tomogram alignment and averaging. The transmembrane domain of MspA is clearly resolved and distinguishable from the surrounding lipid bilayer. The results present a methodical extension of CET that can be adapted to the analysis of membrane proteins in general.

The structure of MspA differs from those of classical porins and, due to its high symmetry, is particularly suited for the investigation of functional aspects of ion- and substrate translocation. The impact of charged amino acids inside the pore and of the periplasmic domain was assessed by constructing appropriate mutants and analyzing their conductivity behavior in planar lipid bilayers. Removing the charges resulted in pores that remained stably ‚open’ up to higher voltages compared to the wild type, while additional deletion of the periplasmic loop increased the frequency of closing- and opening events again. The results are discussed with regard to the closing mechanism and currently suggested biotechnical applications.

1 Introduction

1.1 The genus *Mycobacterium*

1.1.1 Taxonomy

Mycobacteria are aerophilic bacteria with a high GC content of up to 70%. The bacteria are rod-shaped with uneven formed branched cells and show mostly rough colony morphology. They are non-motile organisms and are characterized by their acid-fastness. Taxonomically, mycobacteria belong to the genus *Mycobacterium*, which is the only genus within the family of *Mycobacteriaceae* in the order *Actinomycetales*. *Actinomycetes* include the members of the *Corynebacterium*, *Mycobacterium* and *Nocardia* (CMN) group and are the only microorganisms able to synthesize mycolic acids (Rastogi et al., 2001). Among the respective genera the length of the mycolic acids varies; mycobacteria synthesize the longest molecules with up to 90 carbon atoms (Barry et al., 1998). These extraordinarily long fatty acids are held responsible for the acid-fastness of the bacteria. According to 16S ribosomal RNA sequence analyses, mycobacteria are members of the gram-positive branch of Bacteria (Pitulle et al., 1992). However, a genome-based phylogeny analysis suggests that mycobacteria are in closer evolutionary neighborhood to gram-negative bacteria (Fu and Fu-Liu, 2002), what is also supported by 12S ribosomal protein sequence analysis (Gupta, 1998). The species of *Mycobacterium* (Hartmans et al., 2004) are phylogenetically separated in slow- and fast-growing bacteria (Rogall et al., 1990). Fast-growing species with generation times of less than 5 hours are generally non-pathogenic and saprophytic soil or water dwellers such as *Mycobacterium smegmatis*, *M. phlei* or *M. chelonae*. Slow-growing strains have generation times of 20 hours and longer and include many pathogens known to cause serious diseases in mammals, especially *M. tuberculosis*, the causative agent of tuberculosis (TB) and *M. leprae*, the agent of leprosy.

Figure 1: Morphology of *M. smegmatis*. *Left*: false colored scanning electron micrograph of *M. smegmatis* cells. *Center*: typical colony morphology of *M. smegmatis* mc^{2}155 grown on 7H10 solid media. *Right*: biofilm formation of *M. smegmatis* mc^{2}155 growing on liquid.

1.1.2 Medical relevance of mycobacteria

Since long before their discovery and characterization by Robert Koch in 1882 (Koch, 1882) mycobacteria pose a major health burden to mankind. There were an estimated nine million incidences of TB in 2004 with two million people dying due to an infection with *M. tuberculosis* per year (WHO, 2009). According to a study of the World Health Organization (WHO), one-third of the world's population is infected with *M. tuberculosis* with an infection occurring every second, and a predicted number of more than one billion new infections by 2020 (WHO, 2006). Infections often remain unrecognized as the bacteria are capable of adapting to prolonged periods of dormancy in tissues (Honer zu Bentrup and Russell, 2001; Parrish et al., 1998), leading to an asymptomatic infection, the so called latent disease (Gupta and Chatterji, 2005). The ability of *M. tuberculosis* to remain dormant without any obvious symptoms encapsulated in granulomas in the host for years (Russell, 2001) is likely based on the ability to shift down into a non-replicating state (Wayne and Hayes, 1996). Individuals harboring latent *M. tuberculosis* have a 5 to 10% risk to develop active disease at some time during their life when the immune system is perturbed by ageing, malnutrition or other diseases (Gupta and Chatterji, 2005), while this risk is highly increased after the onset of HIV (Parrish et al., 1998).

Due to its special architecture, the mycobacterial cell wall is a very effective permeability barrier. Diffusion of cephaloridin, a hydrophilic β-lactam antibiotic, through the cell wall of mycobacteria is 100 to 1000 times slower than through the cell wall of *Escherichia coli* (Stephan et al., 2005). Thus, treatment of mycobacterial infections is difficult, since the special cell wall renders the bacteria intrinsically resistant to a multitude of antibiotics (Nikaido, 1994). Fully susceptible tuberculosis is curable with a consequent treatment with up to four different drugs for six months (Espinal et al., 2000). This led to a decrease of the disease in the industrialized countries and consequently less new infections. However, by an increased immigration from countries with bad healthcare, new infections reoccur also in industrialized nations (Rieder et al., 1994). The problem is enhanced by a raising number of multidrug-resistant (MDR) strains (Bleed, 2001) not responding to the first-line antibiotics rifampicin and isoniazid. In 2007, more than 20,000 verified cases of MDR-TB were reported worldwide (WHO, 2009). Since several years, the emergence of extensively drug-resistant (XDR) strains is reported. Those bacteria are not only resistant against rifampicin and isoniazid but also lost susceptibility against at least three classes of second-line drugs. Therapy of XDR-TB is extremely tedious and complicated and raises concerns of a future epidemic of virtually untreatable tuberculosis (Lawn and Wilkinson, 2006).

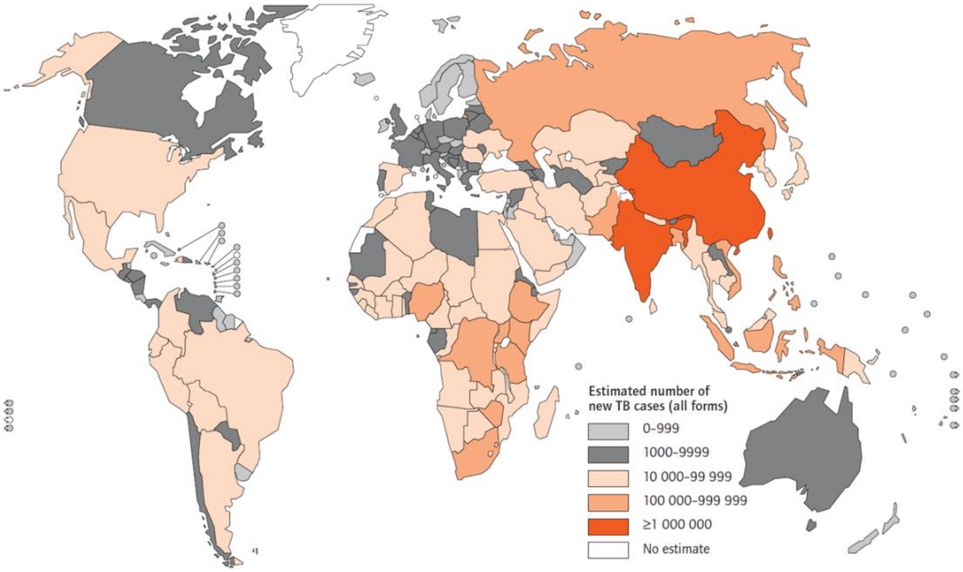

Figure 2: Estimated number of new tuberculosis cases, 2007, by country (WHO, 2009).

1.2 The global architecture of the mycobacterial cell envelope

The cell wall is an inevitable structure for mycobacteria because inhibition of the production of some of its constituents, e.g., mycolic acids and arabinogalactan, kills the cells. The cell envelope and its constituents control the transfer of materials into and out of the mycobacterium. A major discovery of the last decade has been the demonstration of the notably low permeability of mycobacteria to nutrients and antibacterial drugs, which slows down the growth of mycobacteria and impedes the treatment of mycobacterial infections. The permeability of mycobacterial cell walls is 10- to 100-fold lower than that of the notably ‘impermeable’ *Pseudomonas aeruginosa* (Jarlier and Nikaido, 1990). This property is explained by the special structure and composition of the cell envelope of mycobacteria and related microorganisms of the CMN-group. There is a controversial discussion about the affiliation of mycobacteria to gram-positive or gram-negative bacteria (Fu and Fu-Liu, 2002; Pitulle et al., 1992). Importantly, the chemical nature of the envelope is different from those of both groups of bacteria; the lipid content of the cell envelope of mycobacteria represents up to 40% of the cell dry mass, compared to less than 5% in other gram-positive bacteria and only 10% in gram-negative bacteria (Brennan and Goren, 1979). The abundance of lipids is also reflected in the genome of mycobacteria: 225 genes of *M. tuberculosis* are involved in lipid metabolism, compared to 50 genes for *E. coli*, while both bacteria have genomes of comparable size (Cole et al., 1998). Among the enormous variety of these lipids (Brennan and Nikaido, 1995) are extraordinary long fatty acids, the mycolic acids (Fig. 3 *A*). They are a typical feature of the actinomycetes and account for 30% to 40% of the cell envelope mass (Rastogi et al., 2001). The mycolic acids are covalently linked to peptidoglycan via an arabinogalactan polymer. In a typical arrangement, the peptidoglycan network is substituted by linear galactan molecules, which bear several branched arabinose chains. These end in four arabinose dimers, each forming the head group for two mycolic acid molecules (Crick et al., 2001). This huge mycolic acid-arabinogalactan-peptidoglycan polymer is arranged to form a hydrophobic layer with other lipids in addition to the cytoplasmic membrane (Barry et al., 1998; Daffe and Draper, 1998; Nikaido et al., 1993). The unique structure of the cell wall as well as the location and the arrangement of its constituents in mycobacteria is part of numerous studies, but what still remains unclear is the architecture of the outermost layer of this bulwark. In current models a layer of so called ‘extractable’ lipids is overlying the mycolic acids

(Liu et al., 1995; Minnikin, 1991; Minnikin et al., 1982; Nikaido et al., 1993), thus forming an asymmetrical outer ‘membrane’. The outer layer consists of a diversity of lipids, e.g., trehalose dimycolate, phthiocerol dimycocerosates, lipooligosaccharides, sulpholipids, glycero phospholipids and numerous others (Ortalo-Magne et al., 1996). According to Dmitriev and coworkers, the mycolic acids underneath are packed parallel and dense and are aligned perpendicular to the cytoplasmic membrane (2000). Conventional electron microscopical (EM) preparations of mycobacterial cell walls revealed a thickness of approximately 10 nm for this arrangement; thus, this outer ‘membrane’ would be much thicker than the cytoplasmic membrane (Brennan and Nikaido, 1995). The cytoplasmic membrane of *M. smegmatis* is mainly composed of cardiolipin, phosphatidylinositol and phosphatidylethanolamin (Jackson et al., 2000). An overall view of the mycobacterial envelope is illustrated in Figure 3 *B*, which shows a thin section transmission electron microscopical (TEM) image of a chemically fixed and dehydrated *M. smegmatis* cell (Etienne et al., 2005) and provides interpretation of the electron microscopic image. This thin section is representative of what is obtained by this technique with other mycobacterial species, including pathogenic strains, whereas the mycobacterial cell wall appears as a multilayered structure. However, sparse information is available about the ‘native’ structure of the outer layer. This is due to the fact that the various preparation techniques use solvents that may extract more or less material. In addition, dehydration of formerly hydrated cells affects the structure by shrinkage and distortion. For instance, in ultrathin sectioning, the water in the fixed specimen is exchanged by solvents, causing collapse of structures that cannot be cross-linked by fixatives, notably carbohydrates, which are important components of the mycobacterial envelope (Daffe and Draper, 1998). Although the interpretation of microscopic data is still speculative in detail, it is well established that:

- Mycobacteria are surrounded by a complex cell wall made of carbohydrates and lipids.
- The wall possesses a fundamental, covalently linked ‘cell-wall skeleton’ associated with a great variety of non-covalently linked lipids and glycolipids (Daffe and Draper, 1998).
- Although not explicitly demonstrated, mycobacteria should possess a compartment analogous to the periplasmic space in gram-negative bacteria (Daffe and Draper, 1998).
- Little is known about the architecture of the outer layer.

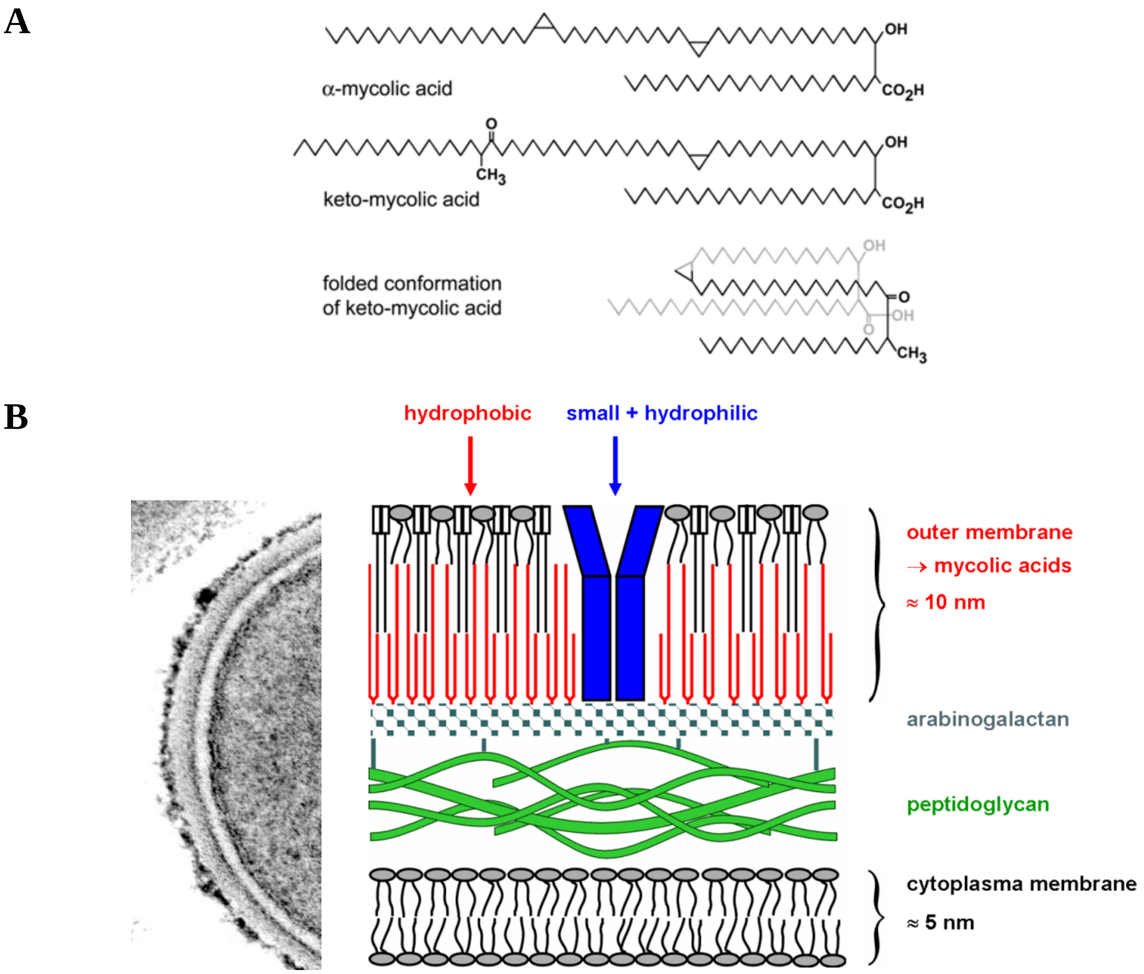

Figure 3: A. Schematical structure of the mycolic acids in an elongated and folded conformation. (Villeneuve et al., 2005; Villeneuve et al., 2007; Watanabe et al., 2002) **B. Electron micrograph and schematic model of the cell envelope of mycobacteria.** *Left*: ultrathin section of *M. smegmatis* fixed with glutaraldehyde and lysine buffer containing ruthenium red and postfixed with osmium tetroxide; bacteria were suspended in uranyl acetate, and cells were embedded in agar before dehydration with ethanol (Etienne et al., 2005). *Right*: schematic representation of the mycobacterial cell envelope, based on Minnikin (1991). The inner leaflet of the outer membrane is composed of mycolic acids, wich are covalently bound to the arabinogalactan-peptidoglycan polymer via their head groups. The outer leaflet is formed by a variety of extractable lipids (Ortalo-Magne et al., 1996).

The rigid character of the cell wall creates an efficient permeability barrier which protects mycobacteria from environmental stress and limits access of many antibiotics. However, the bacteria need to maintain an adequate nutrient supply. Hydrophobic compounds can traverse the outer ‘membrane’ directly across the lipid bilayer, whereas hydrophilic molecules require a special pathway. Transmembrane channels span the membrane and provide water-filled pores for passive diffusion of hydrophilic nutrients and waste products (Niederweis, 2003). They were first described by Nakae in 1976 and named porins (1976).

1.3 The porin MspA of *Mycobacterium smegmatis*

In 1990, Jarlier and Nikaido postulated that there must be a hydrophilic channel in the outer ‘membrane‘ of mycobacteria to facilitate diffusion of small, lipophobic molecules (1990). Two years later, Trias and coworkers analyzed the diffusion of sugars into lipid vesicles by using a cell wall extract from *Mycobacterium chelonae* (1992). They purified a 59 kDa protein, which showed channel activity in lipid bilayer experiments. This was the first description of a mycobacterial porin. In *M. tuberculosis,* very few proteins of the outer membrane have been identified to date. OmpATb was discovered as a protein with channel- forming properties and was suggested to be a porin of *M. tuberculosis* (Raynaud et al., 2002). Though, its function as a porin was put into question shortly after (Niederweis, 2003). Rv1698 was also identified as an outer membrane protein with pore-forming activity (Siroy et al., 2008), however, its physiological function in *M. tuberculosis* still needs to be clarified.

Unlike the rare knowledge about porins in *M. tuberculosis*, they are well analyzed in *M. smegmatis*. The channel-forming characteristics of a crude cell wall extract were examined in lipid bilayer experiments (Trias and Benz, 1994). A few years later, a 160 kDa protein was purified from $CHCl_3$/MeOH-extracts of *M. smegmatis* cells, which showed very high channel-forming activity with a single channel conductivity of 4.6 nS in 1 M KCl (Niederweis et al., 1999). The respective gene was named *mspA* (*<u>M</u>ycobacterium <u>s</u>megmatis* <u>p</u>orin <u>A</u>) and encodes a 184 amino acid protein plus an N-terminal signal sequence. Oligomeric MspA is extremely stable against high temperatures, organic solvents and extreme pH conditions, unsurpassed by any other porin known to date, and was shown to be cation selective (Heinz et al., 2003a). An *mspA* deletion mutant was constructed to study the porin’s function *in vivo*.

Deletion of the gene reduced the cell wall permeability for cephaloridine and glucose nine- and four-fold, respectively (Stahl et al., 2001), and the generation time in 7H9 medium was increased from 3.3 to 4.3 hours (Stephan et al., 2005).

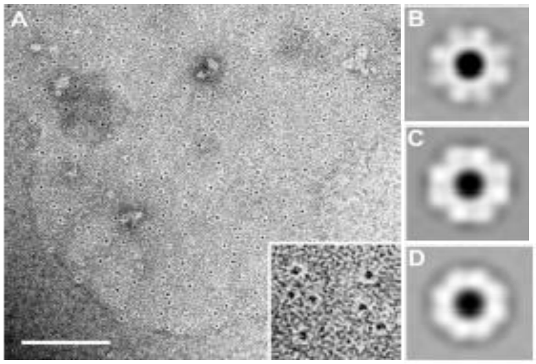

Figure 4: Electron microscopy of MspA (Engelhardt et al., 2002). **A.** An isolated cell wall fragment of *M. smegmatis* was negatively stained with uranyl acetate. Pores in the cell wall are filled with the stain and appear as black dots surrounded by a bright ring indicating the pore protein. The inset represents an enlarged area of 50 nm in size. (Scale bar: 100 nm.) **B. – D.** Averages of porin complexes extracted from images of negatively stained cell wall fragments.

Furthermore, detergent extracts exhibited a significantly lower porin activity in lipid bilayer experiments and, according to electron microscopic analysis, contained about fourfold less porin than extracts of the wild-type (Engelhardt et al., 2002). These studies showed that MspA is the major porin of *M. smegmatis*, and it was also the first experimental evidence that porins limit the uptake of hydrophilic compounds (Stahl et al., 2001; Wolschendorf et al., 2007). Electron microscopy also revealed that the outer membrane of *M. smegmatis* contains about 1000 protein pores per μm^2, which are about 50-fold fewer pores than in gram-negative bacteria (Engelhardt et al., 2002). MspA has three paralogues in *M. smegmatis*, named MspB, MspC and MspD that differ from the mature MspA protein in only 2, 4 and 18 amino acids, respectively. Their expression and functionality as porins was demonstrated recently, whereas *mspB* and *mspD* seem to act as backup porins as their expression is activated only upon deletion of *mspA* and *mspC* (Stephan et al., 2005). Consecutive deletions of the corresponding porin genes decreased the permeability of the cell wall and increased the resistance towards hydrophilic antibiotics (Stephan et al., 2004a; Stephan et al., 2004b). Furthermore, sequence comparisons with *mspA* identified one orthologue in *M. chelonae* and four in *Mycobacterium. phlei* (Niederweis, 2003).

In 2004, Faller and colleagues succeeded in solving the X-ray crystal structure of MspA (2004). This report revealed an unusual porin structure that differs fundamentally from trimeric porins of gram-negative bacteria. MspA consists of eight identical monomers forming a goblet with one central hydrophilic pore (Fig. 5). It has a height of 96 Å, an outer diameter of 88 Å (widest area) to 49 Å (stem β-barrel) and a diameter of the pore that ranges from 48 Å to 10 Å at the ‘eyelet’, the constriction zone at the bottom of the pore. This zone is composed of a double ring of aspartic acids, with each monomer contributing two aspartic acids, D90 and D91. These might be responsible for the cation selectivity of MspA (Hoffmann, 2005). Interestingly, this structure doesn’t accommodate the current models of the mycobacterial cell wall. The model assumes a thickness of 10 nm for the outer cell wall layer, implying that MspA would be buried completely in order to span the ‘membrane’. In porins of gram-negative bacteria, the membrane-spanning domain consists of a central belt of non-polar residues bordered by girdles of aromatic amino acids with a vertical separation of 2 - 2.5 nm (Cowan et al., 1992; Schulz, 1993). It has been suggested that these aromatic residues are especially adapted to accommodate the abrupt change of the dielectric properties at the acyl-water interface (Cowan et al., 1992), to shield the porin against slow membrane movements (Schulz, 1993), and to mechanically stabilize the protein (Kreusch and Schulz, 1994). Several aromatic surface residues were identified in MspA which are oriented perpendicular to the ‘bilayer’ plane and may in principle provide the functions of aromatic girdles as discussed above. Figure 5 *B* shows that the distance between the uppermost and the lowermost of these girdles is only approximately 7.1 nm. Assuming that the protein would be embedded completely, as implemented by the current model for the mycobacterial cell wall, this would result in a ‘hydrophilic’ mismatch. Furthermore, *in vivo* labeling experiments showed that residues between the aromatic girdles are protected from the hydrophilic label whereas the region outside is accessible (Fig 5 *B*; (Mahfoud et al., 2006)).

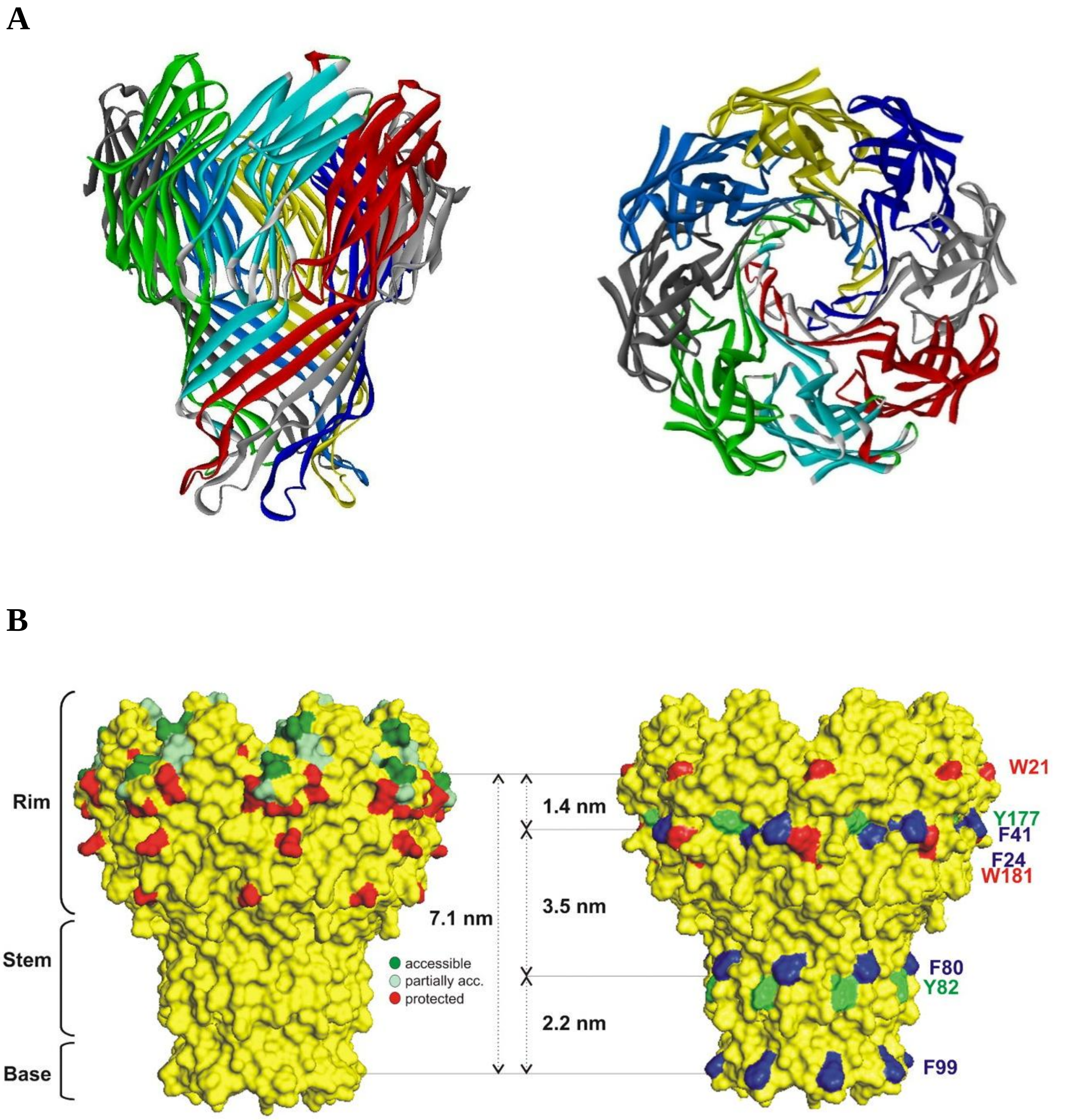

Figure 5: A. Structure of the octameric porin MspA from *M. smegmatis*. Each monomer is shown in a different color. *Left*: Side view of MspA, which would be surrounded horizontally by the outer membrane. The upside is extracellular, the downside ends in the periplasm. The goblet consists of a thick rim at the top, a β-barrel forms the stem in the middle and the base at the bottom contains the periplasmic loops. *Right*: Top view of MspA. The single channel is formed in the center of the octamer. **B. Membrane topology of MspA as defined by surface labeling of single cysteines** (Mahfoud et al., 2006). The left side of the figure shows a surface model of the MspA porin to visualize the protection of surface cysteines against biotinylation *in vivo*. Residues in *dark* and *light green* have protection values less than 30% and 65%, respectively, when compared with biotinylation *in vitro* and are defined as accessible. Residues in *red* have protection values of more than 80% and are considered as inaccessible. The right side of the figure shows surface-exposed aromatic residues of MspA. Tryptophans are colored *red*, tyrosines are colored *green*, and phenylalanines are colored *blue*.

1.4 Aim of the thesis

The porin MspA is currently the only protein of the mycobacterial cell wall whose function has been investigated *in vitro* and *in vivo*. Despite a number of studies it has remained unclear how the natural environment of MspA is organized. The major reason is that classical methods of electron microscopy have failed to preserve the bacterial cell envelope in its natural morphology and that it has not been possible to image membrane proteins in 3D *in situ*.

The aim of this thesis is to evaluate to what extend cryopreparation of mycobacterial cells and MspA, cryo-electron microscopy, and appropriate data analysis and reconstruction can be applied to investigate MspA and its natural environment *in situ*.

The following tasks should be executed:

- Structural analysis and clarification of the *in situ* structure of the mycobacterial cell envelope by means of cryo-electron tomography.
- Evaluation of the applicability of cryosectioning and FIB-preparation for cryo-electron microscopy of intact cells.
- Reconstitution of MspA in defined lipid membranes (vesicles) to work out and develop a data-acquisition scheme for cryo-electron tomography, aiming at resolving MspA *in situ* as a model for membrane proteins at molecular resolution.

MspA provides a particular suited structure to investigate functional aspects of ion and substrate translocation. In this study, a set of mutant proteins are produced that should give clues as to the understanding of voltage-depending gating of MspA.

2 Cryo-electron microscopy and tomography

Cryo-electron tomography (CET) combines the resolving power of the electron microscope with three-dimensional image reconstruction (Fig. 7 *A*) but with an important difference to conventional electron microscopy of biological samples: the preservation of the specimen is by rapid freezing. Avoiding crystallization of the water is mandatory for cryo-preparations, since ice crystals can destroy the native structure of macromolecules (or cells) and would cause strong anisotropic electron diffraction at the crystal lattice. Conversion of water into a solid state (vitreous water) for cryo-EM serves two major purposes: first, consistent with the goal of plastic-embedding, it allows the specimen to be introduced into the vacuum environment of the microscope without evaporation, and second, since biological specimens are predominantly aqueous, this ‘frozen-hydrated’ mode of preservation is much more likely to resemble the native state. In addition to avoiding substitution artifacts by organic solvents and the infiltration with plastic resin, the chemical fixatives and heavy metal stains used in conventional electron microscopy are also omitted (Fig. 6). Cryo-electron microscopy was introduced in the 1970s (Dubochet et al., 1988; Taylor and Glaeser, 1974) and has widely replaced or at least complemented the conventional preparation techniques.

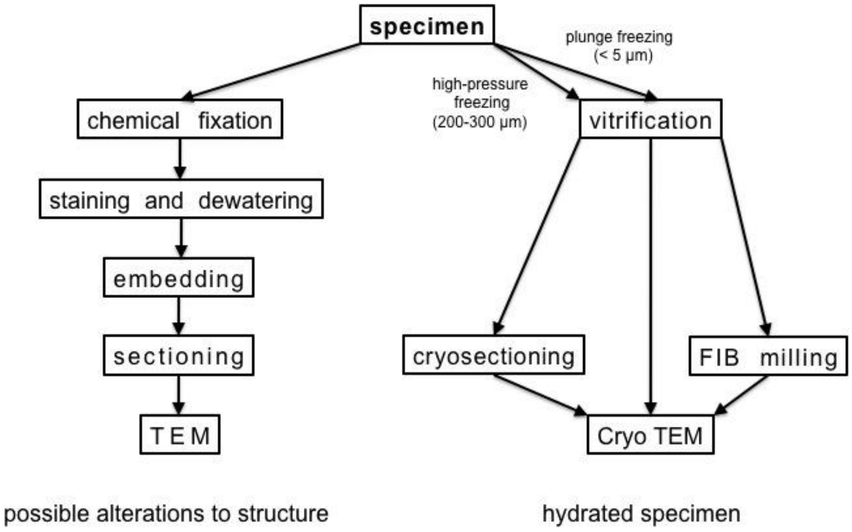

Figure 6: Conventional preparation techniques vs. cryo-preparation.

The tomographical acquisition, i.e. the projection of an object in the TEM under different angles, corresponds, according to the *projection slice theorem*, to the 'filling' with information of different tilt-planes in Fourier space (Crowther et al., 1970). With finite angular increments a continuous transfer of structural information is expected only below a frequency k_C (*Crowther criterion*), beyond that will be gaps in frequency space (Fig. 7 *B*). In addition, owing to limitations of the sample holders and thus a limited tilt range, the unsampled region, the so called *missing wedge*, is completely void of information (Fig. 7 *C*, *left*). Smaller tilt increments, higher tiltangles, and recording of a second tiltseries of the same specimen, rotated by 90° in plane ('dual-axis' tomography; Fig 7 *C*, *right*; (Mastronarde, 1997; Penczek et al., 1995)) come closer to the ideal continuous sampling of the Fourier space. However, to avoid radiation damage of the sample, it is important that the total electron dose over a complete tilt series does not exceed approx. 50 to 100 $e^-/Å^2$ (McEwen et al., 1995).

The method for 3D reconstruction used in this work is *weighted backprojection* (WBP) (Radermacher et al., 1986). The basic mathematical operation of the backprojection of 2D images into a 3D volume approximates an inverse Radon-transform (Radon, 1917). Weighting of the projections is necessary because of the anisotropic data transfer in frequency space. As shown schematically in Figure 7 *B*, the overlapping information below the frequency k_C would lead to an overrepresentation of low frequency areas and thus lead to a 'smeared' image of the object (Fig. 7 *D*). This behavior of the density in Fourier space is described by the point spread function $1/r^*$, with r^* being the distance from the center in frequency space. To get a realistic weighting of the individual frequencies in the 3D reconstruction, the projections are weighted in Fourier space, perpendicular to the direction of the tilt axis with the inverse of the point spread function, the norm function of r^* before backprojection. Thus, high frequencies get considerably more 'weight'. This kind of weighting is called analytic. For exact weighting, a cylindrical or spherical shape is approximated for the object to be reconstructed and the sampling density in Fourier space is calculated (Harauz and van Heel, 1986; Hoppe and Hegerl, 1980). However, this requires an object diameter, because the form function, i.e. its Fourier transform, has to be approximated. Alternatives to the WPB are algebraic methods for iterative optimization of the reconstruction (e.g., *simultaneous iterative reconstruction techniques*, SIRT (Lakshminarayanan and Lent, 1979)). Here, the weighting problem and the approximation of the form function can be surpassed.

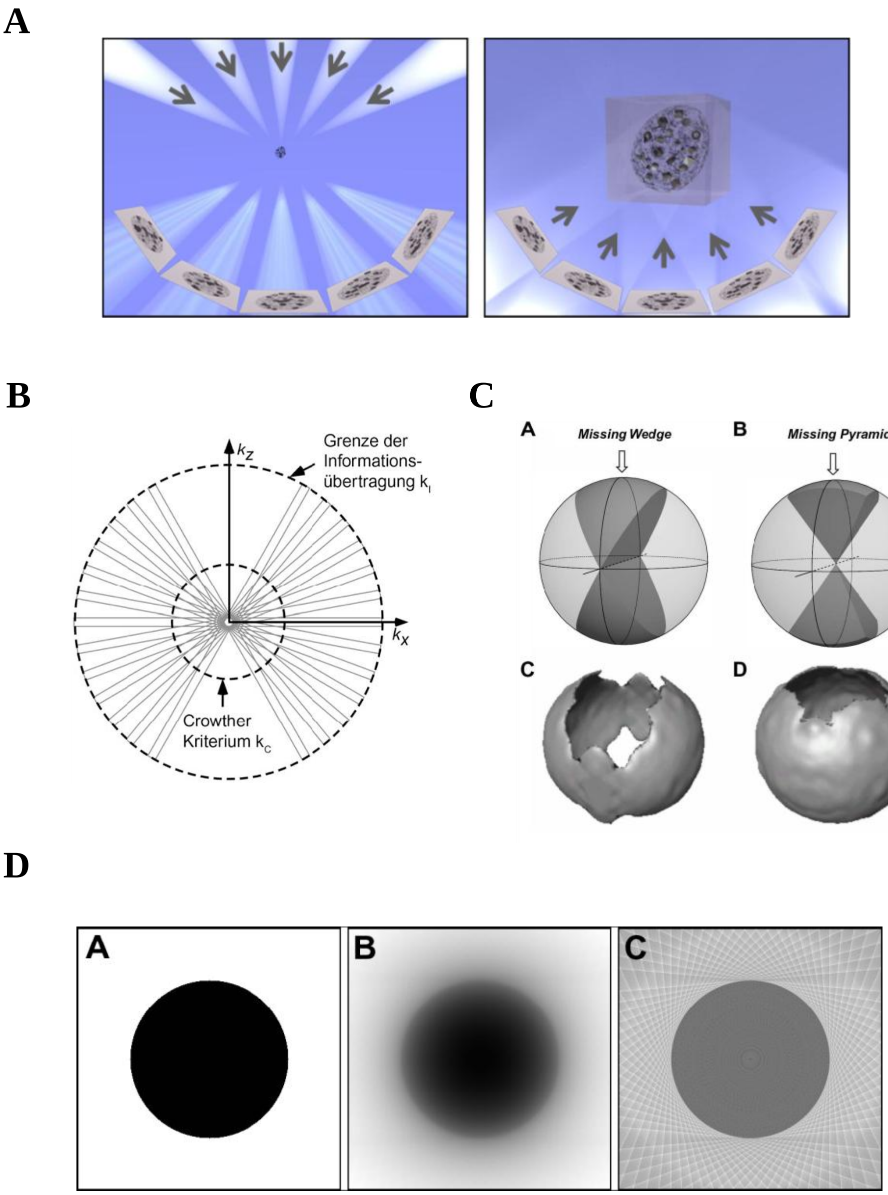

Figure 7: A. Principle of electron tomography. Left: A series of projections is recorded at different tilt angles of the specimen. Right: Computational reconstruction of the 3D object in Fourier space by backprojection (Nickell et al., 2005). **B. Sampling of the object information in Fourier space.** Single projections of an object of thickness D correspond to central sections of thickness 1/D in Fourier space. The central sections are perpendicular to their projection direction. Along k_z the structural information remains inaccessible due to the limited tilt range. Abandoned from this area, the structural information of the object is recorded homogenously up to the frequency k_c, the exceeding information is incomplete. However, it is possible to record object information up to a frequency k_I, which exceeds the Crowther-frequency k_C and, e.g. is limited by the imaging properties of the microscope (Lucic et al., 2005). **C. Influence of the tilting geometry on the 3D reconstruction.** *A. Missing wedge* due to the limited tilting geometry. *B.* Decrease to a *missing pyramid* when tilting around two axes. *C.* and *D.* Representation of the missing information in real space (Lucic et al., 2005). **D. Effect of weighting on the backprojection.** *A.* Section of the volume of a sphere. *B.* Section of a reconstruction of a sphere from 72 projections of a tiltseries from -90° to +90° without weighting. *C.* Section of a weighted backprojection of the same projections (Kofler, 2007).

2.1 Contrast formation in cryo-electron microscopy

In modern cryo-electron microscopes usually a field emission gun (FEG) is the source for a coherent electron beam which is accelerated by a potential of 120 - 300 kV, depending on the application and the sample. In a classic setup, focusing is done by two condenser lenses (C1 and C2) and a condenser aperture, before the sample is penetrated by a preferably parallel beam. Electrons scattered beyond an angle θ_{max} are removed by the objective aperture and the diffracted beam is refocused in the first image plane by the objective lens.

'Non-biological' (or 'no longer biological') samples, e.g. heavy-metal stains, predominantly produce amplitude contrast. However, for biological samples embedded in an amorphous ice layer of 50 - 200 nm thickness, more than 90% phase contrast formation is assumed in the relevant resolution range, caused by singular, elastic scattering with C, N, O and P-atoms with low atomic number (Toyoshima and Unwin, 1988). Phosphate groups, e.g. in lipid head groups, as more electron dense parts, give raise to a comparatively higher contrast than the surrounding water. Due to the high depth of focus of the electron microscope, it is assumed that the contrast resembles the 2D projection of the vitrified sample in the image plane (Lucic et al., 2005).

The phase contrast originates from the interference of the scattered wave with the unscattered primary beam. The resulting diffraction pattern is equivalent to a 2D section through the Fourier transform of the image in frequency space. The diffraction pattern is produced by the objective lens in the back focal plane and becomes visible in diffraction mode. In the normal TEM mode the real intermediate image is magnified and projected on a CCD (*charge coupled device*) camera or film.

Important for cryo-electron microscopy is the adequate quotient of electron dose and gain of information (Henderson, 1995). By unavoidable inelastic scattering mainly valence electrons get excited and thus lead to formation of diffusible radicals in the sample. This process happens also under cryogenic conditions. Cooling of the sample limits the secondary diffusion of highly reactive radicals, however, with increasing electron dose the radiation damage becomes unavoidably larger. For biological molecules this leads to breaking of covalent bonds and later on to a visible evaporation in the amorphous ice. Consequently, the higher the resolution aimed for, the lower has to be the total dose. For high resolution electron crystallography or single particle analysis, a value of 10 - 20 $e^-/Å^2$ is recommended (Henderson, 1995). In the comparable low resolution range of cryo-electron tomography (> 30 Å), doses of 50 - 100 $e^-/Å^2$ are tolerable (McEwen et al., 1995).

2.2 Phase contrast transfer function

Mathematically, the signal transduction in the electron microscope can be described by a convolution of the scattered wave $\Psi_{scatt}(\mathbf{r})$ with a function c which describes the imaging characteristics of the optical system (*point spread function*; PSF):

$$\psi(\mathbf{r}) = \Psi_{scatt}(\mathbf{r}) \otimes c(\mathbf{r})$$

In turn, the PSF equates the Fourier transform of the (phase) *contrast transfer function* (CTF), with which the object information is convolved in frequency space **q**:

$$\psi(\mathbf{r}) = \mathcal{F}^{-1}\{\mathcal{F}\{\Psi_{scatt}\}(\mathbf{q}) \cdot CTF(\mathbf{q})\}$$

The phase of the elastically scattered wave is shifted by 90° (π/2) relative to the unscattered one (Reimer and Rossmessemer, 1989). Thus, a pure phase object imaged with an ideal lens would be invisible. But electromagnetic lenses are not ideal; they elongate the optical path of the traversing scattered wave what causes a phase shift. The reason for the additional phase shift is the spherical aberration and defocusing of the objective lens. Parameters of a simplified CTF are the defocus Δz, the spherical aberration coefficient C_s and the wavelength of the electrons λ:

$$CTF(\mathbf{q}) = sin\,[\tfrac{\pi}{2} C_s \lambda^3 \mathbf{q}^4 - 2\Delta z \lambda \mathbf{q}^2]$$

The CTF describes the imaging characteristics of the objective lens in Fourier space and is independent of the sample structure. It causes oscillation of the contrast between -1 and 1 in frequency space, with the first zero of the CTF moving to lower frequencies while Δz is increased. No contrast is transmitted at the zeros of the CTF and the information is lost in

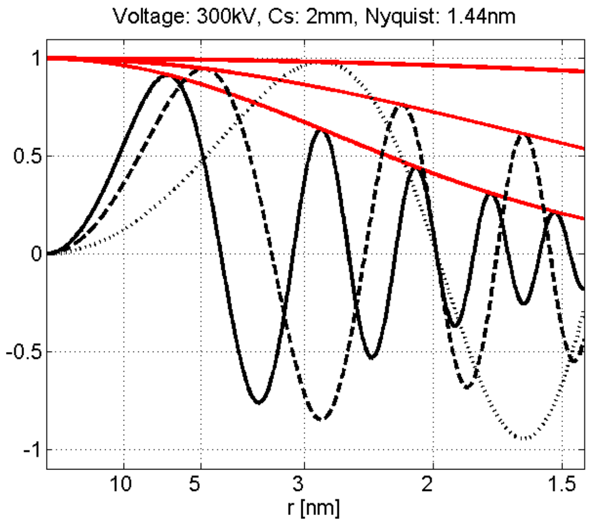

Figure 8: Contrast transfer functions in dependence of the defocus *Δz*. Models of the CTF for an acceleration voltage of 300 kV, a spherical aberration C_S of 2 mm, and an object pixelsize of 7.2 Å at different defoci *Δz* = - 2 µm (···), - 6 µm (▪▪▪) and - 10 µm (▬) with Δz-dependent damping functions (depicted in *red*).

these frequency ranges. Beyond the first zero the contrast flips into the negative and then oscillates in higher frequency ranges. Figure 8 shows models of the CTF for different defocus values *Δz* at an acceleration voltage of 300 kV with the respective damping functions. Several effects lead to damping of contrast transfer of higher frequencies. The finite coherence of the electron source (*partial coherence*) and a chromatic aberration of the electron beam (*energy spread*) damp the amplitude in the higher frequency range, as described by *the envelope function* (Zhu et al., 1997). Furthermore, there is a considerable damping by the *modulation transfer function* (MTF), which describes the transfer of high frequency information by the recording device (a CCD-camera in this work).

2.3 CTF correction in cryo-electron tomography

In the previous chapter it was shown that the contrast transfer function of the microscope limits the resolution of CET, namely below the first zero of the function. Aiming for higher resolution, especially when CET is combined with averaging of sub-tomograms containing identical particles, it is necessary to correct the signal by phase flipping or Wiener filtering (Frank, 1996). To perform CTF correction appropriately it is necessary to determine the shape of the CTF for each image contributing to the reconstruction. Typically, a CTF-model is adjusted to the power spectrum of the image signal, to find suitable parameters with which the phases and amplitudes of the object can be recovered as good as possible from the distorted signal. Up to high frequency ranges this only works for a high signal-to-noise ratio (SNR). This is a standard procedure for single particle analysis, whereas the restoration of the object information by CTF-correction in tomographic, i.e., tilted and noisy projections still is not possible.

Substantial difficulties are encountered in the process of CTF-correcting cryo-tomographic data: (i) Instrumental inaccuracies do not guarantee that the defocus of each image in a tilt series is maintained. (ii) The low SNR hinders detection of the CTF signal on individual images. (iii) Images of tilted specimens present a defocus gradient, and CTF correction cannot be applied uniformly to the whole image.

Several methods for detecting the CTF in tilted specimens have been proposed in the past. Mindell and Grigorieff (2003) calculate the power spectrum of sub-regions extracted from the image to give an estimate of local defocus. This approach is based on data collected with the dose used for single particle studies, which generates images with sufficient SNR to detect CTF oscillations. Winkler and Taylor (2003) rotate the images such that the tilt axis is horizontal, and subareas from image strips with almost invariant defocus can be extracted. These are used to compute rotationally averaged power spectra and to determine the CTF. The method was developed for plastic embedded samples, yielding a higher SNR than cryo-samples. Fernandez and Crowther (2006) determine the CTF of tilted cryo-images by strip based periodogram averaging. The defocus at the tilt axis is assumed to be the same for all images in a tilt series. Areas of similar defocus values are extracted from all images and their mean power spectrum is calculated, thus enabling determination of the defocus gradient. The defocus values used in the latter study ranged between 6 and 26 μm, which are particularly high, even for CET. Recently, Zanetti and coworkers (2009) measured the defocus on individual images using their relative magnification. In a system with non-parallel illumination, defocus and magnification are linearly related for unvarying Condenser 2 lens settings (van Duinen et al., 2005). The gradient depends mainly on the convergence of the beam on the specimen, i.e. the strength of the Condenser 2 lens. For an overfocused condenser lens, specimens at higher defocus have lower magnification. Applied on data of carbon film, this approach yields reliable estimates of defocus, but becomes imprecise for cryo-images.

As well as for the CTF determination, several studies have proposed methods to correct the CTF of images of tilted specimens. For crystalline specimens, Henderson et al. (1990) expressed the

CTF at each spatial frequency as a function of the defocus (the tilt transfer function), and used it to correct areas of the Fourier transform of the crystal images. This approach is not well suited for non-crystalline specimens where the information is distributed continuously over all spatial frequencies. Fernandez et al. (2006) and Winkler et al. (2003) both proposed a strip-based correction, in which the image is rotated such that the tilt axis is horizontal, and correction of strips is performed after interpolation. Zanetti et al. (2009) divide the tilted image into tiles and perform CTF correction prior to rotation.

In the course of an inner-departmental collaboration with Mathias Eibauer, a new method for CTF determination and correction was developed in the context of this thesis. The method was applied to the tomography of porin MspA reconstituted into lipid vesicles. The major difference of our approach is an expanded acquisition scheme to overcome the described limitations by the low SNR (Fig. 9). The defocus values at the exposure area are calculated by means of the average defocii of two high dose images at both sides of the specimen along the tilt axis. The exact procedure is described in chapters 4.11.3 and 4.12 and the results of CTF correction in chapter 5.3.

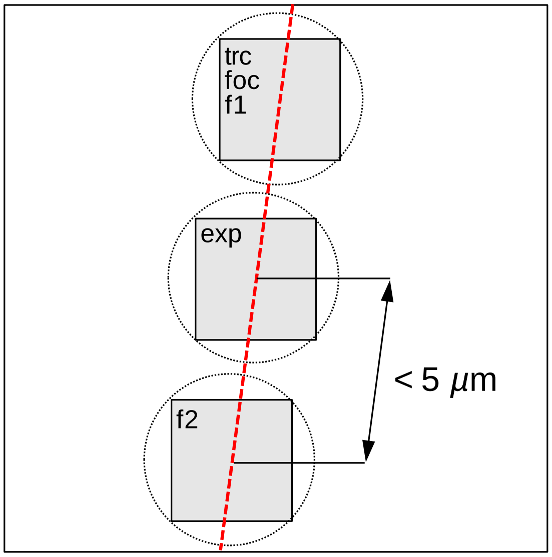

Figure 9: Expanded exposure scheme for CTF-determination and correction of tilted images. In addition to the normal 'low-dose'-routine (*trc*: tracking; *foc*: autofocus; *exp*: exposure) two high-dose images (*f1* and *f2*) are recorded of regions in close proximity (< 5 μm) to both sides of the exposure area along the tilt-axis (*red* dotted line). The high SNR of these images allows the determination of the defocii over the whole tilt-range. From these values the geometry of the exposure area can be calculated and CTF correction is possible.

3 Cryopreparation of biological samples

Cryofixation is a fundamental preparative technique for the structural investigation of biological samples in the presence of water, which is free from structural alterations caused by dehydration, fixation or staining. The native structure and dynamic states within the sample are ‘shock-frozen’. Slow freezing and concomitant conversion of water to hexagonal ice would destroy biological structures otherwise. Besides volume increase during crystallization of water, small solutes, but also macromolecules may be dislocated and lead to disruption of the natural interaction network of biological molecules. By ‘shock-freezing’, i.e. by direct transition of liquid water to vitrified (glass like) ice, crystallization effects are avoided. For a sufficiently thin probe ($D < 1\ \mu$m), this can be achieved at normal pressure by high cooling rates of 10^6 K/s.

For cryopreparation, several microliter of a cell suspension is applied on a specimen grid that is covered by a holey carbon film. Excess liquid is blotted to thin the aqueous film to 50 – 600 nm. The grid is rapidly immersed into a cryogen (Dubochet et al., 1988), usually ethane (boiling temperature 87 K) which is cooled by liquid nitrogen (boiling temperature 77 K). Nitrogen itself is not suitable as a cryogen because the formation of a gaseous cushion around the grid (Leidenfrost phenomenon) would reduce the cooling rate.

Larger cells or volumes of samples must be vitrified by high pressure freezing. The sample is mixed with cryoprotectants (e.g. dextran) to suppress crystal formation upon freezing. The mixture is filled into special containers, for cell suspensions typically copper capillaries (Ø 0.3 mm), and these are mounted in a high pressure freezing apparatus. While a very high pressure (> 2000 bar) is applied on the sample, the capillary is cooled by a jet of liquid nitrogen at the same time. Despite the relatively slow cooling rate of 10^4 °K/s crystal free ice can be obtained to a depth of approx 300 μm.

3.1 Cryosectioning of vitrified biological material

Cryosectioning is currently the only established method to extend tomography to larger cells and tissues in their native state (Bouchet-Marquis et al., 2006; Dubochet and Sartori Blanc, 2001; Hsieh et al., 2006; Masich et al., 2006; Zuber et al., 2005). The suitable thickness of sections ranges from approximately 50 to 300 nm. Thus, the size of organelles or cells is no longer the determining factor for the thickness of specimens. The achievable resolution in 3D is a function of the number of projections, limited by the total dose, and the thickness of the sample. A thinner specimen thus facilitates a higher resolution, but at the expense of 3D-depth.

Sections are usually prepared with diamond knifes from high-pressure frozen material and mounted “dry” on a TEM grid. Like plunge frozen samples, the sections have to be kept below the devitrification temperature of -133 to -138 °C (Dubochet et al., 1988) to prevent the formation of ice crystals. An overview of the development of cryo-ultramicrotomy is given by Sitte (1996).

Unfortunately, cryo-ultramicrotomy is not free of artifacts. The most serious impacts are compression of the material in the cutting direction and knife marks, chatter and crevasses, which affect superficial regions of the sections and may degrade the quality of projection images. The artificial effects were described in detail (Al-Amoudi et al., 2005; Hsieh et al., 2006; Hsieh et al., 2002). Since compression proved to be the most severe difficulty for this work, it is specified here. Compression is indicated by a ‘shortening’ of the ribbon in the cutting direction, accompanied by an increase in section thickness. To what extent a ribbon is compressed varies with the sample and the nominal thickness of the sections, and typically ranges from 30 to 60 % (McDowall et al., 1983; Shi et al., 1996). The effect of compression is illustrated in Figure 10, where the distance between the cytoplasmic and the outer membrane of the bacterial cell is considerably reduced in the cutting direction. An integral part of this work was to determine the dimensions of the constituents of the mycobacterial cell wall. It is obvious that cryosectioning is only of limited use for this task. Meaningful measurements could only be done in restricted areas perpendicular to the cutting direction (indicated by the arrowheads) since these are disturbed least by compression (Matias et al., 2003).

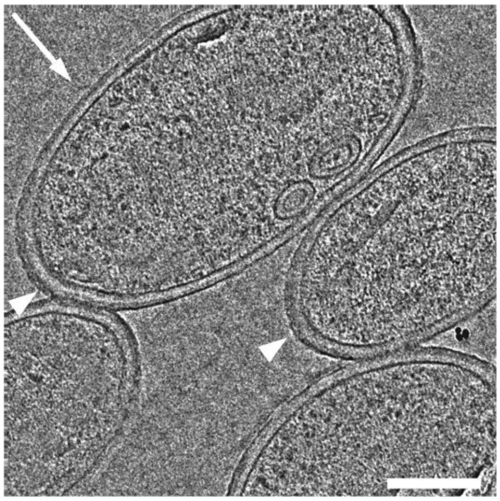

Figure 10: Cross-section of frozen hydrated *M. smegmatis* cells deformed by the cutting process. Regions perpendicular to the cutting direction (arrow) are disturbed least by the sectioning (arrowheads; and can be used for further analysis (arrowheads). (Scale bar: 200 nm.)

Moreover, sectioned ribbons are not perfectly flat and only poorly attached to the support film on the grid, resulting in a ‘buckled’ morphology, which in turn hampers the imaging process during specimen tilting in tomography. Ultrathin cryosections (< 100 nm) are currently superior in quality to thicker ones and offer the best possible resolution. However, larger cellular structures cannot be captured within such restricted volumes unless serial sectioning is used, which poses an additional technical challenge (Leis et al., 2009). In addition, while many sections cut with the ultramicrotome will be suitable for 2D imaging, only a small fraction will be usable for tomography. Despite its potential for 3D imaging of large cells and tissue, cryo-sectioning is still a demanding craftsmanship and far from ideal for potential automation and/or high-throughput applications.

3.2 Cryopreparation by focused ion beam (FIB) micromachining

An alternative method for thinning of vitreous biological material is the use of a focused ion beam (FIB). Instrumental setups where originally developed for applications in material sciences and are commonly used to directly modify semiconductor devices, for fabrication of opto-electronic parts and for failure analysis (Volkert and Minor, 2007). The FIB technique for the preparation of inorganic TEM specimens was introduced more than 20 years ago and has since then become one of the major preparation methods due to its unsurpassed site-specific preparation possibilities (Kirk et al., 1989). For micromachining and imaging, a primary ion beam, typically Gallium, is used to ablate the surface of a specimen via sputtering of substrate atoms (Giannuzzi and Stevie, 2005). In dual beam microscopes, the FIB is combined with a scanning electron microscope (SEM; Fig. 11) which allows simultaneous monitoring of the milling process, as used in ‘slice-and-view’ applications (Knott et al., 2008), and thus avoids continual erosion of the scanned area during imaging with ions. The development of sample stages and transfer systems suitable for cryogenic temperatures dual beam systems (SEM/FIB) in the meantime allows to thin frozen-hydrated specimens site-specifically while the process and the resulting sample surfaces can be monitored in a non-destructive way using the SEM (Heymann et al., 2006; Marko et al., 2006; Mulders, 2003). The application of an oblique or ‘grazing’ angle of the incident ion beam ensures that implantation of Gallium is minimized; compression or other artifacts known from mechanical sectioning are completely missing. Furthermore, there is evidence that heat transfer to the sample during milling does not cause devitrification (Marko et al., 2006). However, only one study with *E. coli* cells has successfully demonstrated the potential of cryo-FIB thinning in combination with cryo-electron tomography (Marko et al., 2007). A cryo-transfer system and a cryo-sample stage were designed and developed (Rigort et al., 2010). In the course of this thesis, the previous results of Marko and coworkers could be confirmed with *M. smegmatis*, and the results were compared with the data obtained from cryosections and tomography of intact cells.

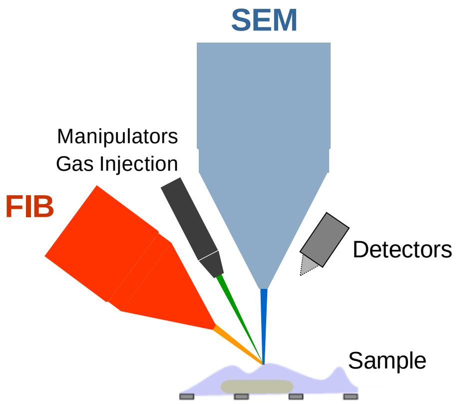

Figure 11: Operating principle of a SEM/FIB dual beam system. The combination of a focused ion beam with a scanning electron microscope allows parallel monitoring of the ablating process without continuous erosion of the scanned area during imaging with ions. The sample (cell on an EM grid, embedded in vitreous ice) is kept below -160° C during the whole process of micromachining by means of a specially designed cryo-stage (Rigort et al., 2010). Several manipulators, injectors and detectors can be used for special applications.

4 Materials and Methods

Chemicals and media were purchased from Roth (Karlsruhe, Germany), Merck (Darmstadt, Germany), Sigma-Aldrich (St. Louis, USA), Fluka (Buchs, Switzerland), Difco (BD Biosciences, Franklin Drive, USA), Serva (Heidelberg, Germany), Avanti Polar Lipids (Tuscaloosa, USA), Boehringer (Mannheim, Germany) or Bachem (Heidelberg, Germany) unless statet otherwise.

4.1 Materials and Instruments

Table 1: Auxiliary Materials

Material	Source
Anion exchange column POROS 20HQ (20,1 ml)	PerSeptive Biosystems, USA
BioBeads	BioRad, München
C-Flat R2/1 copper grids	EMS, USA
Electroporation cuvettes (2 mm)	BioRad, München
Blotting paper S&S 595	Schleicher & Schuell, Dassel
Filter Minisart (0.22 and 5.0 µm poresize)	Schleicher & Schuell, Dassel
Gelfiltration column G3000SW$_{XL}$ (14.3 ml)	TosoHaas, Stuttgart
Polycarbonate membranes (50, 100 and 200 µm)	Schleicher & Schuell, Dassel
Quantifoil R2/1 copper- and molybdenum grids	Qantifoil Micro Tools, USA
Slide-A-Lyzer dialysis tubes (20.000 MWCO)	Thermo Scientific, USA
Sterile filter (0.22 µm)	Eppendorf, Hamburg

Table 2: Instruments

Instrument	Source
Äkta Purifier 10/100	Pharmacia, USA
Cryo plunger	custom made, R. Gatz
CM120 EM	Philips, Hamburg
Diamond knife (25° and 35°)	Diatome, Switzerland
EMPACT2 high pressure freezing system	Leica, Austria
GenePulser XCell	BioRad, München
Cryo sample holder	Gatan, USA
MilliQ PLUS Ultra Pure Water System	Millipore, Schwalbach
Mini extruder	Avanti-Polar Lipids, USA
Plasma cleaner	Harrick, USA
Quanta 3D FEG FIB	FEI, USA
RC5B ultra centrifuge	Sorvall, USA
Rotanta 46 RS centrifuge	Hettich, Tuttlingen
Tecnai F20 EM	FEI, The Netherlands
Tecnai G2 Polara EM	FEI, The Netherlands
Ultracut FC6 cryo ultramicrotome	Leica, Austria
UV/VIS Lambda 40 photospectrometer	Perkin Elmer, USA
VitroBot	FEI, USA

4.2 Bacterial strains, plasmids, oligonucleotides and enzymes

Table 3: Bacterial strains

Strain	**Genotype**	**Reference**
E. coli DH5α	*rec*A1; *end*A1; *gyr*A96; *thi*; *rel*A1; *hsd*R17(r$_K^-$,m$_K^+$); *sup*E44; ϕ80Δ*lac*ZΔM15; Δ*lacZ*YA-argF)UE169	(Sambrook et al., 1989)
M. smegmatis mc^{2}155	not characterized, high transformation efficiency	(Snapper et al., 1990)
M. smegmatis ML10	SMR5 derivative, Δ*mspA* / Δ*mspC*	(Stephan et al., 2004b)
M. bovis BCG	strain Institute Pasteur	ATCC 27291
C. glutamicum 13032	type strain	(Dusch et al., 1999)
C. glutamicum Δ*pks13*	13032 derivative, Δ*pks13*	(Portevin et al., 2004)

Table 4: Plasmids

Plasmid	**Description**	**Source**
pMS2	Hyg^R; shuttle plasmid for *E. coli* and Mycobacteria	(Kaps et al., 2001)
pMN016	Hyg^R; pMS2 derivative; p$_{smyc}$-*mspA*; *Swa*I	Xiuan Bai, unpublished
pMN035	Hyg^R; pMN016 derivative; p$_{smyc}$-rv1698	(Hillmann et al., 2007)
pCH003	Hyg^R; pMN016 derivative; *mspA*-D56N/E57N/D90N/D91N/D93N/D118N/E127N/D134N/D139N	this study
pCH004	Hyg^R; pMN016 derivative; *mspA*-D56N/E57N/D90N/D91N/D93N/D118N/E127N/D134N/D139N ΔL6	this study

Table 5: Oligonucleotides

Oligonucleotide	**Sequence (5‘ → 3‘)**	**Application**
pMS-Seq1	CGTTCTCGGCTCGATGATCC	amplification of *mspA*
psmyc1	CGACCAGCACGGCATACATC	amplification of *mspA*
mspA-FP	TGGGACACCTTCCTCAATGG	sequencing of *mspA*
mspA D56N/E57N	CCGGCCCCGGTGCC$\underline{\text{AACAAC}}$TTCGAGGGCACGCTG	cloning of *mspA* D56N/E57N
mspA D90N/D91N	CCCCGAACATCCTGATC$\underline{\text{AACAAC}}$GGTGACATCACCGCTCC	cloning of *mspA* D90N/D91N
mspA D93N	CAACAACGGT$\underline{\text{AAC}}$ATCACCGCTCC	cloning of *mspA* D93N
mspA D118N	CGATCTCGGCA$\underline{\text{AAC}}$CTGGGCAACG	cloning of *mspA* D118N
mspA E127N	CGGCATCCAG$\underline{\text{AAC}}$GTCGCAACG	cloning of *mspA* E127N
mspA D134N	CGTTCTCGGTC$\underline{\text{AAC}}$GTCTCCGGC	cloning of *mspA* D134N
mspA D139N	CCGGCGCC$\underline{\text{AAC}}$GGTGGCG	cloning of *mspA* D139N
ΔA	TCGGTCATCACCCCGAACCTGTTC	deletion of L6 (upstream)
ΔB	GTCGTCGATCAGGATGTTCGG	deletion of L6 (downstream)

Introduced mutations are underlined. The mutagenesis oligonucleotides were phosphorylated at the 5‘-end.

Table 6: Enzymes

Enzyme	**Source**
Pfu-Polymerase	Fermentas, St. Leon-Rot
Ampligase, thermostable ligase	Epicentre, USA
Restriction endonucleases SphI and HindIII	NEB, USA
T4 DNA ligase	NEB, USA
T4 Polynucleotide kinase	NEB, USA

4.3 Media, buffers and solutions

If not stated otherwise, media, buffers and solutions were prepared with deionized or Millipore® water and autoclaved for 20 min at 121°C and 2 bar. Heat-labile substances were dissolved and filtered through a sterile filter (pore size 0.22 μm). A pH-meter was used to adjust the pH-values.

4.3.1 Media

LB-Broth:	10 g/L	Tryptone
	5 g/L	Yeast extract
	10 g/L	NaCl
MAN-Broth:	10 g/L	Tryptone
	5 g/L	Yeast extract
	10 g/L	NaCl
	5 mM	Mannose
	0.5 mL/L	100% Tween 80
BHI-Broth:	37 g/L	BHI Broth
	1 g/L	bacto agar
7H9-Broth:	4.7 g/L	7H9 Broth
	0.5 mL/L	100% Tween 80
	3.3 mL/L	60% Glycerol
7H10-Agar:	19 g/L	7H10 Agar
	5 mL/L	100% Glycerol
SOC-Broth:	20 g/L	Trypton
	5 g/L	Yeast extract
	10 mM	NaCl
	2.5 mM	KCl
	10 mM	$MgCl_2$
	10 mM	$MgSO_4$
	20 mM	Glucose

For the preparation of solid media, LB and BHI were supplemented with 12 g/L agar and autoclaved together with all other components.

Antibiotics were prepared as a 1000-fold stock solution and added to autoclaved media after cooling down to approximately 50°C in the following concentrations:

Table 7: Antibiotics

Antibiotic	**final concentration *E. coli***	**final concentration *Mycobacterium sp.***	**final concentration *Corynebacterium sp.***
Ampicillin	-	100 μg/mL	-
Hygromycin B	200 μg/mL	50 μg/mL	-
Kanamycin	-	20 μg/mL	25 μg/mL
Streptomycin	-	100 μg/mL	-

4.3.2 Buffers and solutions

General buffers and solutions

TE:	10 mM Tris/HCl pH 7.5 0.1 mM EDTA	PBS:	0.14 M NaCl 0.01 M KH_2PO_4/K_2HPO_4 pH 7.4 0.002 M KCl
10x CCR-buffer:	200 mM Tris/HCl pH 8.4 30 mM $MgCl_2$ 500 mM KCl 5 mM NAD		

Buffers and solutions for DNA gel electrophoresis

Agarose gel: (0.8-2%)	0.8-2% (w/v) Agarose in 1x TAE	20x TAE:	0.8 M Tris 0.4 M Acetic acid 0.025 M EDTA pH 8.3 (acetic acid)
DNA loading buffer:	0.1 % (w/v) Bromphenol blue 0.1 % (w/v) Xylencyanol 50 % (w/v) Glycerol in 1x TAE		

Buffers and solutions for polyacrylamide gel electrophoresis

Collection gel: (4%)	1 mL Acrylamide (37.5:1) 2.6 mL 3x gel buffer 4 mL H_2O Millipore 0.16 mL 10% APS 0.01 mL TEMED	Separation gel: (10%)	4.5 mL Acrylamide (37.5:1) 4.5 mL 3x gel buffer 3 mL H_2O Millipore 1.35 g Glycerol 0.135 mL 10% APS 0.015 mL TEMED
4x protein loading buffer:	0.14 M Tris/HCl pH 7.0 30 % (w/v) Glycerol 4 % (w/v) SDS 0.1 % (w/v) Bromphenol blue	3x gel buffer:	3 M Tris/HCl pH 8.5 0.3 % (w/v) SDS
10x anode buffer:	1 M Tris/HCl pH 8.5	10x cathode buffer:	1 M Tris/HCl pH 8.25 1 M Tricin 1% (w/v) SDS

Buffers for the selective purification of MspA

3x PEN:	300 mM NaH_2PO_4/Na_2HPO_4 pH 6.5 0.3 mM EDTA 450 mM NaCl	POP05:	1x PEN 0.5 % (w/v) OPOE
AOP05:	25 mM HEPES/NaOH pH 7.5 10 mM NaCl 0.5 % (w/v) OPOE	BOP05:	25 mM HEPES/NaOH pH 7.5 2 M NaCl 0.5 % (w/v) OPOE

NaPOP05: $25\ mM\ NaH_2PO_4/Na_2HPO_4$ pH 7.5
0.5 % (w/v) OPOE

Liposome Buffer

NaPNOP: $25\ mM\ NaH_2PO_4/Na_2HPO_4$ pH 7.5

4.4 General Methods

Table 8: General methods

Method	Reference
Gel electrophoresis of DNA	(Ausubel et al., 1987)
Ethidium bromide staining of DNA	(Ausubel et al., 1987)
Ligation of DNA fragments	(Ausubel et al., 1987)
Polymerase chain reaction	(Mullis et al., 1986)
DNA sequencing	(Sanger et al., 1977)
Preparation of competent *E.coli* cells	(Hanahan et al., 1991)
Transformation of *E.coli* cells	(Hanahan et al., 1991)

Table 9: Commercially available systems („kits”)

System	Application	Source
QIASpin Miniprep Kit	plasmid preparation	Qiagen, Hamburg
QIAquick Gelextraction Kit	DNA gel extraction	Qiagen, Hamburg
BCA Protein Assay Kit	determination of protein concentration	Pierce, USA

4.5 Bacterial growth conditions

Unless mentioned otherwise *M. bovis* BCG and *M. smegmatis* were grown at 37° C in Middlebrook 7H9 liquid medium supplemented with 0.2% glycerol, 0.05% Tween 80, or on Middlebrook 7H10 agar supplemented with 0.2% glycerol. The media for the bacillus Calmette-Guérin strain were additionally supplemented with ADS (0.5% BSA fraction V, 0.2% dextrose, and 14 mM NaCl). *E. coli* DH5α was routinely grown in LB medium at 37°C. The S-layer-less *C. glutamicum* ATCC 13032 RES167 (Dusch et al., 1999) and *C. glutamicum* Δpks13::km were cultured at 30°C in BHI medium. Antibiotics were added to the media according to Table 7. Inoculation was done by supplying cells from a preculture from freshly spread colonies. Growth was monitored by measuring the optical density at $\lambda = 600$ nm.

4.6 Detachment of the outer membrane

M. smegmatis mc^{2}155 was routinely grown overnight in Middlebrook 7H9 medium. After extensive washing with 25 mM Tris/HCl buffer solution (pH 7.0), cells were incubated for 1 h at 37°C in the same buffer containing 1.0% octyl β-glucoside. The cells were harvested and prepared for cryo-electron microscopy as described below.

4.7 Extraction and purification of MspA

4.7.1 Growing and harvesting of the cells

1L 7H9 broth with 50 mg/mL hygromycin in a 2L beveled flask was inoculated with 1 mL of a *M. smegmatis* ML10 preculture harboring either the plasmid pMN016 for expression of wild-type MspA or a plasmid encoding mutated MspA. After incubation under agitation at 37°C for 48 h the cells were harvested (4500 rpm, 30 min, 4°C), resuspended in 1x PBS and centrifuged again. The cells were processed immediately or stored at -20°C.

4.7.2 Extraction of MspA

10 g cells (wet weight) were resuspended in 35 mL extraction buffer POP05 containing detergent and the suspension was heated in a boiling water bath for 30 min. Afterwards, the suspension was immediately cooled on ice for 10 min. The extract was centrifuged at 4,000 ×*g* for 30 min at 4°C. The protein containing supernatant was stored at -20°C until being processed further.

4.7.3 Acetone precipitation

The raw extract was carefully mixed with the same volume of ice cold acetone and incubated for 1 h at -20°C. It was then centrifuged at 8,000 ×*g* for 30 min at 4°C. The protein containing pellet was dissolved in 25 mL AOP05 buffer per gram wet weight and filtered (Sartorius, 5μm pore size) to remove insoluble particles.

4.7.4 Chromatographic purification

The chromatographic purification was done following the protocol from Heinz (Heinz et al., 2003b) with minor adjustments. Briefly, the filtered solution was loaded on an anion-exchange column (POROS 20HQ) and bound protein was eluted with a gradient from 10 mM NaCl to 2 M NaCl over five column volumes. The collected fractions were analyzed using SDS-PAGE. Fractions containing pure MspA were combined and the protein concentration was determined using the BCA test. After a second acetone precipitation the pellet was dissolved in 1-2 mL NaPOP05 buffer, filtered and loaded on a gel filtration column (G3000SW$_{XL}$). Protein was eluted at a flow rate of 0.5 mL/min. The fractions were analyzed by SDS-PAGE, and the protein concentration was determined with the BCA test. The MspA preparation was stored at 4°C.

4.8 Preparation of proteovesicles for CET

4.8.1 Preparation of lipid vesicles by extrusion

Lipid vesicles were prepared by dissolving 1,2-Diphytanoyl-sn-Glycero-Phosphocholine (DiphPC) in chloroform. The mixture was dried to a thin film by evaporation under a stream of nitrogen for at least 2 h. The lipid film was hydrated in liposome buffer (NaPNOP) and subjected to 3 - 5 cycles of freeze thawing (dry-ice in ethanol), followed by 11 - 15 cycles of extrusion through a Nuclepore® Track-Etched Membrane (pore size 50 or 100 nm) using a mini-extruder (Avanti Polar Lipids, Alabaster, USA). During vesicle formation the temperature of the lipid preparation was kept at 45°C to ensure the lipid being in the ‘liquid’ phase. The vesicle suspension had a lipid concentration of 2 - 5 mg/mL.

4.8.2 Reconstitution of MspA into lipid vesicles

500 to 750 μL vesicle preparation was mixed with 10 to 25 μg MspA in solution containing 0.5 % octyl-POE. To remove the detergent from the proteins and thus ensure reconstitution, 50 mg BioBeads® SM-2 (Bio-Rad) were added, and the mixture was incubated for at least 12 h at 37°C and slow rotation. BioBeads® SM-2 were spun down (1000 ×*g* for 1 min) and the proteovesicles in the supernatant were ready for cryo-preparation.

4.9 Constructing mutants of MspA

4.9.1 Site-directed mutagenesis by combined polymerase chain reaction (*CCR*)

The advantage of the combined polymerase chain reaction is that the insertion of the mutation and the amplification of the mutated fragment happen in only one step. In-between purification steps are unnecessary, no product is lost, and less undesired mutations occur compared to the two-step PCR mutagenesis (Landt et al., 1990). Furthermore, the method is quite fast since several mutations can be introduced in the gene in one run.

The CCR combines the polymerase chain reaction with the ligation step. In contrast to the normal PCR, three or more oligonucleotides are needed. Every cycle comprises four steps: denaturation of the template DNA, annealing of the oligonucleotides, extension of the oligonucleotides and ligation of the 3’-OH end of the synthesized strand with the 5’-phospate end of the mutagenesis oligonucleotide. The ligation can only occur when the 5‘-end of the mutagenesis oligonucleotide is phosphorylated. Because of the high temperatures during the CCR a thermostable ligase is needed. pMS-Seq1 and psmyc1 (Tab. 5) were used as 3’- and 5’-oligonucleotides, the *mspA*- gene carrying plasmid pMN016 (Tab. 4) was the template. The mutagenesis oligonucleotides are listed in Table 5. The enzyme *Pfu* was used as polymerase. Unless stated otherwise, the samples were treated as follows:

composition:

20 ng	mutagenesis oligo, 5‘-pho
20 ng	3‘- oligo
20 ng	5‘- oligo
20 ng	plasmid DNA
2 μL	10x CCR buffer
2.5 mmol	dNTPs
2.5 U	Pfu-polymerase
3 U	Ampligase
2 μL	BSA, 4 mg/mL
ad 20 μL	H_2O Millipore

CCR reaction profile:

96°C	2 min	1x	(denaturation)
96°C	30 sec	30x	(denaturation)
52-58°C	45 sec	30x	(annealing)
72°C	4 min	30x	(extension)
72°C	7 min	1x	(final extension)
4°C	∞		

4.9.2 Construction of the MspA loop 6 (L6) deletion mutant

The L6 deletion mutants were constructed using the plasmid pCH003 as a template. Psmyc1 and pMS-seq1 were used as end primers along with appropriate mutagenesis primers to perform a twostep PCR. Separate PCR amplifications of the upstream and downstream portions of the gene flanking the deletion were performed. Then the two purified PCR products were amplified and ligated together in the same reaction using Ampligase. Mutated mspA genes were then ligated into SphI and HindIII double digested pMN035 to generate the plasmid pCH004. Primers and resulting plasmids are listed in Tables 4 and 5.

All of the plasmids were verified by sequencing the entire mspA gene before they were transformed into the porin mutant *M. smegmatis* ML10 for protein production.

composition ΔA-upstream:

20 ng	ΔA-oligo, 5‘-pho
20 ng	pMS-Seq1
20 ng	plasmid DNA
2 μL	10x PCR buffer
2.5 mmol	dNTPs
3 U	Pfu-polymerase
2 μL	BSA, 4 mg/mL
ad 20 μL	H_2O Millipore

composition ΔB-downstream:

20 ng	ΔB-oligo
20 ng	psmyc1
20 ng	plasmid DNA
2 μL	10x PCR buffer
2.5 mmol	dNTPs
3 U	Pfu-polymerase
2 μL	BSA, 4 mg/mL
ad 20 μL	H_2O Millipore

PCR reaction profiles:

96°C	2 min	1x	(denaturation)
96°C	30 sec	30x	(denaturation)
55°C	30 sec	30x	(annealing)
72°C	45 sec	30x	(extension)
72°C	7 min	1x	(final extension)
4°C	∞		

4.9.3 Electroporation of *M. smegmatis* ML10 cells

Preparation of the cells: 500 mL 7H9 broth, supplemented with ADS enrichment, was inoculated with 4 mL filtered (pore size 5 μm) preculture of *M. smegmatis* mc^{2}155 and incubated until an OD_{600} of 0.6-0.8 was reached. The culture was harvested (4,000 ×*g*, 15 min, 4°C) and resuspended in 125 mL ice cold 10% glycerol. This step was repeated three times, each time reducing the resuspension volume by half. After the final centrifugation step, the cells were resuspended in 5 mL 10% glycerol, aliquots of 100 µL were snap-frozen in liquid N_2 and stored at -80°C.

Transformation: The cells were thawed on ice, carefully mixed with 0.5 - 1 µg of DNA and transferred into a precooled 2 mm electroporation cuvette. After pulsing (U = 2.5 kV, R = 1,000 Ω, C = 25 μF), the bacteria were resuspended with 1 mL 7H9 broth and recovered at 37°C for 3 h. Afterwards, the cells were plated on selective media and incubated for approx. 3 days.

Mutated MspA was purified according to the wild-type, following the protocol described above.

4.10 Conductivity assays

All conductivity analyses were done in collaboration with the Nanion Technologies GmbH (Munich) using the Port-a-Patch® patch clamp rig (Farre et al., 2009). Solvent-free planar lipid bilayers are formed in an automatic manner by bursting of giant unilamellar vesicles (GUVs) after gentle suction application through micron-sized apertures in a borosilicate glass substrate. Incubation of the GUVs with purified wild-type MspA or the mutants of interest yielded proteoliposomes which allow for immediate recording of channel activity after GUV sealing.

4.10.1 Preparation of liposomes

Planar lipid bilayers were obtained from GUVs prepared by using the electroformation method (Angelova, 2001) in an indium tin oxide (ITO) coated glass chamber connected to the Nanion

Vesicle Prep Pro® setup (Nanion Technologies GmbH, Munich, Germany). The ITO-layers on the two glass slides are electrically conductive, and therefore serve as electrodes. Lipid-containing solution, 5 or 10 mM of 1,2-Diphytanoyl-sn-Glycero-Phosphocholine (DiphPC), dissolved in chloroform, was deposited on the ITO-coated glass surface. After total evaporation of the solvent, the lipids are assembled in a perfectly dehydrated lamellate phase. An O-ring was placed around the dried lipid film and 300 μl of a 1M solution of sorbitol was carefully added to the lipid film. Then, the second ITO-slide was placed on top of the ring, with the ITO-layer facing downwards. The process of electroformation was controlled by the Vesicle Prep Pro® setup and all parameters (amplitude, frequency, duration, *etc*.) were programmed in the *VesicleControl* software. Generally, an alternating voltage of 3 V peak to peak was applied with a progressive increase for the rise time and a decrease for the fall time to avoid abrupt changes, which otherwise might rupture the formed GUVs. The alternating current was applied to the ITO-slides over a period of 2 h at a frequency of 5 Hz at room temperature. After successful swelling, the vesicles were used directly for the reconstitution of the porins.

4.10.2 Reconstitution of wild-type MspA and the mutants in GUVs

In contrast to conventional bilayer recordings, where reconstitution of proteins is achieved by adding the protein after bilayer formation in the presence of detergent, here the porin is inserted into the GUVs directly after the electroformation. Purified wild-type or mutated MspA (ca. 60 μg/mLor ca. 30 μg/mL) in solution containing 0.5 % octyl-POE was reconstituted into GUVs by adding MspA with a final protein concentration between 0.2 – 0.5 μg/mL to 300 µl of the GUV solution. The final concentration of detergent was approximately 0.002%. The mixture was incubated for 1 h at room temperature, followed by the addition of BioBeads® SM-2 at 40 mg/ml and further incubation at room temperature overnight to remove the detergent. BioBeads® were discarded after centrifugation and the protein containing GUVs could be used immediately.

4.10.3 Planar lipid bilayer formation

1 to 3 μl of the proteoliposomes solution was pipetted onto the patch clamp chip to form a lipid bilayer. The GUVs were positioned onto the aperture in the chip by application of a slight negative pressure. When the GUVs touch the glass surface of the chip, they burst and form planar bilayers (Farre et al., 2007) with a seal resistance of tens to hundreds of GΩ.

4.10.4 Data recording and analysis

Based on the aperture diameter of the chip (approximately 1 µm) and a specific conductance of DiphPC of 0.5 μF/cm^2 (Farre et al., 2007; Schuster et al., 1998), the membrane capacitance could be estimated to be in the order of a few fF. Experiments were done in symmetric solutions of 1 M KCl at pH 7.5.

Currents were amplified with an EPC-10 patch clamp amplifier (HEKA Electronics, Germany) connected to Ag/AgCl electrodes in the Port-a-Patch system. The signal was filtered at 10 kHz (Bessel filter, HEKA amplifier), digitized at a sampling rate of 50 kHz and analyzed with the pClamp 10.0 software (Axon Instruments, Foster City, USA).

4.11 Electron microscopy

4.11.1 Sample preparation

4.11.1.1 Fiducial gold markers

BSA was dissolved in Borax buffer (2 mM sodium borate, pH 9.0) to a concentration of 10 % w/v. 10 μL BSA solution was mixed with 10 mL freshly prepared gold suspension (Slot and Geuze, 2007) with has been adjusted to pH 9.0 and vortexed. The BSA-coupled gold was spun down at 20,000 $\times g$ for 5 min at 4°C, resuspended in PBS containing 0.1% BSA and transferred to a new Eppendorf tube. It was stored at 4°C.

4.11.1.2 Negative stain

Carbon coated copper grids that were made hydrophilic by glow discharging for 30 sec were incubated for 1 min on a drop of sample solution sitting on parafilm. They were consecutively transferred to two drops of H_2O for washing. The specimen were negatively stained on a drop of 2% (w/v) uranylacetate for 30 to 60 sec.

4.11.1.3 Plunge freezing

Holey carbon copper grids were glow discharged for 30 sec and 3 to 5 μL of the respective sample was applied. BSA-conjugated gold markers were added (typically 5 μL), excess fluid was blotted using filter paper from the backside of the grid and the samples were vitrified by plunge freezing in liquid ethane. The grids were stored in liquid nitrogen.

4.11.1.4 High-pressure freezing

Samples of 5 mL of a freshly grown cell suspension of Mycobacteria or Corynebacteria were concentrated by low speed centrifugation at 4,000 $\times g$ for 3 min at 4°C and carefully mixed 1:1 with the cryo-protectant dextran (100 – 200 kDa; 40% (w/v)) dissolved in PBS. The solution was drawn into copper capillary tubes. The tubes were rapidly frozen in a high-pressure freezer (EM-Pact2; Leica, Vienna, Austria) and stored in liquid nitrogen.

4.11.1.5 Vitreous sectioning

The copper capillary containing the sample was mounted in the chuck of a Leica Ultracut FC6 cryo-ultramicrotome. The temperatures of the knife, the sample holder, and the chamber atmosphere were held between -150°C and -160°C. The surrounding metal of the capillary and excess sample was trimmed away, thus exposing a blunt pyramid. A diamond knife (Diatome, 25° cutting angle, 6° clearance angle) was used to prepare the sections with nominal thicknesses ranging from 20 - 50 nm and cutting speeds between 1.0 and 20 mm/s. An ionizer helped to improve the gliding of section ribbons along the knife and to transfer the samples onto grids covered with a continuous carbon film. After firmly pressing the section on the grid by means of a stamping tool, the grids were stored in liquid nitrogen. To minimize contamination of the samples with frost, the whole setup was located in a chamber, which is connected to an air-drying system.

4.11.1.6 Focused ion beam (FIB) micromachining

In order to protect the vitrified specimen from ice contamination and to ensure maximal thermal stability, a cryo-FIB loading station with a transfer ‘shuttle’ adapted to the Polarprep 2000T cryo-system (Quorum, East Sussex, UK) was designed and constructed as described in Rigort et al. (Rigort et al., 2010). *M. smegmatis* cells in suspension were plunge-frozen as depicted above (cf. 4.11.3). By utilizing the new loading station and transfer shuttle, the frozen-hydrated EM grids were micromachined with a dual-beam (FIB/SEM) instrument (Quanta FEG 3D, FEI, Hillsboro, USA), equipped with a Quorum cryo-stage maintained at -160° C. The vitrified samples were imaged at 5 keV with the SEM and milled with 30 keV Gallium ions by rapidly scanning the selected regions at various tilt angles using a beam current of 10 – 15 pA.

4.11.2 Data acquisition

Table 10 gives an overview about the characteristics of the microscopes used for this work. Tilt series were collected according the ‘low-dose’-acquisition scheme (Dierksen et al., 1992; Dierksen et al., 1995; Koster et al., 1997; Koster et al., 1989) covering a minimum angular range of 120°, with angular increments of 1.5°, 2° or 3°. Defocus was measured along the tilt axis after each tilt and automatically adjusted to -4 to -12 μm ± 0.5 μm. The total electron dose at the specimen level was kept between 50 - 100 $e^-/Å^2$. To compensate for the increase in sample thickness with higher tilt angles, the exposure time was adjusted by a 1/*cos* scheme.

Table 10: Microscopes, cameras and software used for data acquisition. Several microscopes were equipped with a post-column energy filter (Gatan).

Microscope	**U** (kv)	**Energy filter**	**Multiscan CCD camera**	**Acquisition software**
CM120 Biotwin	120	+	Gatan 1k x 1k	Digital Micrograph (Gatan)
CM300 FEG	300	+	Gatan 2k x 2k	Digital Micrograph (Gatan)
Tecnai F20	200	-	FEI Eagle 4k x 4k	*TOM-toolbox* (Nickell et al., 2005) FEI *User Interface*
Tecnai Polara	300	+	Gatan 2k x 2k	*TOM-toolbox* (Nickell et al., 2005) FEI *User Interface*

Table 11: Projects and the used respective microscopes.

Project	**Microscope**	**Magnification** (Pixelsize [nm])	**Defocus** (µm)
Whole-cell tomography of mycobacteria	Tecnai Polara	18 k to 34 k (0.71 to 0.38)	-12 to -4
Vitreous sections of mycobacteria and corynebacteria	Tecnai Polara	18 k to 36 k (0.71 to 0.38)	-8 to -5
Tomography of mycobacterial cryo-samples prepared with a FIB	Tecnai Polara	27.5 k (0.47)	-6 to -5
MspA reconstituted into lipid vesicles	Tecnai Polara, F20	61 k (0.21) 29 k (0.37)	-8 to -2 -8 to -4

4.11.3 Extended data acquisition scheme for CTF correction of tilt series

Acquisition of two additional high-dose images was done manually with the 'FEI *user interface*'. After every cycle of 'tracking', 'autofocus' and 'exposure', the run was paused and, via a beam shift along the tilt-axis, the imaging position was set to the corresponding areas referred to as *f1* and *f2*. The distances from the exposure area were kept large enough to avoid any overlap (in practice 4 to 5 μm). After recording and storing the images, the data acquisition scheme was continued with the next tilt-angle. To improve the SNR the ice was 'evaporated' from the high-dose areas *f1* and *f2* by means of an extended exposure to the electron beam.

4.12 Image processing

4.12.1 CTF determination and correction of tilted projections

The average defocus and the astigmatism for *f1* and *f2* at every tilt angle was determined via periodogram-averaging (Fernandez et al., 1997) and fitting a calculated CTF to the measured power spectrum in two dimensions by cross correlation (Mindell and Grigorieff, 2003). The focus condition of the exposure site was calculated by interpolating the focus values from sites *f1* and *f2*, assuming that the grid surface is flat over the distance between *f1* and *f2* (~10 μm). For the subsequent CTF correction, we applied the approach of Zanetti (2009). Figures 12 *A* – *C* depict the workflow schematically. Briefly, the image is divided into tiles of 32^2 pixels (*A*). For each tile, the defocus is calculated based on the position of the central pixel (*small red square*):

its distance *x* from the tilt-axis (*red dotted line*) and the respective tilt angle (*ψ*). A square box of 256^2 pixels is extracted from the image around each tile (*B*). The Fourier Transform of the box is calculated and corrected for the appropriate CTF by phase flipping. The central 32^2 pixels of the corrected box are pasted to their original position to give the corrected final image (*C*). Errors due to approximation of the tile to a flat sub-image can be reduced by choosing a smaller tile size at the expense of an increased computational time. The tilt axis direction was calculated during the alignments performed with the TOM-toolbox. The tilt angle was taken from the goniometer setting.

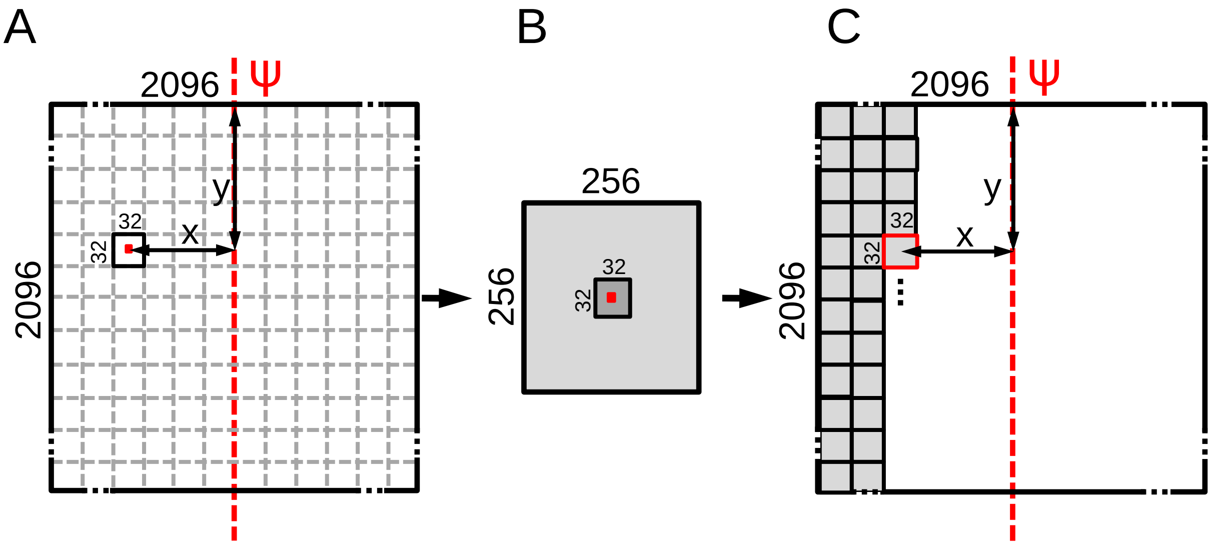

Figure 12: Schematical workflow for CTF correction of tilted projections. A. The 2096^2 pixel image is rasterized into 32^2 squares. The position of the center pixel (*red square*) relative to the tilt-axis (*red dotted line*) and the tilt-angle (*ψ*) determines the defocus value. **B.** An area of 256^2 pixels around the center pixel is CTF corrected and the central square of 32^2 pixels is pasted into the final image (**C.**).

4.12.2 Correction of the modulation transfer function (MTF)

Unfortunately, a measured MTF was not readily available for the Gatan 2k x 2k CCD-camera of the Tecnai Polara. To avoid downtime of the microscope, deconvolution was done with the determined function of an FEI Eagle 4k x 4k camera connected to another EM (Fig. 13, *red line*). Determination was done by edge analysis (Samei et al., 2005). Compared to the modeled MTF of the Gatan camera, determined by measuring the noise spectrum (‘pre-whitening filter’ (Sigworth, 2004), Fig. 13, *blue curve*), deconvolution of our data with the FEI Eagle-function is rather conservative.

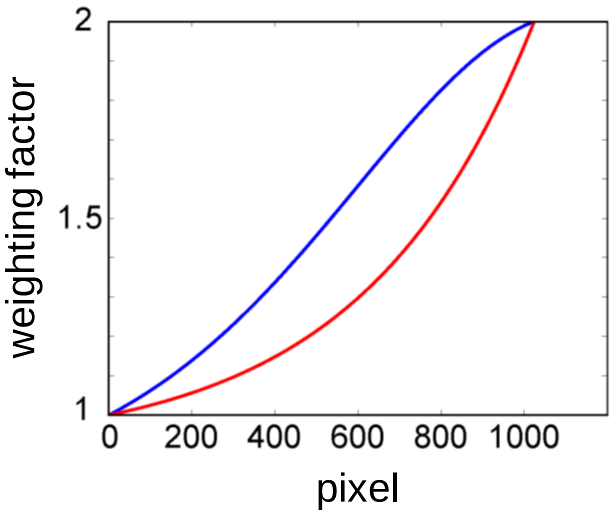

Figure 13: Comparison of the measured MTF of the 4k x 4k FEI Eagle CCD camera (*red curve*) with the modeled function of the 2k x 2k Gatan CCD camera of the Tecnai Polara (*blue curve*). The Gatan-MTF was modeled according the 'pre-whitening filter' approach of Sigworth (2004)

4.12.3 Reconstruction of tilt series

Alignment and reconstruction of tilt series were performed using the TOM-toolbox (Nickell et al., 2005) implemented in MATLAB (Mathworks, Natick, USA). Tilted images were aligned with gold beads as fiducial markers or via cross-correlation based methods ('feature tracking', (Sorzano et al., 2009)). Three-dimensional reconstructions were calculated using weighted back projection (WBP) or simultaneous iterative reconstruction techniques (SIRT; (Lakshminarayanan and Lent, 1979)). A nonlinear anisotropic diffusion algorithm was applied to reduce noise in survey tomograms (Frangakis and Hegerl, 2001). Three-dimensional data sets used for calculation of density profiles were not filtered.

4.12.4 Image analysis of the cell wall structures

The distances between the cell envelope structures were determined by averaged cross-sections of the cell walls. For this purpose, the tomograms were oriented such that the longitudinal axis of the cells was parallel to the x-y plane of a 3D coordinate system. Figure 14 shows the workflow in detail. Subvolumes of the whole reconstructions (*A*) that covered a long, preferably straight region of the cell wall were averaged in z. The z dimension of the subvolumes was kept small enough to prevent artificial blurring of the membrane because of the cylindrical shape of the cells. The resulting 2D projection was rotated to align the membranes parallel to the y axis (*B*). The image was separated into one-pixel-thick rows along the y-direction (*C*), which were aligned onto each other via cross-correlation to unbend the curved cell envelope traces (*D*). The resulting image was projected along the y direction (*E*) to obtain an averaged density profile across the cell envelope structures (*F*). In untilted projections of cryosections exhibiting sufficient contrast, the CTF was determined and corrected for to minimize optical aberrations introduced by the imaging conditions.

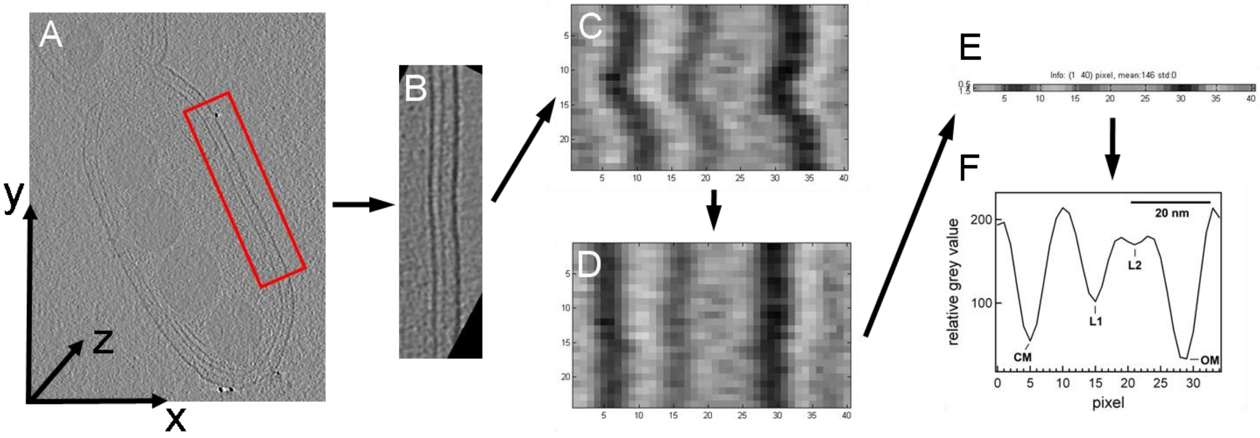

Figure 14: Workflow for measuring the dimensions and distances between the cell wall components. A. x-y slice from a tomogram of an *M. bovis* BCG cell. The red rectangle indicates a subvolume, containing a long and preferably straight region of the cell wall. **B**. The resulting 2D projection, aligned to the y-axis. **C.** and **D**.'Unbending' of the curved cell envelopes via cross-correlation. **E**. Projection from *D* along the y-axis. **F**. Calculated density profile as used for the measurements.

4.12.5 Averaging of subtomograms

Extraction, alignment, averaging and further image processing of subtomographic volumes were performed using the TOM-toolbox (Nickell et al., 2005) and the procedure tom_corr3D (Haller et al., 2009) which accounts for the *missing wedge* of the particles. Tomograms had to be filtered for manual picking to discern structures. Gray values were normalized. Docking of the x-ray structure into electron density maps was performed with Chimera (Goddard et al., 2007). The resolution was assessed by Fourier shell correlation (FSC; (Stewart et al., 1999)).

4.12.6 Visualization of electron density maps

Visualization and segmentation was performed using Amira 3.0-5.2 (TGS, Bordeaux, France) and Chimera (Goddard et al., 2007). Nonlinear anisotropic denoising (Frangakis and Hegerl, 2001) and Gaussian filtering was applied before segmentation when necessary. Final figure preparation and drawings were performed in Adobe Photoshop CS2 (Adobe, San Jose, USA).

5 Results

5.1 Cryo-electron tomography reveals the native architecture of bacterial cell envelopes

The cell envelope architecture was investigated in *M. smegmatis* mc^{2}155, *M. bovis* bacillus Calmette-Guérin (BCG), and, as a control, in *Escherichia coli* DH5α, with frozen-hydrated and otherwise untreated intact cells by cryo-electron tomography. Figure 15 *A* shows an electron microscope projection of *M. bovis* BCG imaged with subcritical electron dose conditions. The major cell envelope layers are discernible, and they are clearly recovered in the x-y slices extracted from the tomograms (Fig. 15 *B*). To evaluate the structural preservation of the cell wall in CET, *E. coli* was chosen as a reference organism. The location of the outer membrane close to the peptidoglycan (distance ≈ 7.5 nm; Fig. 15 *C*) and the width of the periplasm (≈ 16 nm) are consistent with the structure of periplasmic protein complexes such as Braun's lipoprotein, the flagellar basal body, and the TolC-AcrB assembly that serve as molecular rulers (Fig. 16 *A* and *B*; details see Table 12). This can be interpreted as evidence for accurate preservation of the native structure of the cell envelope in CET.

M. bovis BCG possesses a multilayered cell envelope structure (Fig. 15 *A* and *B*). The inner layer represents the cytoplasmic membrane, and the outer layer, the mycobacterial outer membrane (see below). The layers L1 and L2 cannot be assigned according to structural appearance alone. They likely represent structures related to the peptidoglycan-arabinogalactan-mycolate network visualized in their natural arrangement within the cell wall (see also Table 13).

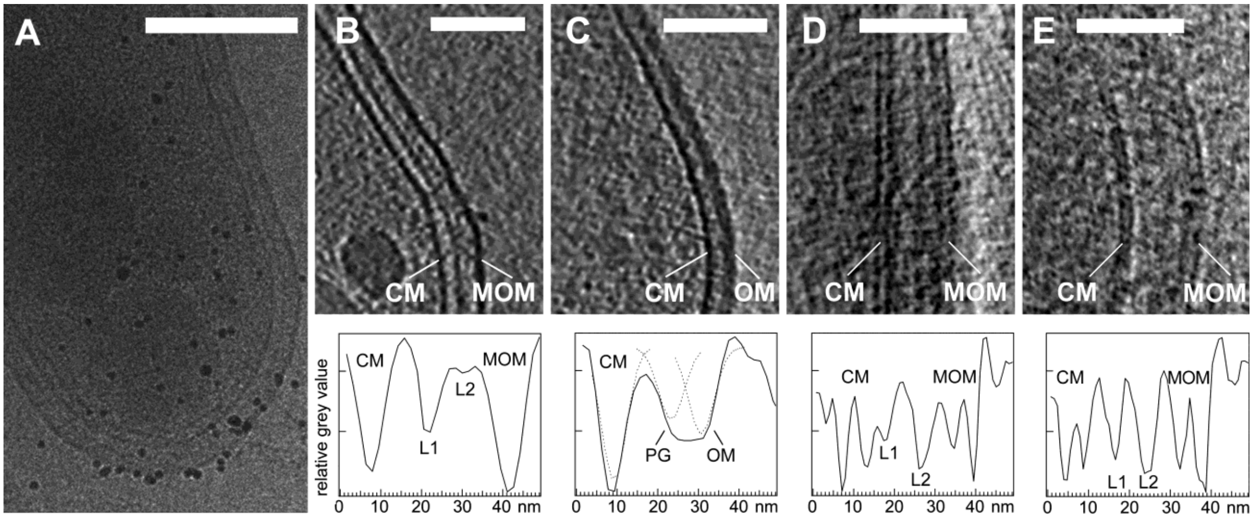

Figure 15: CET of *M. bovis* BCG (A, B, D), *M. smegmatis* (E), and *E. coli* (C). A. Intact cell rapidly frozen (vitrified) in growth medium and imaged by using low-dose conditions. Black dots represent gold markers. **B. – E.** Calculated x-y slices extracted from subvolumes of the three-dimensionally reconstructed cells and corresponding density profiles of the cell envelopes. The profiles were calculated by averaging cross-sections of the cell envelopes along the x-y direction in 20 independent slices. A total of 10,000 cross sections for the mycobacteria and 8,000 for *E. coli* were aligned by cross-correlation before averaging. The fitted Gaussian profiles in C (dashed curves) indicate the positions of the peptidoglycan (PG) and the outer membrane (OM). **D.** and **E.** Subtomograms recorded at nominal -6 μm defocus and reconstructed without noise reduction. CM, cytoplasmic membrane; L1 and L2, periplasmic layers; MOM, mycobacterial outer membrane. (Scale bars: *A*, 250 nm; *B* and *C*, 100 nm; *D* and *E*, 50 nm.)

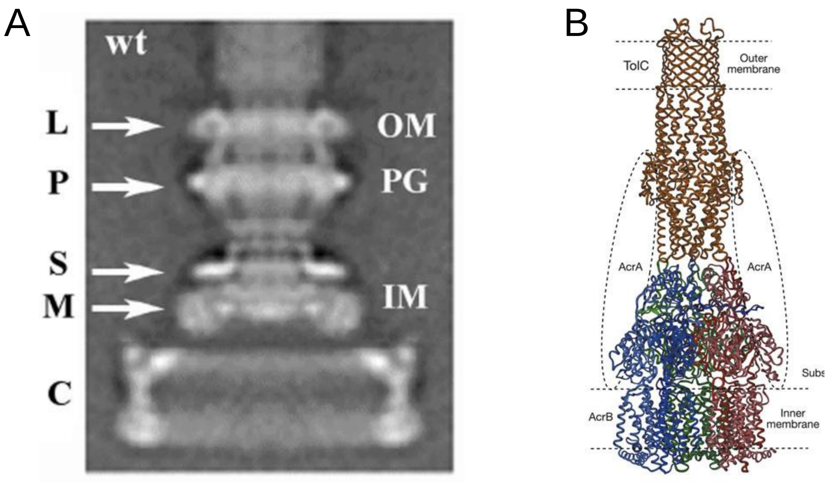

Figure 16: A. Averaged image of a basal body from a *Salmonella enterica* wild-type strain (SJW880), as derived by single-particle cryo-electron microscopy (Thomas et al., 2001). The L, P, S, M, and C rings are labeled. The positions of the outer membrane (OM), peptidoglycan (PG), and inner membrane (cytoplasmic membrane; IM) are marked. **B. Structure of the TolC-AcrB assembly of *E. coli*** (Murakami et al., 2002). Both structures served as molecular rulers. See Table 12 for dimensions.

Table 12: Characteristic distances in the cell envelope of *Escherichia coli*.

Characteristic distance	Source of data			
	Cryo-electron tomography,[*] nm	Cryosections,[†] nm	Periplasmic proteins	
			Size, nm	Molecular ruler
Center-to-center				
CM - OM	22.0	27.4[‡]	24	Basal body (M- to L-ring)[§]
CM – PG	14.5		16	Basal body (M- to P-ring)[§]
PG – OM	7.5	12.0[‡]	8	Basal body (P- to L-ring)[§]
Surface-to-surface (gap)				
CM – OM	15.7[¶]	21.0±2.7	18	Basal body (M- to L-ring)[§]
			17	TolC-AcrB assembly[‖]
CM – PG	8.4[¶]		10	Basal body (M- to P-ring)[§]
PG – OM	<2[¶]	5.3±0.9	3.5	Basal body (P- to L-ring)[§]
			3.0	Lipoprotein[**]
Thickness				
CM	≈6[††]	5.8±0.4		
PG		6.5±0.5		
OM		6.9±1.0		

CM, cytoplasmic membrane; PG, peptidoglycan; OM, outer membrane.
*This study.
†(Matias et al., 2003).
‡Calculated from surface-to-surface distances, taking into account the average thickness of membranes or the peptidoglycan.
§(Thomas et al., 2001).
¶Calculated from centre-to-centre distances, taking into account the thicknesses of membranes or the peptidoglycan.
‖(Murakami et al., 2002)
**(Braun et al., 1976)
††Width at half height of the averaged membrane profile.

5.1.2 The outer layer is revealed as a lipid bilayer in cryo-electron tomograms

In the case of intact cells, membranes are not usually resolved as lipid bilayers in CET because of cell thickness, the limited number of projections, and the focus conditions. To clarify the membrane structure further, the focus conditions for data recording were adapted, i.e. the values were raised from below -10 *µ*m to above -6 *µ*m and the tomograms were analyzed to the full resolution available. The x-y slices and the averaged density profiles in Figure 15 *D* and *E* now clearly reveal the bilayer structure of the cytoplasmic membrane with an apparent total thickness of ≈ 7 nm. Concomitantly, the fine structure of the outer membrane of *M. bovis* and *M. smegmatis* is also rendered visible as a bilayer. It is ≈ 8 nm thick, and thus only 15% thicker than the cytoplasmic membrane. The term *mycobacterial outer membrane* (MOM) is used to distinguish the structure from the outer membrane of Gram-negative bacteria.

To probe the nature of the bilayer, *M. smegmatis* cells were incubated with 1% octyl β-glucoside before freezing. After treatment and resuspension in detergent-free buffer, the cells became extremely hydrophobic and aggregated strongly. This phenomenon is consistent with the removal of lipids that expose a hydrophilic head group, such as polar glycolipids and glycopeptidolipids, and the exposure of lipids with hydrophobic ends, such as the covalently bound mycolic acids. Cells that could be resuspended were virtually intact and exhibited limited detergent effects, as observed by CET. Similar effects have never been found in untreated cells. Figure 17 *A*, *E* and *F* shows an undisturbed cell wall region comprising four cell envelope layers similar to the architecture of untreated *M. smegmatis* (Fig. 15), as well as the bilayer structure of the mycobacterial outer membrane. The lipidic nature of the bilayer is demonstrated by the detergent effects, which disturb the membrane structure and apparently dissolve extractable lipids (Fig. 17 *B-D*).

It is remarkable that the inner membrane is dissolved in regions where the detergent had affected the structure of the outer membrane. Octyl β-glucoside obviously made the mycobacterial outer membrane penetrable and destroyed the inner membrane. Also, the periplasmic layers appear to become affected. Degradation of structures by lytic processes cannot be excluded in places where the cytoplasm infiltrated the periplasm. The remaining layer below the outer membrane-detergent composite in Figure 17 *B-D* likely represents the covalently linked mycolic acids that cannot be removed by detergents. The putative mycolic acid layer still shows local contacts to the detaching membrane material (Fig. 17 *C*), but it is not obvious whether the layer was a constituent of the mycobacterial outer membrane.

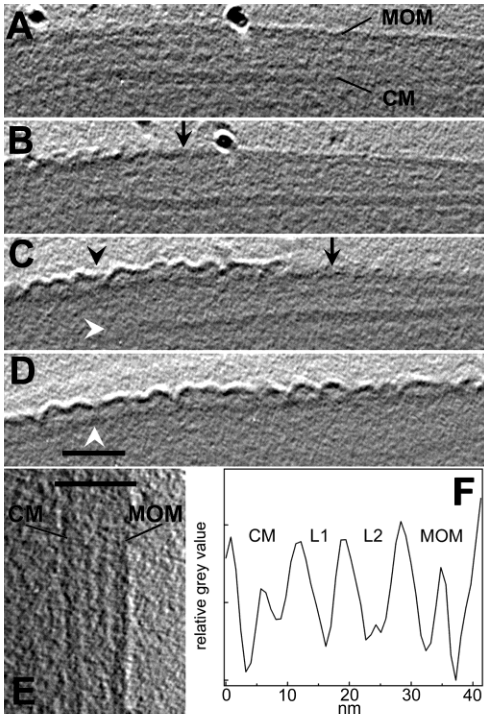

Figure 17: CET of intact *M. smegmatis* treated with octyl β-glucoside. A – D. x-y slices of the tomogram without noise filtering. **A.** Region of the apparently intact mycobacterial outer membrane (MOM), cytoplasmic membrane (CM) and periplasmic layers L1 and L2 as marked in **F.** The prominent black dot represents a gold marker used for alignment purposes. **B. – D.** Slices of cell wall positions with successively affected MOM (black arrowhead) and dissolved CM (white arrowhead in C) because of the treatment with the detergent. Black arrows indicate the approximate border between detergent-affected and apparently undisturbed regions of the MOM. **D.** The white arrowhead indicates the putative mycolate layer. (Scale bar: 50 nm.) **E.** Enlarged slices of the cell envelope illustrating the bilayer structure of the CM and the MOM. The bar indicates the width of the profile displayed in **F.** The averaged profile was calculated according to the procedure described in Ch. 4.12.4.

5.1.3 Vitreous cryosections confirm the bilayer structure of mycobacterial outer membranes

Since membrane bilayer structures have not previously been rendered visible in tomograms of intact cells, the attempt was undertaken to reproduce the results by means of thin, frozen hydrated sections. Due to the reduced sample thickness a higher resolution can be expected and because the total tolerable dose can be applied on one single projection a better contrast is achieved. The resulting loss of information in the z-dimension can be neglected since the arrangement of the cell wall layers can be resolved in the x-y plane and should be homogenous around the cell. Cells of both *M. smegmatis* and *M. bovis* were rapidly frozen under high pressure (cf. Ch. 4.11.1.4; (Al-Amoudi et al., 2004)).

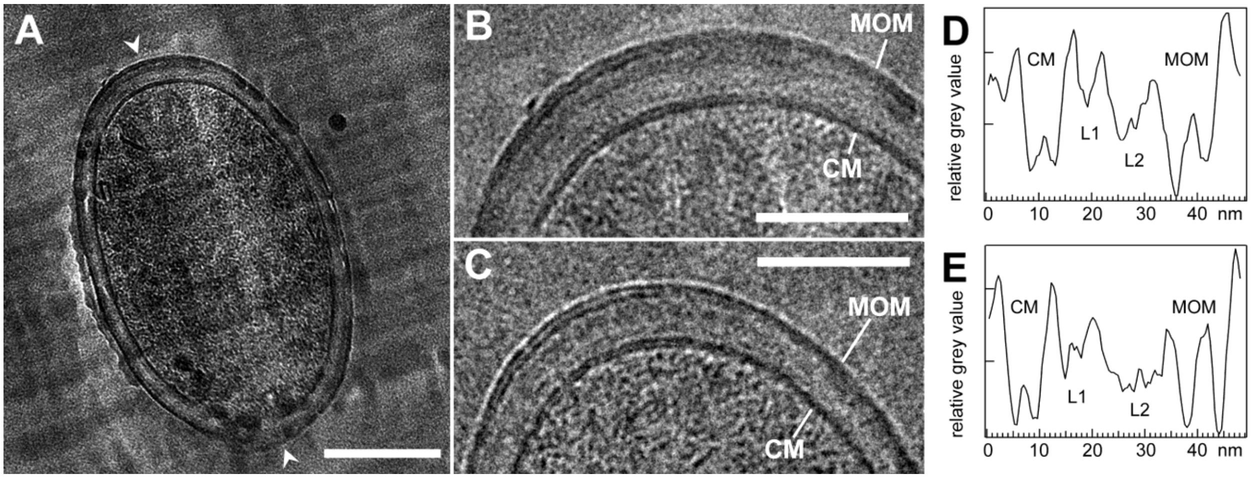

Figure 18: Cryo-electron micrographs of vitreous cryosections from mycobacteria. The sections have a nominal thickness of 35 nm. **A.** Cross-section of an *M. smegmatis* cell deformed by the cutting process. Regions perpendicular to the cutting direction (arrowheads) were used for further analyses. (Scale bar: 200 nm.) **B.** Cell envelope of *M. smegmatis* (subarea from *A*). **C.** Cell envelope of *M. bovis* BCG. (Scale bars: 100 nm.) **D.** and **E.** Averaged profiles from the cell envelopes of *M. smegmatis* (*D*) and *M. bovis* BCG (*E*). CM, cytoplasmic membrane; L1 and L2, domain-rich periplasmic layers; MOM, mycobacterial outer membrane. Note that the distances between the membranes and layers are influenced by the cutting process. The bilayer structure of the CM and the MOM is discernible (*B* – *E*). Images are corrected for the contrast transfer function with fitted defocus values of -6.4 μm (*B*) and -6.7 μm (*C*).

Sections with a nominal thickness of 35 nm revealed similar substructures in the periplasmic space of both species and suggested that the periplasmic layers comprise several domains (Fig. 18). The bilayer structure of the cytoplasmic membrane as well as of the outer membrane is clearly resolved in regions perpendicular to the cutting direction. These are disturbed least by compression (Matias et al., 2003). The results confirm the structure of the mycobacterial outer membrane in Figures 15 and 17, having an overall thickness of ≈ 8 nm in both *M. smegmatis* and *M. bovis*. Because of the observed dilatation of structural detail by ≈ 20% perpendicular to the cutting direction in the periplasm of *E. coli* (see details in Table 12), the thicknesses of membranes and periplasmic layers as determined in cryosections from mycobacteria represent upper values (Tab. 13). The identical appearance of the two areas of high contrast in the bilayer structures (Fig. 18 *B* and *C*) indicates that the head group regions of the outer membrane exhibit similar mass (electron) densities that result in the same image (phase) contrast in the microscope. Thus neither the mass distribution of lipid head groups in the two leaflets nor their cumulative thickness normal to the membrane plane gives rise to a clear morphological asymmetry as it is assumed in the current models of the mycobacterial cell wall (Brennan and Nikaido, 1995; Nikaido et al., 1993; Rastogi et al., 1991).

Table 13: Characteristic distances in mycobacterial cell envelopes derived from tomograms and vitreous sections.

Charcteristic distance	*Mycobacterium smegmatis*, nm	*Mycobacterium bovis* BCG, nm
Center-to-center from tomograms		
CM – MOM	28	27 (34)*
CM – L2†	18	16 (23)
CM – L1†	10	7 (14)
L1 - MOM	18	19 (20)
L2 - MOM	10	10 (11)
L1 – L2	8	9 (9)
Thickness from vitreous sections‡ (tomograms)§		
CM	7.0 (7.5)	7.0 (8.0)
MOM	7.5-8.5 (8.0)	7.5-8.5 (7.5)
L1	4.0 (4)	6.0 (5)
L2	7.0 (5.5)	≈11¶

CM, cytoplasmic membrane; MOM, mycobacterial outer membrane.
*Values in parentheses determined from cells in nongrowing cultures.
†L1, L2: periplasmic layers assigned to the peptidoglycan-arabinogalactan network.
‡Average values and ranges determined from images.
§Width at half height from averaged profiles.
¶Including variations by subdomains.

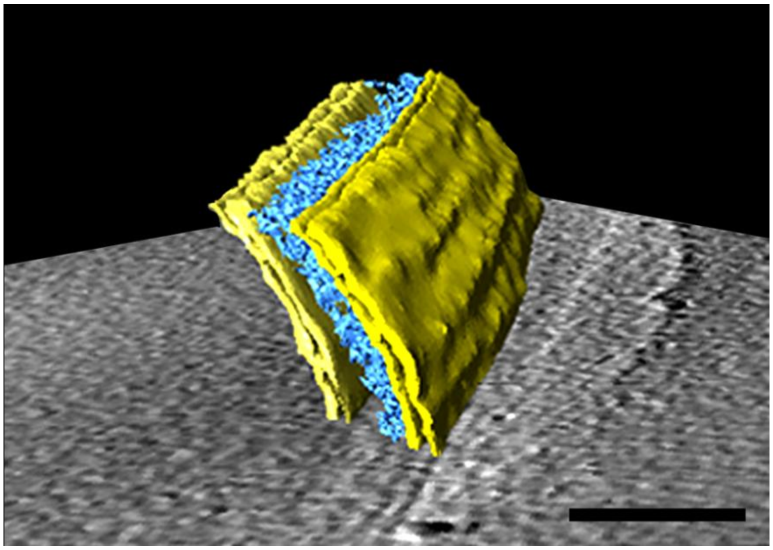

Figure 19: 3D-representation of the cell wall of *M. bovis* BCG as derived from tomograms of intact cells. The periplasmic space between the MOM (*dark yellow*) and the CM (*bright yellow*) contains the layers of the arabinogalactan-peptidoglycan polymer (indicated in *blue*). (Scale bar: 50 nm).

5.1.4 The asymmetric structure of the outer membrane of *Escherichia coli* is visualized in cryo-electron tomograms

To probe if it is indeed possible to visualize an apparent asymmetry in the structure of a membrane by cryo-electron tomography of frozen-hydrated intact cells, *E. coli* cells were treated and imaged according to the mycobacteria before. The outer membrane of *E. coli* has a highly asymmetric architecture, with the outer layer consisting of lipopolysaccharides (LPS) while the inner layer is made up from phospholipids (Matias et al., 2003). LPS have a larger number of phosphates per unit area than a typical phospholipid and it can thus be expected that LPS should have more inherent contrast in the image. LPS also possesses more carboxyl- and phosphate groups, which interact more strongly with Mg^{2+}- and Ca^{2+}-ions than phospholipids, and these complexed metal ions should also increase the contrast of the outer face of the OM. Figure 20 shows an 2.8 nm thick x-y slice of an cryo-electron tomogram of an *E. coli* cell. The multilayered structure of the cell wall is clearly resolved (Fig. 20 *A*) and the bilayer structure of the cytoplasmic and outer membrane is shown in the enlarged section (arrows Fig. 20 *B*). The outer layer of the outer membrane appears thicker and with higher contrast than the inner one, what is emphasized in the averaged density plot in Figure 20 *C*. According to these results, a strongly asymmetric composition of lipid headgroups in the mycobacterial outer membrane, as implied by current cell wall models (Minnikin, 1991), should actually be visible in cryo-electron tomograms.

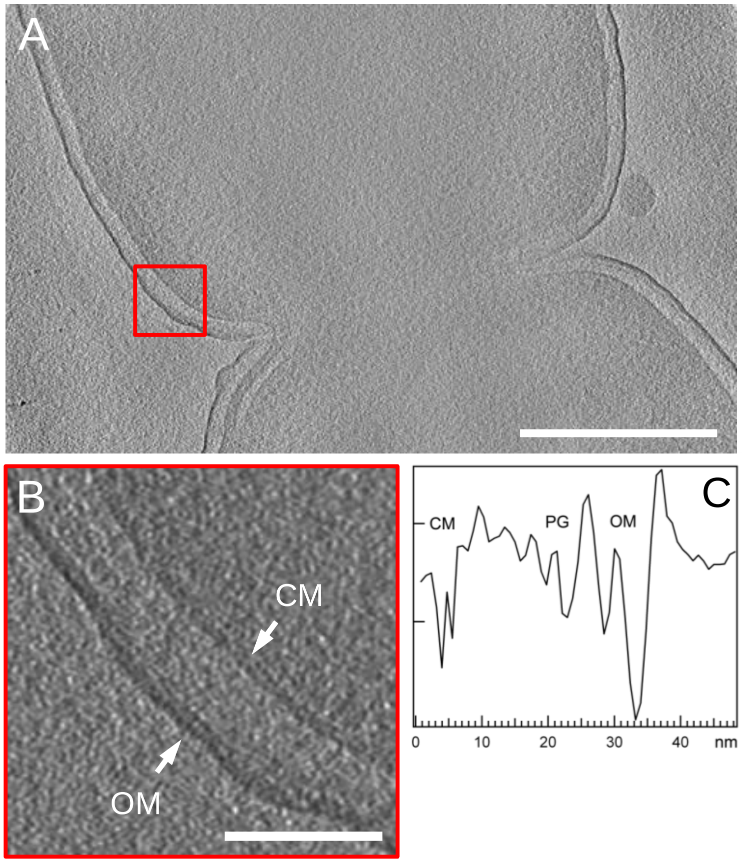

Figure 20: CET of intact *E.coli* cells showing the asymmetric architecture of the outer membrane. A. Calculated 2.8 nm thick x-y slice of a three-dimensionally reconstructed *E. coli* cell. The multilayered structure of the cell wall is clearly visible. *Red* square: enlarged area shown in *B*. (Scale bar: 200 nm.) **B.** The cytoplasmic membrane and the outer membrane are resolved as bilayers. The outer layer of the outer membrane appears thicker and with higher contrast. (Scale bar: 50 nm.) **C.** Averaged density plot of the cell wall. CM, cytoplasmic membrane; PG, peptidoglycan; OM, outer membrane.

5.1.5 Mycolic acids are an essential part of the outer membrane in *Corynebacterium glutamicum*

A mycolic acid-deficient mutant is required to assess the contributions of these lipids to the outer membrane. Such mutations are lethal in mycobacteria, whereas a mycolic acid-deficient mutant of the related species *Corynebacterium glutamicum* is viable (Portevin et al., 2004). Both, mycobacteria and corynebacteria belong to the suborder *Corynebacterinae* (Pascual et al., 1995). By *in silico* analysis of various mycobacterial genomes the gene product Pks13 was identified as the enzyme responsible for the final condensation step in mycolic acid biosynthesis. It contains four catalytic domains required for the condensation reaction. Deletion in the *pks13* gene resulted in a *Corynebacterium glutamicum* strain deficient in mycolic acid production, whereas it was able to produce the fatty acids precursors (Portevin et al., 2004). The mutant strain also displayed an altered cell wall structure. Therefore, wild-type *C. glutamicum* and the mycolic acid free mutant Δ*pks13* were investigated. Tomography of frozen-hydrated intact cells was not possible due to the thickness of the corynebacteria and the resulting limitations for CET. Thus, vitreous cryosections were prepared and analyzed. Figure 21 demonstrates that *C. glutamicum* also possesses an outer membrane, as shown for *M. smegmatis* and *M. bovis* BCG (Figs. 15 and 18). Importantly, the outer membrane is absent in the Δ*pks13* mutant (Fig. 21 *B*). The mutant cell wall is thinner by 5 – 8 nm (mean: 6.4 nm; Fig. 21 *B* and *D*), which corresponds to the dimension of the missing bilayer structure. These results establish that mycolic acids are indispensable for the structural integrity of the outer membrane. This finding is consistent with the key role of mycolic acids for the cell wall permeability barrier in *C. glutamicum* (Gebhardt et al., 2007). Furthermore, the periplasmic constituents are also organized in layers, indicating the formation of domains similar to those observed in mycobacteria (Fig. 18).

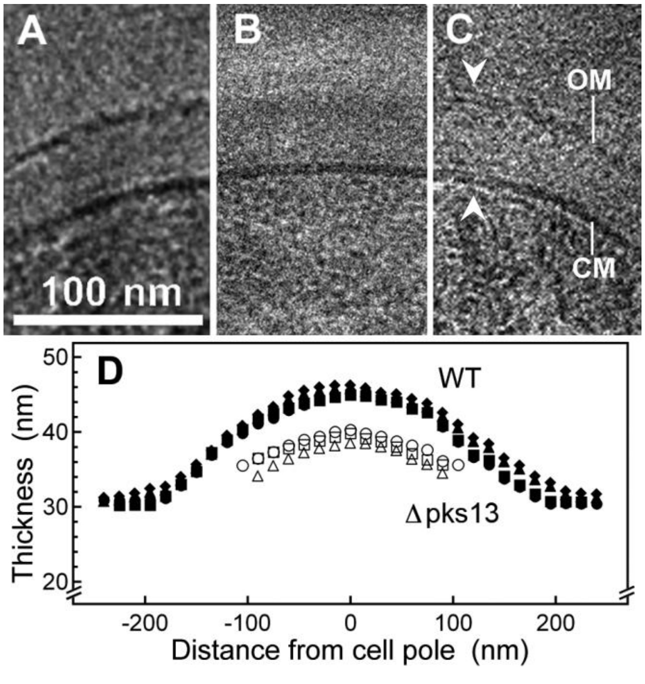

Figure 21: Cryo-electron micrographs of vitreous cryosections from *C. glutamicum*. The sections have a nominal thickness of 35 nm. **A** and **C**. Wild-type cells imaged at high (A) and low (C) defocus. The bilayer structure of the cytoplasmic membrane (CM) and the outer membrane (OM) is resolved in minimally compressed parts of the cell envelope (arrowheads). **B.** Projection of an ultrathin section of the mycolic acid-lacking mutant *C. glutamicum* Δ*pks13* at low defocus. **D.** Thickness of the cell walls determined from several cells as measured from the surface of the CM to the outer surface of the cell wall. In images of the mutant cell wall, the cell boundary was identified by the change from higher to lower contrast (background). The center of the thickness curves corresponds to the position of the cell envelope “poles” that are oriented perpendicular to the cutting direction. Filled symbols, wild-type cells; open symbols, mutant cells.

5.2 CET with FIB-micromachined *M. smegmatis* cells

5.2.1 Specimen thickness and milling approaches

Adequate thinning procedures are a prerequisite for obtaining a useful resolution by cryo-electron tomography with many cellular samples. By means of ultrathin cryo-sections it was possible to confirm the results concerning the cell wall structures obtained by tomography of 'intact' cells. Using CET for further analysis of macromolecular complexes located in the mycobacterial cell envelope would be of enormous interest. The major drawbacks of cryo-sectioning, the unavoidable compression of the sample in the cutting direction, and the limited possible thickness of the sections and thus the loss of information in z-direction, restrict the use of this method considerably. The already mentioned difficulties in preparing tomograms from ultrathin cryo-sections pose further problems. Promising results with the use of a focused ion beam for the preparation of biological samples for cryo-microscopy were already attained some years ago (Marko et al., 2007). Thus we attempted to extend the method for samples used for tomography. Specimen thicknesses of about 500 nm or less would be best to account for the considerable 'thickness' increase during sample tilting (Fig. 22 *A*). However, the preparation of suitable thin samples for electron tomography should yield extended electron transparent regions, covering a maximum volume of cellular space. In FIB-micromachining, the 'transparency length' is dependent on the incident angle of the ion beam (Fig. 22 *Aa*; (Rigort et al., 2010)). In order to generate large enough transparent areas, shallow angles (<10°) are preferable. The major disadvantage of this approach is that cellular features in the z-axis are lost ('thinned out') over a relatively large area. A solution to this problem would be 'parallel milling' (Fig. 22 *Ba*), but this technique is difficult and demanding; the carbon support of the EM grids is never perfectly flat, what is even more serious a problem with ice-embedded cells. The carbon layer very often forms 'basins' across the meshes of the grid, so that the cells are 'shadowed' by the grid bars when tilted parallel to the ion beam. They are thus inaccessible for milling (Fig. 23 *C*) . A solution would be halving frozen grids and making the cutting edge accessible for the parallel milling approach (Fig. 23 *D*).

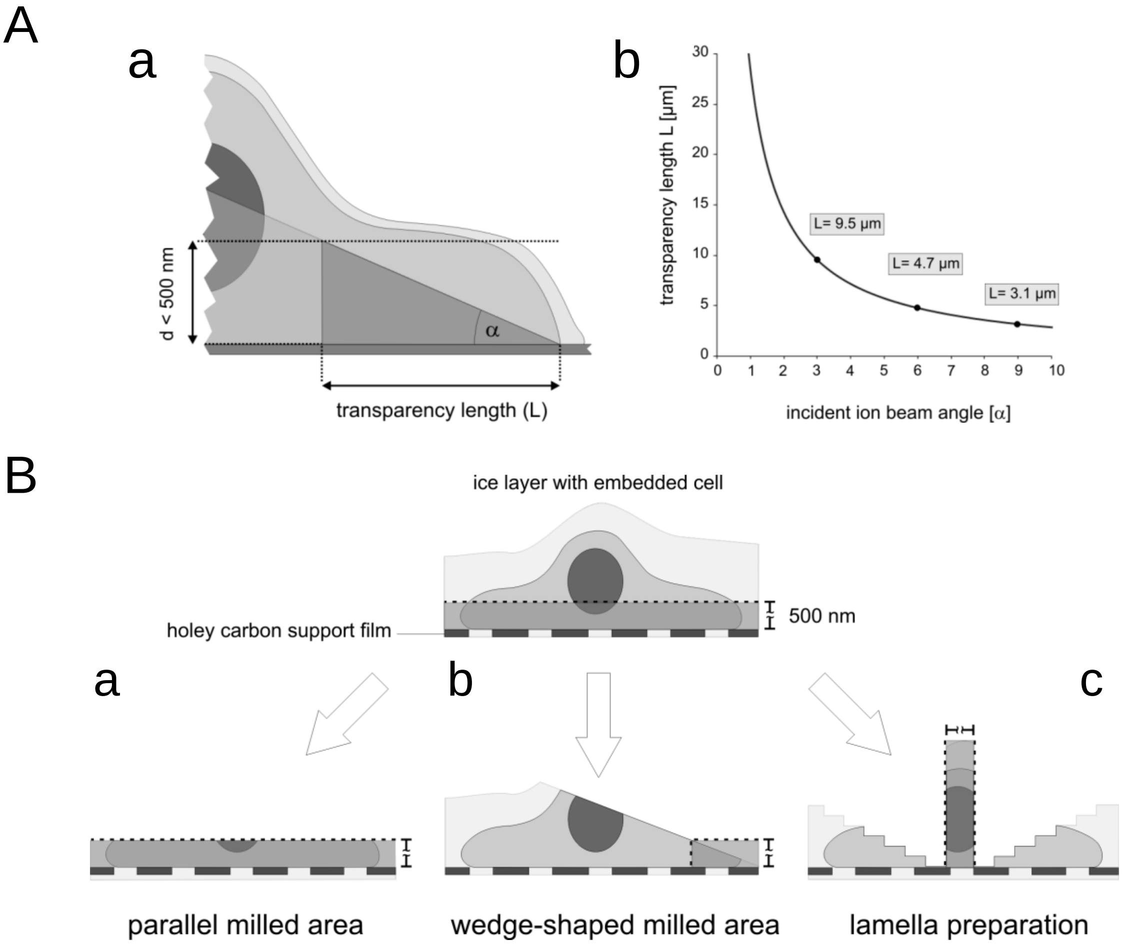

Figure 22: A. Definition of the transparency length for ‘efficient’ CET (Rigort et al., 2010). (a) Schematic representation of a cut-away of a cell attached to a carbon support film and embedded in a thin layer of vitreous ice. The drawing illustrates how the angle [α] of the incident ion beam defines the cellular area that is accessible for tomographic data acquisition. The dimension in the beam direction is referred to as the ‘transparency length’ [L]. A thickness of < 500 nm is considered to be optimal for sufficient electron transmission especially at high tilt angles where the projected thickness increases. **(b)** Graph showing the ‘transparency length’[L] in dependence of small (< 10°) incidence angles [α]. **B. Different strategies of FIB-micromachining of vitrified cellular samples (Rigort et al., 2010).** The cell is lying on the carbon support film of an EM grid and embedded in vitreous ice. The thin layer (delineated by the dashed line) represents the desirable specimen thickness appropriate for CET (< 500 nm). **(a) Parallel milling.** The incident ion beam is parallel to the EM grid surface. This approach usually involves halving a frozen grid and is demanding, as the milled areas on the halved grid are extremely fragile and are lost very easily during the subsequent transfer into the TEM. **b. Wedge-shaped milling.** The ion beam impinges on the frozen specimen at an oblique or ‘grazing’ angle. This approach is the most feasible since the grid remains intact and the fragile carbon film stays fully supported**. c. Cryo-lamella preparation.** The frozen specimen is milled to expose a thin lamella, thereby preserving cellular features along the z-dimension. Removal and reorientation of the lamella is necessary for subsequent analysis in the TEM. At present, a lift-out option for cryogenic lamella preparations is not available.

In a number of experiments the grids were cut after plunge freezing with a precooled scalpel in the cryochamber of the Leica FC6 ultramicrotome, set to -160°C. However, although the cutting process was successful, due to the lacking support for the fragile carbon film at one side of the square, almost all of the milled areas broke away and were lost during the transfer of the grid into the TEM cartridge. The approach of milling free-standing lamellas as commonly practiced in material sciences (Fig. 22 *Bc*) is currently not feasible, because the transfer of the lamella at cryogenic temperatures is a technical challenge that still remains to be solved.

5.2.2 Wedge-shaped milling results in areas thin enough for CET

Due to the problems with the parallel approach, an incident ion beam angle of approximately 10° was used for thinning of the mycobacteria. Milling was performed with 30 keV at an ion current of only 10 pA. Approximately 30 μm^3 of material was removed within five minutes, corresponding to a milling rate of 0.1 μm^3 s^{-1}. By means of electron energy loss spectroscopy (EELS) log-ratio method (Malis et al., 1988), and taking a total inelastic mean free path length of λ = 300 nm at 300 keV for vitreous ice (J.M. Plitzko, personal communication), the thickness of the areas of interest in the milled wedges was assessed to 300 – 400 nm (Fig. 24 *C* and *D*). The amorphous state of the ice after micromachining was verified by electron diffraction, which showed the characteristic diffuse ring of vitreous ice. In comparison to sections of the same bacteria obtained by cryo-ultramicrotomy (Fig. 24 *A*), where compression in the cutting direction leads to structural artifacts, the bacteria thinned by the FIB do not exhibit any compression (Fig. 24 *B*) or other structural damage. A regularly appearing effect of thickness variation is shown in Figure 24 *E*. The surface of the milled areas is non-uniform and exhibits a streak-like pattern (white asterisks) due to varying milling efficiency. However, the structure of the ice-embedded cell is not influenced by this effect. The results of tomographic reconstructions of milled *M. smegmatis* cells (Fig. 24 *G*) are in excellent accordance with the data of cryo-tomograms of intact cells and TEM-projections of vitreous sections (cf. Ch. 5.1). The layered architecture of the cell wall is clearly resolved (Fig. 24 *H*), and the fine structures of the cytoplasmic membrane (CM) and the mycobacterial outer membrane (MOM) are rendered visible as bilayers. The thicknesses of both membranes, OM and MOM, are ≈ 6.5 and ≈ 8 nm, respectively, as determined from the averaged density plots. They agree with the measured

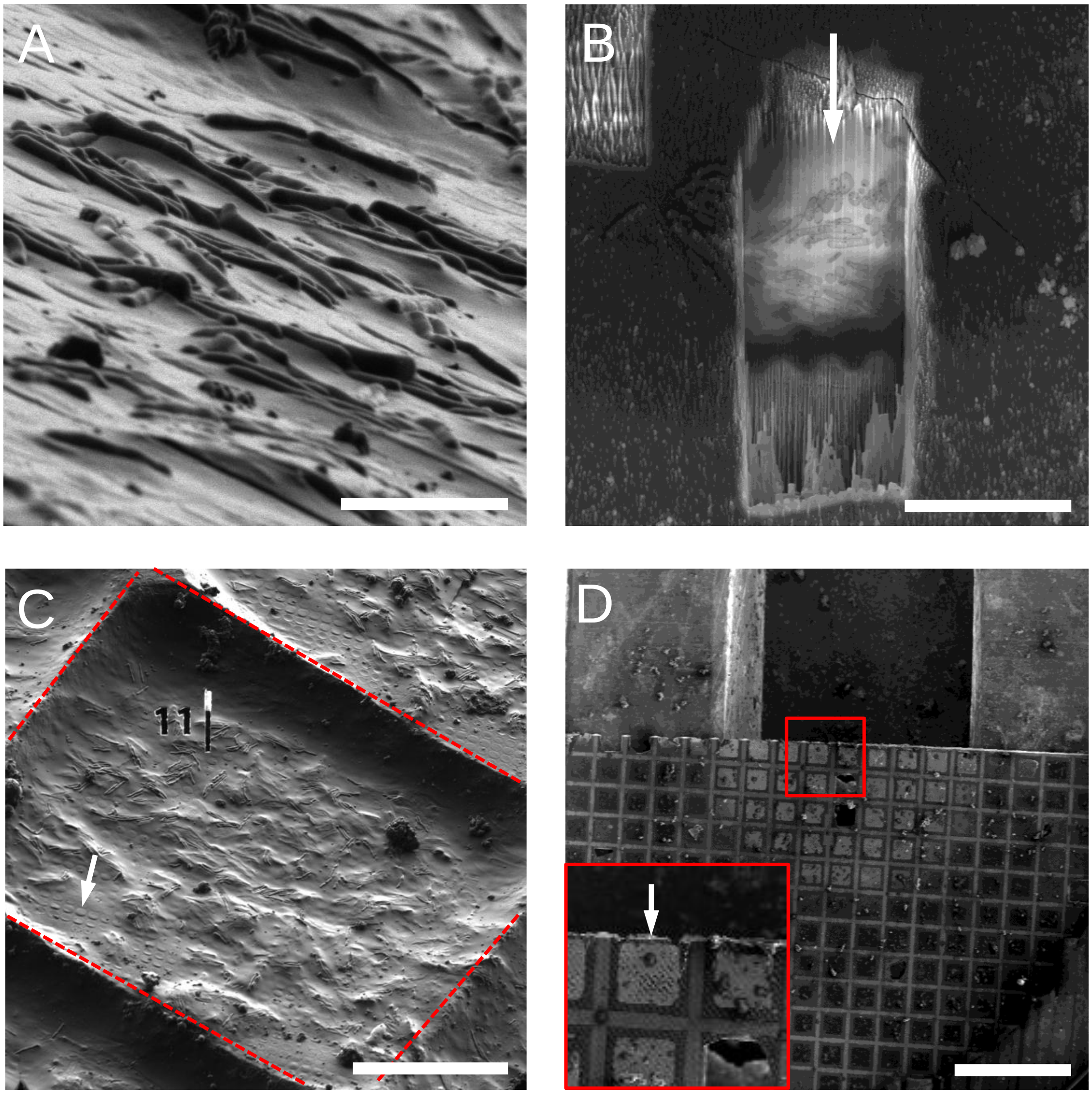

Figure 23: Approaches of FIB-micromachining of frozen-hydrated *M. smegmatis* cells All samples were prepared by plunge freezing and transferred to the SEM/FIB under cryogenic conditions (cf. Ch. 4.11.1.3 and 4.11.1.6). **A. Cryo-scanning electron micrograph of vitrified *M. smegmatis* cells on an EM grid.** The hydrophobic nature of their cell walls (Deshayes et al., 2005) makes them protrude from the vitreous ice layer. (Scale bar: 5 μm.) **B. Wedge milled into a sample of *M. smegmatis* cells embedded in vitreous ice.** The arrow indicates the direction of the incident beam. Thinned cells are visible on the wedge surface. (Scale bar: 10 μm.) **C. *M. smegmatis* cells embedded in vitreous ice on an EM grid.** The red dotted lines show the bars of the EM grid. The grid is covered by a 'holey' carbon film as specimen support (white arrow). The obvious 'basin' formed by the film prevents parallel milling. The number (11) and the straight line were milled into the sample and served for orientation purposes in the TEM. (Scale bar: 40 μm.) **D. 'Halved' grid to enable parallel milling.** Inset: enlarged area from the red square. The thick gridbar was cut away and the area behind the cutting edge is accessible for parallel milling. (Scale bar: 500 μm.)

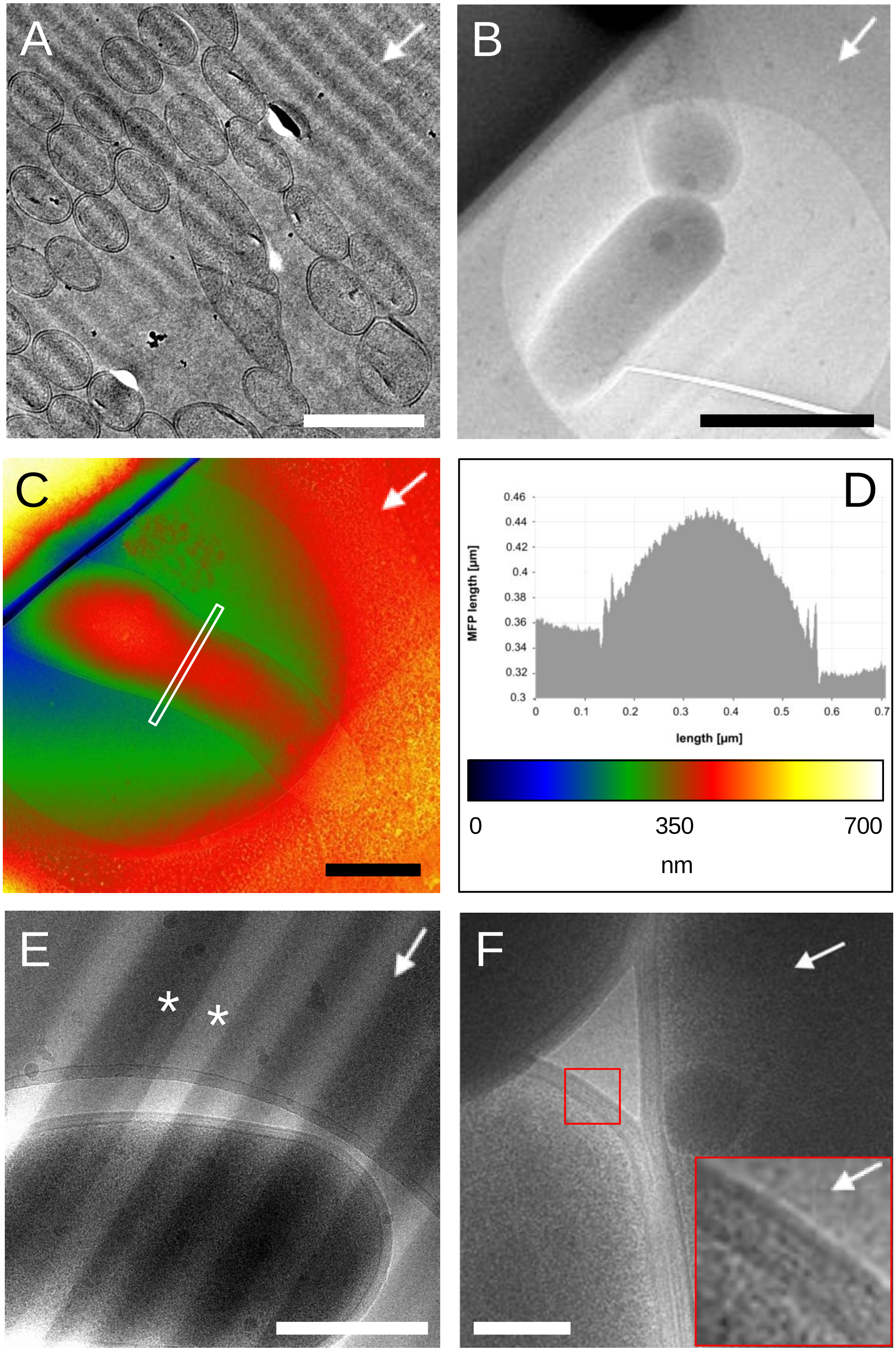
A
B
C
D
0.46
0.44
0.42
0.4
0.38
0.36
0.34
0.32
0.3
MFP length [µm]
0
0.1
0.2
0.3
0.4
0.5
0.6
0.7
length [µm]
0
350
700
nm
E
*
*
F

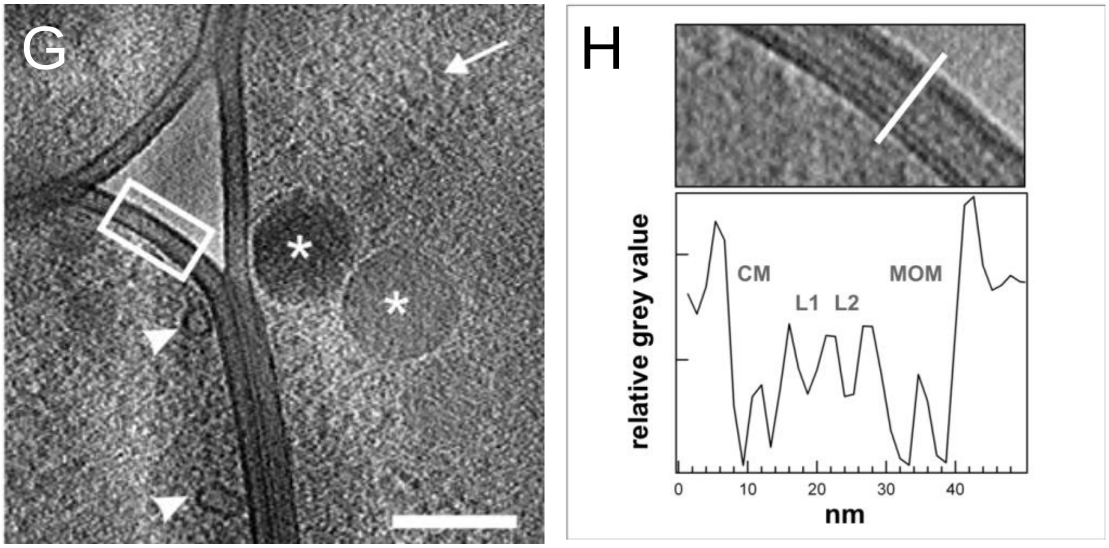

Figure 24: FIB micromachining of frozen hydrated *M. smegmatis* cells. A. TEM projection of an ultrathin cryo-section (nominal thickness: 50 nm) from *M. smegmatis* as obtained by cryo-ultramicrotomy. Compression of the cells in the cutting direction (white arrow) is clearly visible (distorted cross-sections). The striped pattern perpendicular to the cutting direction is caused by 'chatter', another typical artifact of cryo-sectioning . (Scale bar: 5 μm.) **B.** TEM projection image from FIB- micromachined *M. smegmatis* cells. The dark edge in the upper left corner depicts the milling edge. (Scale bar: 500 nm.) **C.** and **D.** Thickness determination based on the electron energy loss spectroscopy (EELS) log-ratio method (Malis et al., 1988). **C.** 'Heat-map' representation of the EELS log-ratio of a TEM-projection of a FIB-milled *M. smegmatis* cell. (Scale bar: 500 nm.) **D.** Thickness profile from the white rectangle in C. A total inelastic mean free path length of $\lambda = 300$ nm at 300 keV was assumed for vitreous ice. **E.** TEM projection image exhibiting a streak-like pattern on the surface of the milled area (white asterisks). Most likely caused by preferential or anisotropic milling (Heymann et al., 2006). **F.** 0°-projection image from a tomographic recording. The fine-structure of the cell wall is perfectly preserved even in areas perpendicular to the milling direction, indicated by the white arrow. (Scale bar: 100 nm.) **G.** Slice from a tomographic reconstruction. The larger vesicular objects (asterisks; 'lipid-bodies', (Waltermann and Steinbüchel, 2005)) demonstrate the absence of structural deformation. Small vesicular structures close to the CM (arrowheads) become apparent in the thinned cell. Milling direction is indicated by the white arrow. (Scale bar: 100 nm.) **H.** Enlarged area from E. (white rectangle). The structure of the *M. smegmatis* cell envelope can be discerned in more detail. The averaged density plot reveals the double layered structure of the cytoplasmic membrane (CM) as well as the mycobacterial outer membrane (MOM), and the periplasmic layers (L1, L2).

values from the tomograms of intact cells (details see Table 14). The whole appearance of the cell wall is more 'regular' compared to the data from the intact cells or the cryo-sections. Likewise, the periplasmic structures L1 and L2 are distinct layers, with L2 appearing thinner than in the previous data (≈ 40% compared to L2 in tomograms of intact cells), which might be an effect of the maturity of the cell. Moreover, small sized, delicate structures, e.g. vesicles ranging from ≈ 6 to 60 nm are clearly recognizable within the cytoplasm of the thinned mycobacteria (white arrowheads and asterisks in Fig. 24 *G*). The larger spherical structures resemble ‘lipid bodies’, known as intracellular storage compartments for lipids and lipophilic compounds (Daniel et al., 2004; Waltermann and Steinbüchel, 2005).

Table 14: Characteristic distances in the cell envelope of *M. smegmatis* derived from tomograms of cells prepared by FIB-micromachining in comparison to tomograms from intact cells and TEM-projections of vitreous sections.

Charcteristic distance	Dimensions of the cell envelope, nm		
	FIB	Intact cells	Vitreous sections[‡]
Center-to-center			
CM – MOM	26	28	29
CM – L2[†]	15	18	17
CM – L1[†]	8	10	9
L1 - MOM	18	18	20
L2 - MOM	11	10	12
L1 – L2	7	8	8
Thickness[§]			
CM	6.5	7.5	7
MOM	8	8	7.5-8.5
L1	3.5	4	4
L2	3	5.5	7[¶]

CM, cytoplasmic membrane; MOM, mycobacterial outer membrane.
†L1, L2: periplasmic layers assigned to the peptidoglycan-arabinogalactan network.
‡Average values and ranges determined from images.
§Width at half height from averaged profiles.
¶Including variations by subdomains.

5.3 CET of MspA reconstituted into lipid vesicles

Part of this thesis was to evaluate methodical requirements for the identification and localization of MspA *in situ*. In the previous chapter I addressed the problems coming along with cellular samples and their preparation, e.g. the thickness and the compression artifacts introduced by cryo-sectioning to thin cells for CET (cf. Ch. 5.1). Further difficulties arise from the low signal-to-noise ratio and low contrast of proteins located in lipid membranes and the unfavorable focus conditions and variations in projections of tilted specimens. To cope with these difficulties when working with intact cells, there is need to develop a technical strategy. For this purpose, purified MspA was reconstituted into lipid vesicles that served as a model system for the development of a data acquisition-scheme for the analysis of membrane proteins in their natural environment.

5.3.1 Reconstitution of MspA

Several attempts were needed to establish a reproducible insertion of MspA into the membrane of lipid vesicles. Unfortunately, the phospholipids DMPC and DPPC that are widely used in reconstitution experiments of membrane proteins ((MirAfzali et al., 2005; Parmar et al., 1999); Tab. 15) proved to be unsuitable. None of the experimental conditions, listed in Table 15, resulted in reconstitution of MspA, the membranes of all vesicles were ‘empty’. Only the approach with DiphPC, a C16-phospholipid harboring four methyl-groups in each acyl chain, was promising, since it already allowed insertion of MspA in planar lipid membranes used for conductivity measurements (cf. Ch. 5.4). The dialysis method usually yielded vesicles with a wide size distribution. The majority of the vesicles was larger than 1 μm, and was not suited for CET. DiphPC vesicles were prepared by extrusion through a polycarbonate membrane filter having a pore size of 100 nm. Purified MspA, existing as micelles together with the detergent octyl-POE, was added to the vesicle preparation and the whole mixture was incubated with BioBeads® over night at 37° C to remove the detergent and establish the reconstitution. Analysis of the samples by cryo-TEM showed that approximately 25 % of the vesicles contained more than 10 inserted MspA molecules. These preparations were used for further analysis by CET.

Table 15: Lipids and preparation methods for the reconstitution of MspA.

Lipid	Method of vesicle formation	Vesicle diameter	Method of reconstitution	Formation of proteovesicles
1,2-dimyristoyl-sn-glycero-3-phosphocholine (DMPC; PC(14:0/14:0)) TT: +23° C	dialysis¶	50 nm – > 2000 nm§	dialysis*	no
			BioBeads®	no
1,2-dipalmitoyl-sn-glycero-3-phosphocholine (DPPC; PC(16:0/16:0)) TT: +41° C	dialysis¶	no vesicles	dialysis*	no
	extrusion‡	100 nm – 200 nm†	BioBeads®	no
1,2-diphytanoyl-sn-glycero-3-phosphocholine (DiphPC; PC(16:0 4ME/16:0 4ME)) No gel to liquid crystalline phase transition from -120° C to +120° C (Lindsey et al., 1979)	extrusion‡	50 nm – 100 nm†	BioBeads®	yes

TT: transition temperature

¶the lipid was dissolved in detergent containing buffer (0.5 % octyl-POE) and dialysis was performed at 37° C against a constant flow of buffer

*either lipid/detergent-micelles were mixed with protein/detergent-micelles or preformed lipid vesicles were mixed with protein/detergent-micelles before dialysis

§large size distribution

‡Avanti Polar Lipids® mini extruder

†depending on the pore size of the used polycarbonate membrane filter

5.3.2 Extended exposure-scheme for CTF-correction of tilted projections

The detection and reliable interpretation of small structural details in CET is limited by the microscope's contrast transfer function (CTF; cf. Ch. 2.2). To exploit the information contained in EM projections and to achieve higher resolution in tomograms, it is critical to determine the CTF and to correct for its phase inversions. However, the extremely low signal-to-noise ratio (SNR) and the focus gradient in the projections of tilted specimens are challenges for the determination and correction of the CTF. To avoid radiation damage of the structure of interest it is not appropriate to increase the electron dose for imaging and to raise the SNR in the corresponding projections. The standard ‘low-dose’ acquisition scheme consists of the steps ‘tracking’, ‘autofocus’ and ‘exposure’ (Dierksen et al., 1992; Dierksen et al., 1995; Koster et al., 1997; Koster et al., 1989), where ‘tracking’ and ‘autofocus’ are done on an area located along the tilt axis, but displaced only by a small distance from the desired exposure area. Our idea was to extend this scheme by recording two additional high-dose images, one taken at the area used for ‘tracking’ and ‘autofocus’ and the second at the other side of the exposure area along the tilt axis. For every tilt angle, the scheme was paused after the ‘low-dose’ routine, and the beam was moved to the two areas, referred to as *f1* and *f2* via a beam shift. Two images with doses ranging from 20 to 30 $e^-/Å^2$ (per image) were recorded. This ‘manual’ approach seemed to be tedious and time consuming, but unfortunately no reliable software for automation of the procedure was available. After all, the extended procedure requires approximately one minute per tilt angle in addition. The SNR of the image pairs was high enough to determine the defoci and to correct the CTF of every single image of the whole tilt-series. An overview of the extended exposure scheme is shown in Figure 25.

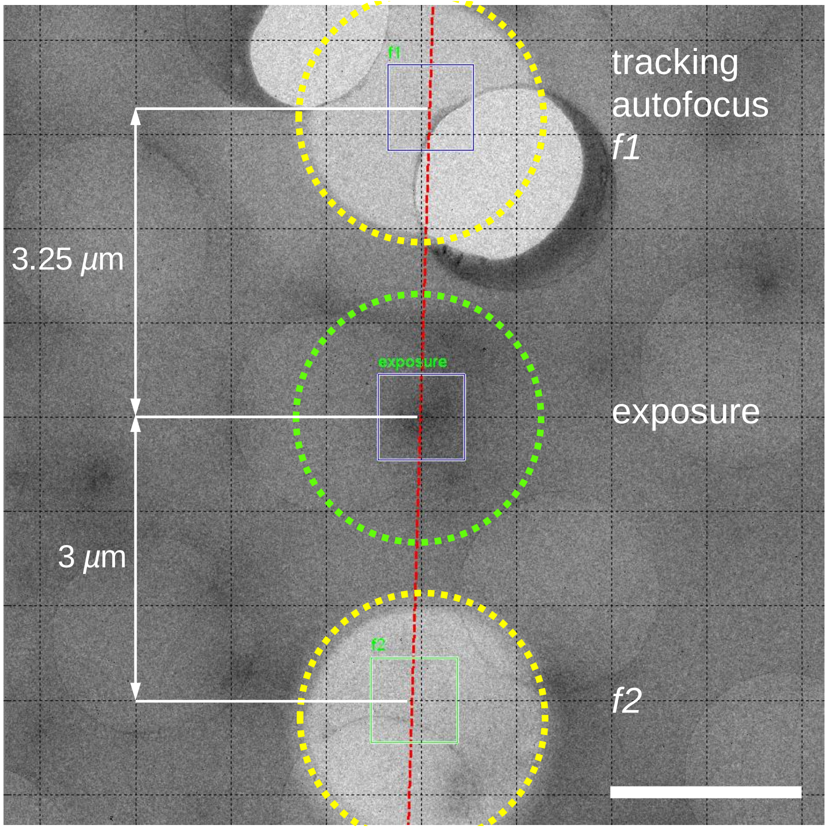

Figure 25: Image illustrating the extended exposure-scheme for subsequent CTF correction of tilted projections. The holey carbon film is covered with vitreous ice and contains MspA that was reconstituted into lipid vesicles. The red dotted line depicts the tilt-axis. *f1* and *f2* are regions where the high-dose images were recorded. *f1* was also used for ‘tracking’ and ‘autofocus’. The areas appear brighter (*yellow circles*) because the ice was ‘evaporated’ with the electron beam to enhance the SNR. Squares indicate the field of view of the CCD camera. (Scale bar: 2 µm.)

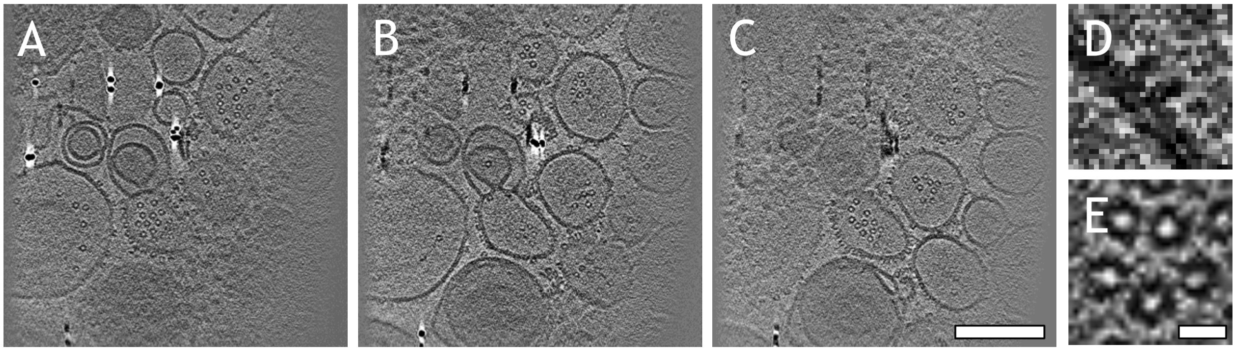

Figure 26: A-C. x-y-slices from a reconstructed volume of lipid vesicles containing MspA in the membrane. The slices are 1.7 nm thick and have a relative distance of 12.6 nm to each other. Black dots in image (*A*) represent gold beads (ø 10 nm) used for alignment of the projections. (Scale bar: 100 nm.) **D. and E.** Typical side- (*D*), and top-view (*E*) of MspA embedded in a lipid membrane as obtained by CET. The membrane in (*D*) is resolved as a bilayer. *E* shows several MspA molecules in top view. (Scale bar: 10 nm.)

5.3.3 CTF determination and correction in tomograms of reconstituted MspA

A series of tomograms of MspA containing proteovesicles were recorded with the extended acquisition procedure. Due to the limited amount of time, only one was further processed with regard to correction of the CTF within the framework of this thesis. Figure 26 represents a typical 3D reconstruction of lipid vesicles with MspA reconstituted in the membranes. Ideally, several hundred protein molecules could be imaged in a single tomogram.

The mean defocus values and the astigmatism for *f1* and *f2* were determined at each tilt angle as described in chapter 4.12.1 (Fernandez et al., 1997; Mindell and Grigorieff, 2003). The tile size for periodogram averaging was 512^2 pixels with an overlap of 50%, fitting of the CTF was done with a defocus increment of 100 nm.

Figure 27 shows images from *f1* and *f2* and the respective power spectra at a tilt angle of 0° (Fig. 27 A) and of 57° (Fig. 27 B). Red circles indicate the zeros of the fitted CTFs. The high SNR of images from *f1* and *f2* allowed detection of at least three Thon rings for all tilt angles. Our CTF-fitting routine allows adjustment to astigmatism, what is indicated by the oval appearance of the rings (Fig. 27). Evaluation of the data showed that the long axis of the ‘astigmatic rings’ ($\Delta z1$) is aligned with the tilt axis and that the Thon rings appear blurry in this direction. Astigmatism was not observed on an averaged power spectrum derived from the exposure position. Instead of misalignment of the optical system (the microscope was carefully aligned before data acquisition with respect to astigmatism) it is more likely that due to the relatively long exposure time (~ 1 sec) at *f1* and *f2*, vibrations transmitted via the mechanical coupling of the sample holder cause drift in the images. Blurring of the Thon rings along one axis is then misperceived as astigmatism by the fitting routine. Therefore, calculation of the defocus values was done based on the course of the power spectrum along the short axis $\Delta z2$. Figure 28 shows the course of the calculated defocus values from *f1* (*black lines*) and *f2* (*red lines*). The mean defocus Δz_{exp} of the exposure position (*blue lines*) is interpolated by:

$$\Delta z_{exp} = \frac{(\Delta z_{f1} \cdot \Delta f1 + \Delta z_{f2} \cdot \Delta f2)}{(\Delta f1 + \Delta f2)}$$

Δz_{f1} and Δz_{f2} are the mean defocus values from *f1* and *f2*; $\Delta f1$ and $\Delta f2$ are the distances of *f1* and *f2* from the exposure position.

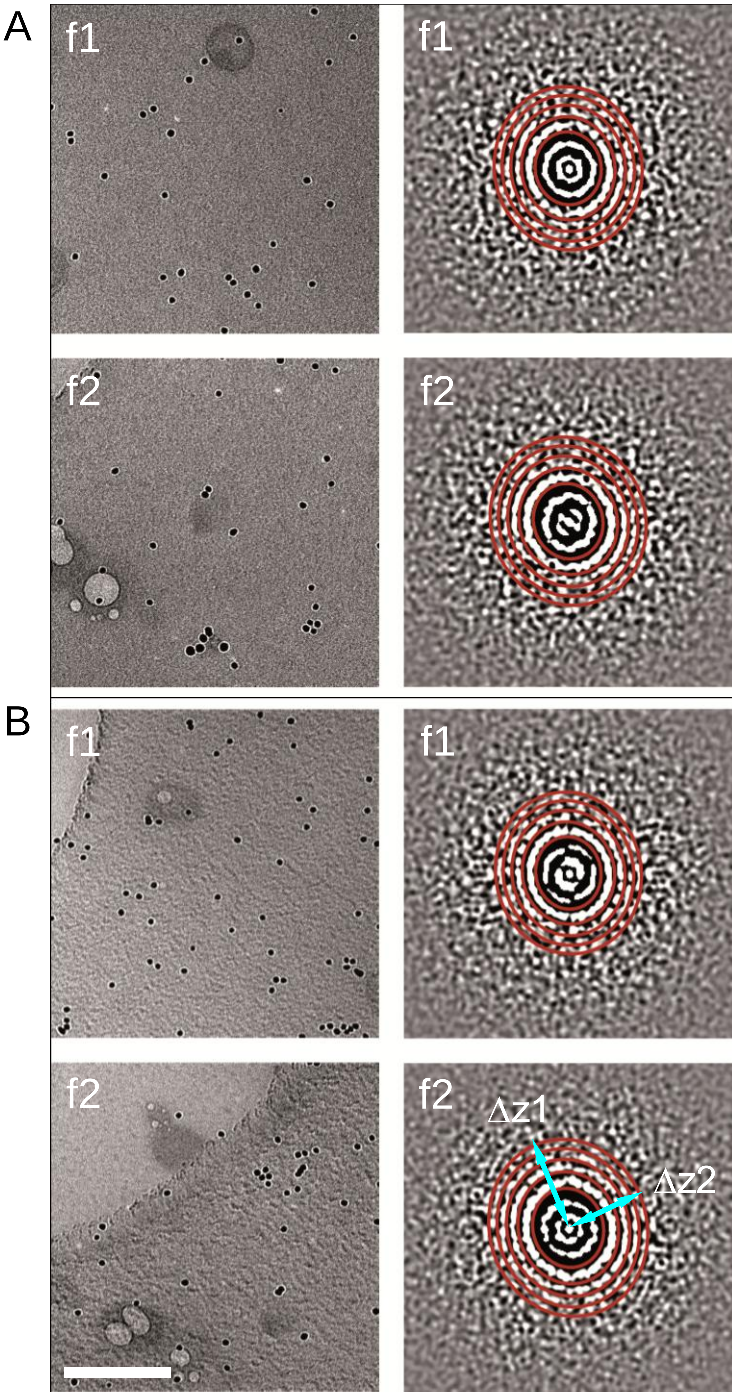

Figure 27: High-dose images of the positions *f1* and *f2* and the respective power spectra as used for determining the defocus values. A. 0° projection. **B.** Projection at a tilt angle of 57°. Red circles indicate the zeros of the fitted CTFs. They appear slightly oval due to drift of the sample in direction of the tilt axis. Δz1: long axis of the astigmatism. Δz2: short axis of the astigmatism. (Scale bar: 150 nm.)

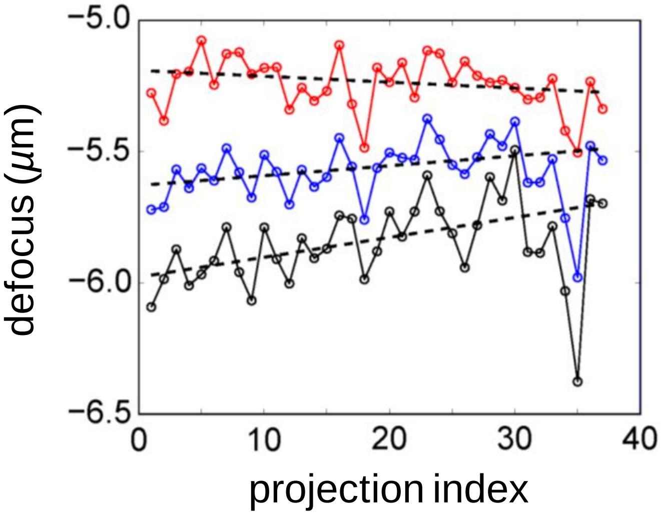

Figure 28: Course of the calculated defocus values for *f1* (*black lines*), *f2* (*red lines*) and the interpolated values at the exposure position (*blue lines*). The nominal defocus in the microscope was set to – 5 μm.

In this experiment *f2* was used for 'tracking' and 'autofocus'. The nominal defocus at the microscope was set to – 5 μm. The *red line* in Figure 28 depicts the measured values for *f2*. The average deviation is less than -300 nm from the nominal setting, which is the expected accuracy of the autofocus of the microscope. The values of *f1* (Fig. 28, *black line*) differ by ~ -600 nm on average, what indicates a slightly tilted orientation of the sample along the tilt axis. For the exposure area (2048^2 pixels), at the given pixel size of 0.21 nm and a distance of 9.5 μm between *f1* and *f2*, this results in a deviation of the z-height of approximately ± 50 nm along the tilt axis in both directions from the center pixel. This value is less than the increment used for fitting the CTF (100 nm, see above), and we treated the exposure area as being flat along the tilt axis for the subsequent CTF correction. The single defocus values show a similar course for *f1* and *f2*, indicating the mechanical imprecision of the sample holder.

For the CTF correction, the defocus value is calculated for every pixel of the exposure area via the tilt angle ψ and its distance Δx from the tilt axis (parallel to the y-axis):

$$\Delta z_{xy} = \Delta z_{exp} + \Delta x \cdot \tan(\psi)$$

Δz_{xy} is the defocus of the pixel *xy*.

Images were corrected using the tile-by-tile approach described in chapter 4.12.1. The corrected tiles extended over 32^2 pixels, while the FFTs were computed over 256^2 pixels. At a tilt angle of 60° and the pixel size of 0.21 nm the defocus variation across a tile of size 256^2 is ~90 nm.

5.3.4 Sub-tomogram averaging reveals the effects of CTF- and MTF-correction and shows the situation of MspA in a lipid membrane

A total of 249 sub-tomograms (64^3 voxels each), containing individual porins embedded in the membrane of lipid vesicles were reconstructed with a 2-fold binning (0.42 nm voxel size) from one tomographic recording. Sub-volumes containing MspA which was inserted outside-in (due to fusion of vesicles after reconstitution) were excluded to avoid ‘smearing’ of the membrane because of the inverted curvature, leaving 191 particles for further processing. To assess the effects of the CTF and MTF correction, two individual datasets were created: one from the original projections and one from the projections corrected for the effects of the CTF and MTF. The subsequent alignment procedure was identical for the two datasets. The electron density map of the crystal structure of MspA (Faller et al., 2004) was resampled to a voxel size of 0.42 nm and used as a starting reference for the alignment of sub-tomograms. An appropriately shaped missing wedge was applied to the Fourier transform of the rotated references in each alignment before cross-correlation with each particle. The aligned sub-tomograms were averaged and eightfold symmetrized before using it as a reference for the next iteration.

The Fourier Shell Correlation between the averaged tomographic maps and the electron density map obtained from the atomic structure (Faller et al., 2004) reveals a major improvement upon CTF and MTF correction, with the recovery of a region of former negative correlation (Fig. 29 *A*). The nominal resolution applying the correlation criterion by Frank (1996) jumped from 29.5 Å (*black line*) to 21.3 Å (*red line*). Sampling of the structure of MspA can be assumed to be almost isotropic, the orientations of the protein cover nearly the entire spectra of angular orientation (Fig. 29 *B*). An improvement in resolution can also be visually detected by comparing the two maps in Figures 30 and 31. The appearance of the protein changes considerably. While the effect is little in the rim domain of MspA, the corrections are most striking in the region spanning the membrane, the stem and base of the protein (the descriptions of the domains are according to Fig. 5 *B*). In both averages, the density of the protein at the transmembrane region is set apart from the surrounding lipid environment. In the uncorrected average the base seems to be 'disconnected' from the stem domain of the protein (Fig. 31 *A*). No structural details can be resolved in the eyelet of MspA and no symmetry is detectable in the autocorrelation or in the contour plot. The membrane appears as a thick single layer without any substructure. In the CTF and MTF corrected map this changes drastically (Fig. 31 *B*). The base is connected to the stem of MspA and a 'waistline' is visible between the two domains. Base and stem show up in more detail and the pore in the base is clearly resolved. Autocorrelation, as well as the contour plot, explicitly depict the eightfold symmetry of the protein. The membrane is resolved as a bilayer.

Rigid body docking of the x-ray model of MspA into the CTF and MTF corrected EM density map evaluates the consistence of both structures (Fig. 32). The density shows good agreement with the overall dimensions of the atomic structure of the porin. Only the upper region of the rim appears slightly smeared out. The base of the protein is flush with the inner surface of membrane and does not extend into the vesicle. ('in' and 'out' are indicated by the membrane curvature).

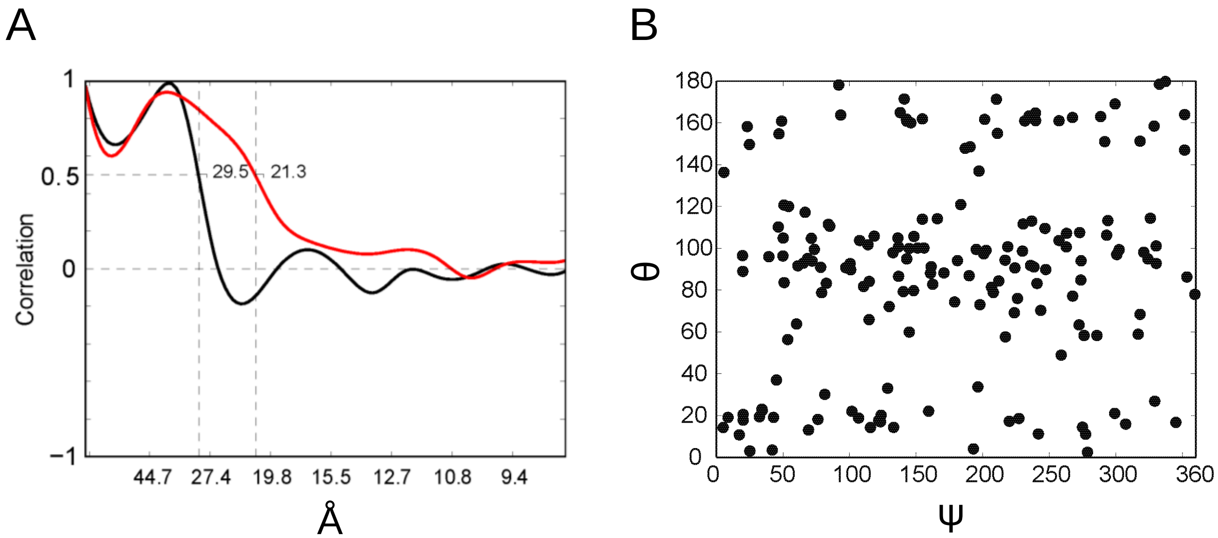

Figure 29: A. Crossresolution between uncorrected/ corrected averages with an appropriately scaled and aligned electron density map obtained from the atomic model of MspA (Faller et al., 2004). A Fourier Shell Correlation (FSC) value of 0.5 was chosen as criterion for the resolution (Frank, 1996). The resolutions are: 29.5 Å for the uncorrected average (*black line*), and 21.3 Å for the CTF and MTF-corrected average (*red line*). **B. Plot of the Eulerian angles Theta and Psi against each other.** Individual MspA particles show a sufficient coverage of the entire spectra of angular orientation.

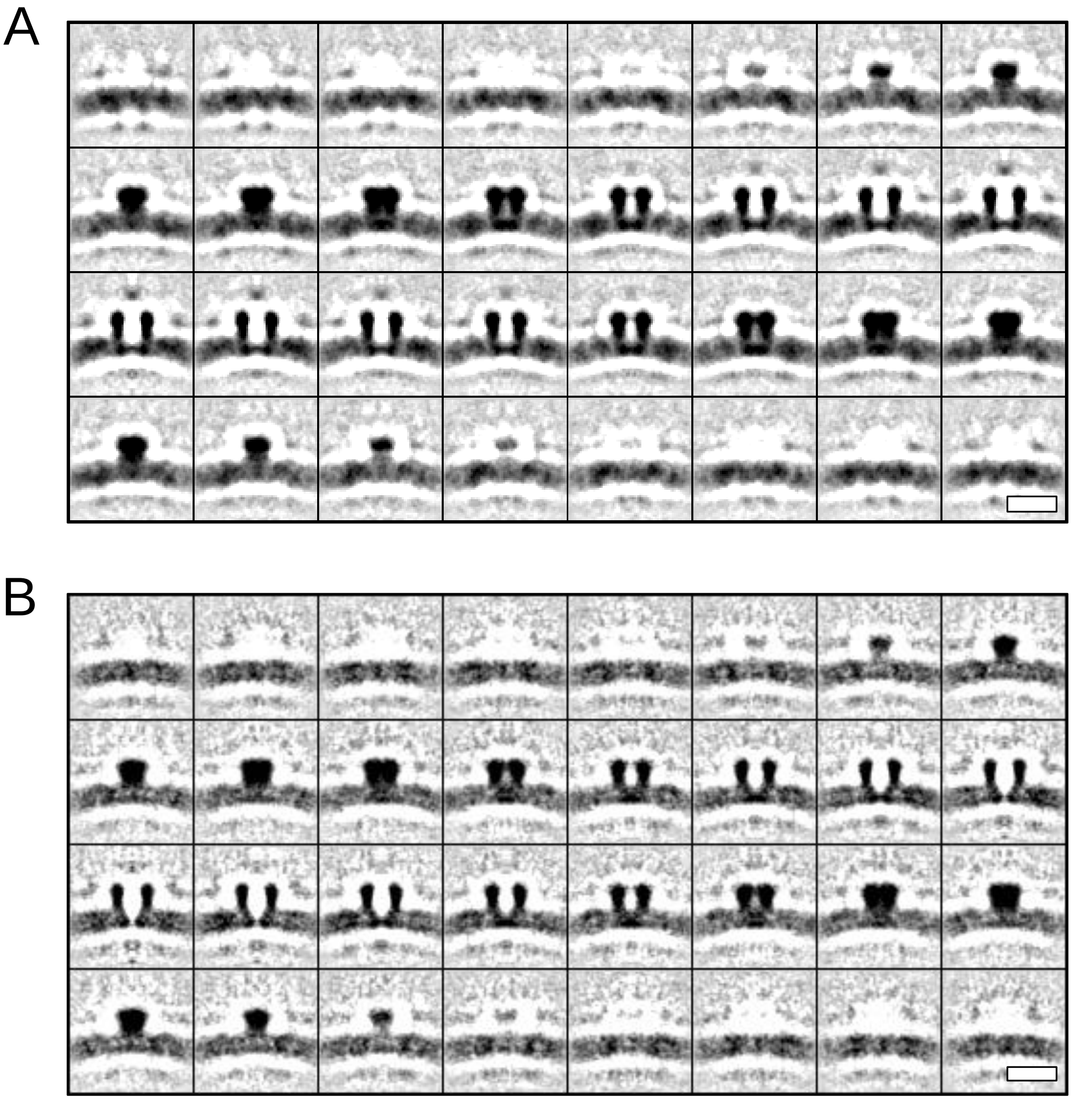

Figure 30: Gallery representation of the density maps of averages of membrane-embedded MspA . The slices have a thickness of 0.42 nm. **A.** Uncorrected map. **B.** CTF and MTF corrected map. The improvement in resolution is clearly visible for the protein and the membrane, which appears as a bilayer upon correction. (Scale bar: 10 nm.)

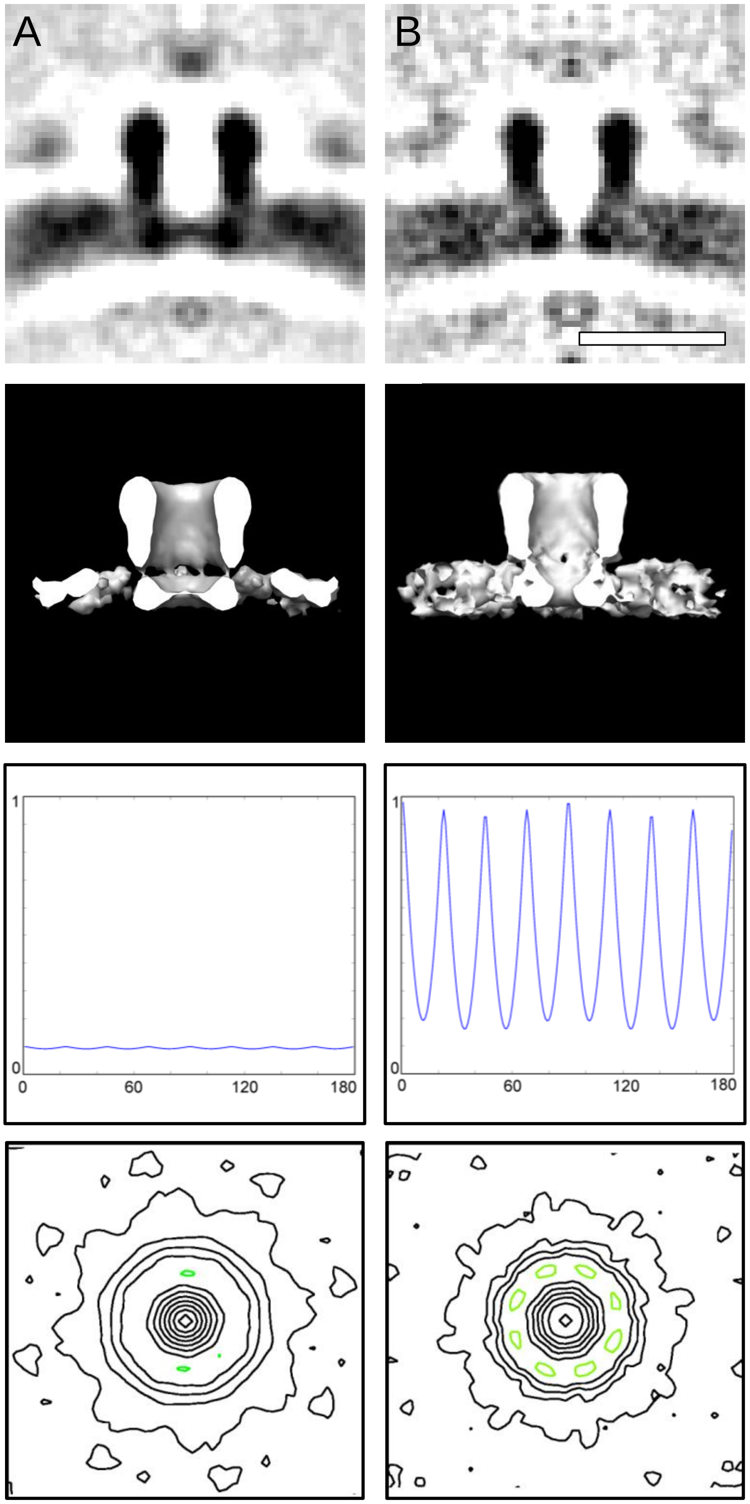

Figure 31: Representations of the averages of membrane embedded MspA showing the improvement in resolution upon correction of the CTF and MTF. A. Uncorrected. **B.** CTF and MTF corrected. Top down: - Central slices from the density maps. - Isosurface representation of the averages, clipped at the central slice. – Autocorrelation plot of a 4.2 nm thick horizontal slice around the of center of the density map . - Horizontal contour plots at half height of the volumes. (Scale bar: 10 nm.)

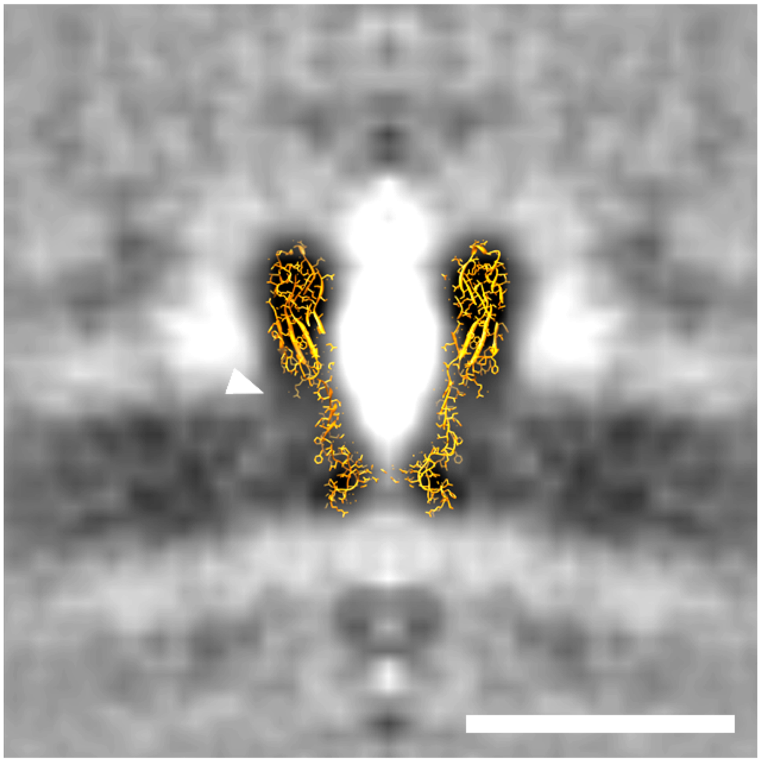

Figure 32: Rigid body docking of the x-ray structure of MspA (Faller et al., 2004) into the EM density map of the CTF and MTF corrected average. Representation of the X-ray structure in *orange*. Docking was performed with Chimera (Goddard et al., 2007). Central slice from the EM map; thickness: 0.42 nm. *White arrowhead*: additional densities at the stem region of the protein. (Scale bar: 10 nm.)

5.4 Biophysical analyses of the ion conductivity of MspA

5.4.1 Construction of the MspA mutants – Strategy

The influence of charged residues inside the pore of MspA on the channel properties and the voltage-depending gating behavior was analyzed recently. In a previous project I could show the impact of amino acids in the ‘eyelet’ of the pore. The negatively charged aspartates D90 and D91 in the wild-type were exchanged with a variety of other amino acids with different properties (charge, ‘dimensions’ of the sidegroup, *etc.*) and the effects on the channel properties were analyzed. We could prove that the selectivity of the pore strongly depends on the charges in the ‘eyelet’ (Hoffmann, 2005). Later, Butler and coworkers studied the feasibility of using MspA for nanopore sequencing of DNA (2008). They constructed, *inter alia*, a mutant which has no charged residues in the constriction zone of the pore. In lipid bilayer experiments these pores remained in an ‘open’ state up to significantly higher transmembrane potentials compared to the wild-type MspA (and thus allowed translocation of single stranded DNA). Butler’s mutants still had charged residues at the entrance of the pore and in the vestibule. Therefore, we were interested in the behavior of a completely ‘neutral’, i.e. uncharged pore. In addition to the amino acids in the constriction zone, D90, D91 and D93, six other amino acids likely influence the charge of the pore; these are: D56, E57, D118, E127, D134 and D139 (Fig. 33). Asparagine (N) was chosen as a ‘neutral’ replacement and via site-directed mutagenesis, using the combined chain reaction (CCR; (Bi and Stambrook, 1997)), the mutant *mspA* D56N E57N D90N D91N D93N D118N E127N D134N D139N was constructed in a stepwise fashion and named N-MspA.

Shortly after Butler, Huff et al. studied the influence of the loop (L6) at the periplasmatic end of MspA on the pore properties by constructing various deletion mutants (2009). He showed that removal of this flexible region also strongly alters the channel behavior. They observed different conductivity values and less gating compared to wild-type MspA. We wanted to analyze the effect on the pore and on the voltage-depending gating in particular, when both features were combined, a pore without net charges inside the channel and a missing periplasmic loop L6 (Fig. 34). Hence, based on N-MspA, a loop L6 deletion mutant was constructed and named N-MspA ΔL6.

The mutant was cloned into pMN016, which contains a *psmyc-mspA* transcriptional fusion (Stephan et al., 2005) and expressed in *M. smegmatis* ML10 (Stephan et al., 2004b). Figure 35 schematically depicts the cloning strategy.

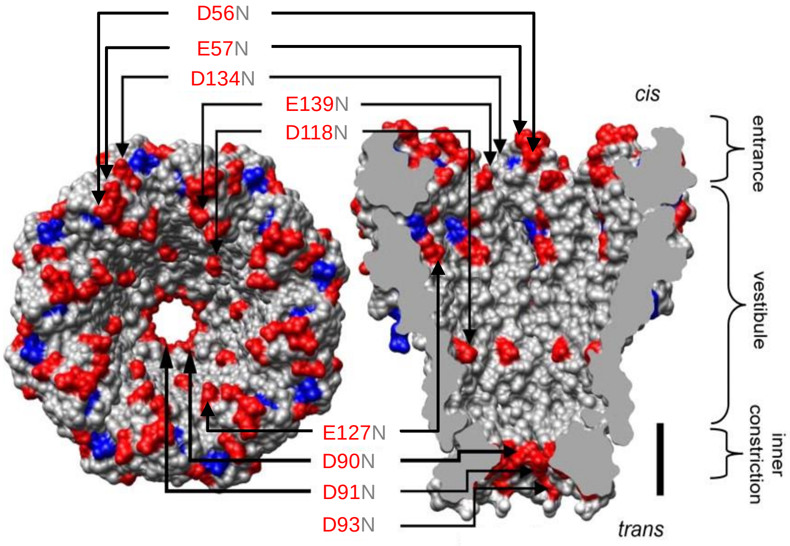

Figure 33: Charge distribution of wild-type MspA (adapted from (Butler et al., 2008)). Aspartate and glutamate residues are colored *red*, and argenine and lysine residues are colored *blue*. Pointmutations are indicated by arrows and labels.

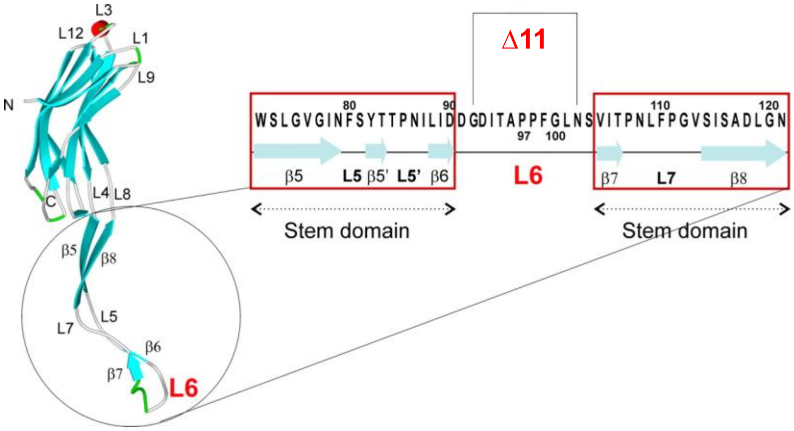

Figure 34: Schematic representation of the deletion of the periplasmic loop 6 of MspA (Huff et al., 2009). The assignment of the secondary structure elements was taken from the crystal structure of MspA (Faller et al., 2004). *Turquoise arrows* represent the β-sheets, *light grey lines* represent the loops and the *red cylinder* represents the L3 helix. The periplasmic loop is marked as L6, and the sequence of loop 6 and the stem domain is shown to the right. Deletion of amino acids 92 – 102 generated the mutant Δ11.

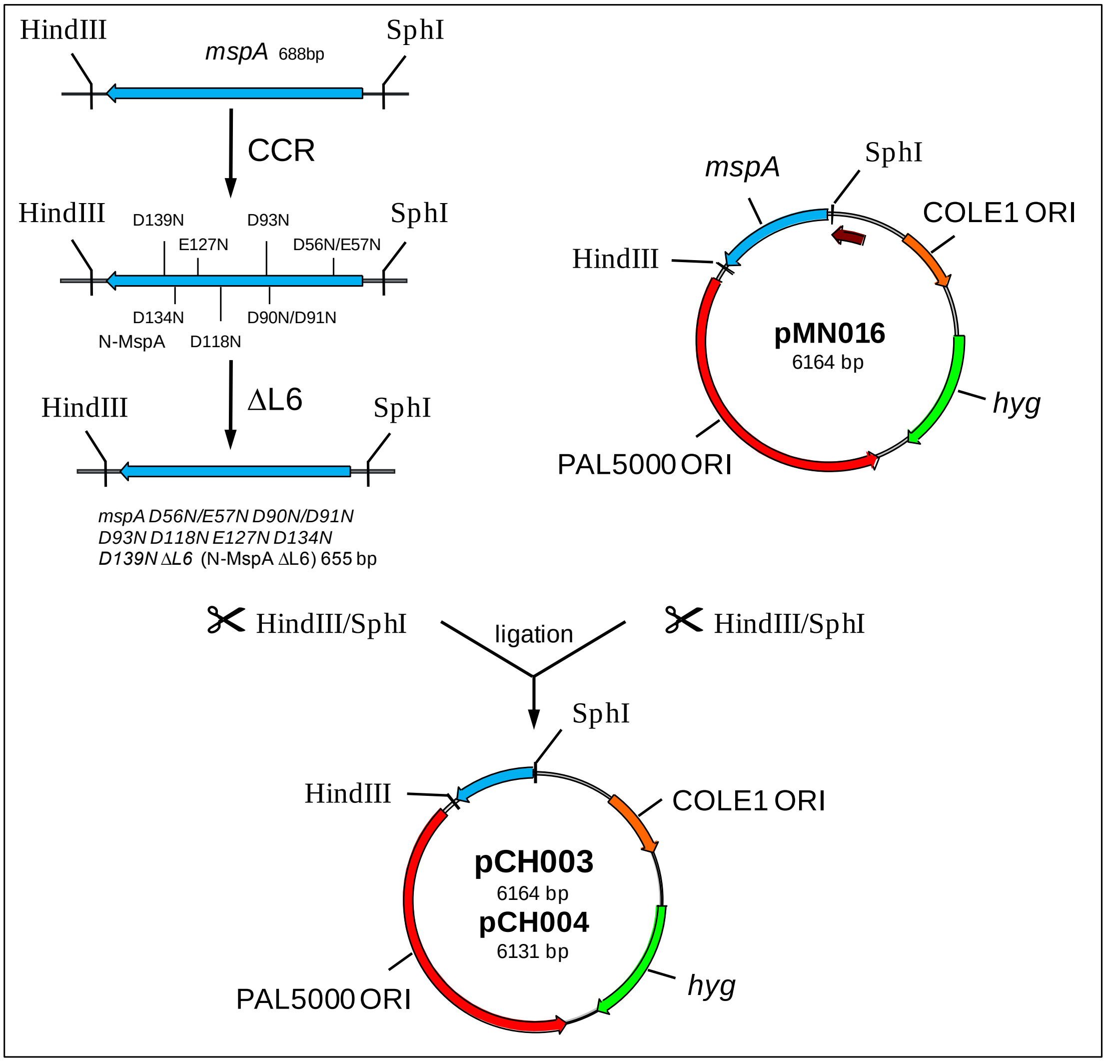

Figure 35: Cloning strategy for the mutants N-MspA and N-MspA ΔL6. Based on wild-type mspA, nine negatively charged amino acids inside the channel were consecutively replaced with aspargine via site directed mutagenesis by CCR, resulting in N-MspA. Based on this mutant the periplasmatic loop L6 was deleted using appropriate mutagenesis primers (Tab. 5). The mutants were cloned into pMN016 resulting in pCH003 (N-MspA) and pCH004 (N-MspA ΔL6). *COLE1 ORI*, *E. coli* origin of replication; *hyg*, hygromycin phosphotransferase; *psmyc*, strong mycobacterial promotor; *PAL5000 ORI*, mycobacterial origin of replication.

5.4.2 Expression of N-MspA and N-MspA ΔL6 in *M. smegmatis* ML10

For expression of the *mspA*-mutant genes, the porin double ‘knockout’-mutant *M. smegmatis* ML10, which lacks the *mspA* and *mspC* genes, was used (Stephan et al., 2004b). To examine whether the mutant was expressed in ML10, the standardized selective extraction procedure was utilized that yields predominantly MspA when whole cells of *M. smegmatis* are heated with 0.5%

ocyl-POE to 100 °C (Heinz et al., 2003b). A whole cell extract of the mutants was separated on a denaturing 12% polyacrylamide gel and stained with Coomassie Blue. No porins were detectable in extracts of *M. smegmatis* ML10 carrying the empty vector pMS2 (Kaps et al., 2001), indicating a very low background expression of *mspB* and *mspD* (Fig. 36, *lane 4*). Expression of wild-type *mspA* in ML10 using the plasmid pMN016 (Fig. 36, *lane 1*) yields MspA levels similar to that in wild-type *M. smegmatis* mc^{2}155 (Stephan et al., 2005). Expression of N-*mspA* was slightly, and of N-*mspA* ΔL6 significantly reduced in comparison with wild-type *mspA* (Fig. 36, *lane 2* and *3*). The results demonstrated that the mutants were expressed in *M. smegmatis* ML10 and were stable during heat extraction. The much lower expression of N-*mspA* ΔL6 indicated the importance of the periplasmic loop for MspA expression and/or insertion in the outer membrane.

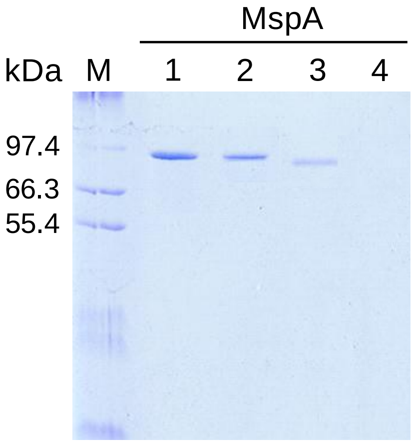

Figure 36: Expression of the mutant N-mspA ΔL6 in the porin mutant M. smegmatis ML10. *Lane M*, protein mass marker (Mark12; Invitrogen); l*ane 1*, wild-type MspA; *lane 2*, N-MspA; *lane 3*, N-MspA ΔL6; *lane 4*, pMS2.

5.4.3 Conductivity measurements of MspA

To gain insights into the biophysical properties of the porin MspA in comparison with the constructed mutants, the proteins were reconstituted in planar lipid bilayers (cf. Ch. 4.10.2). Channel currents were recorded under voltage clamp conditions. Once the seal was obtained, the buffer solution was perfused to remove the remaining vesicles and to stabilize the membrane by avoiding evaporation. The recording of MspA in the lipid bilayer was stable for long periods allowing a thorough investigation of the properties of the porin. In 75 % of the experiments functional MspA was successfully inserted.

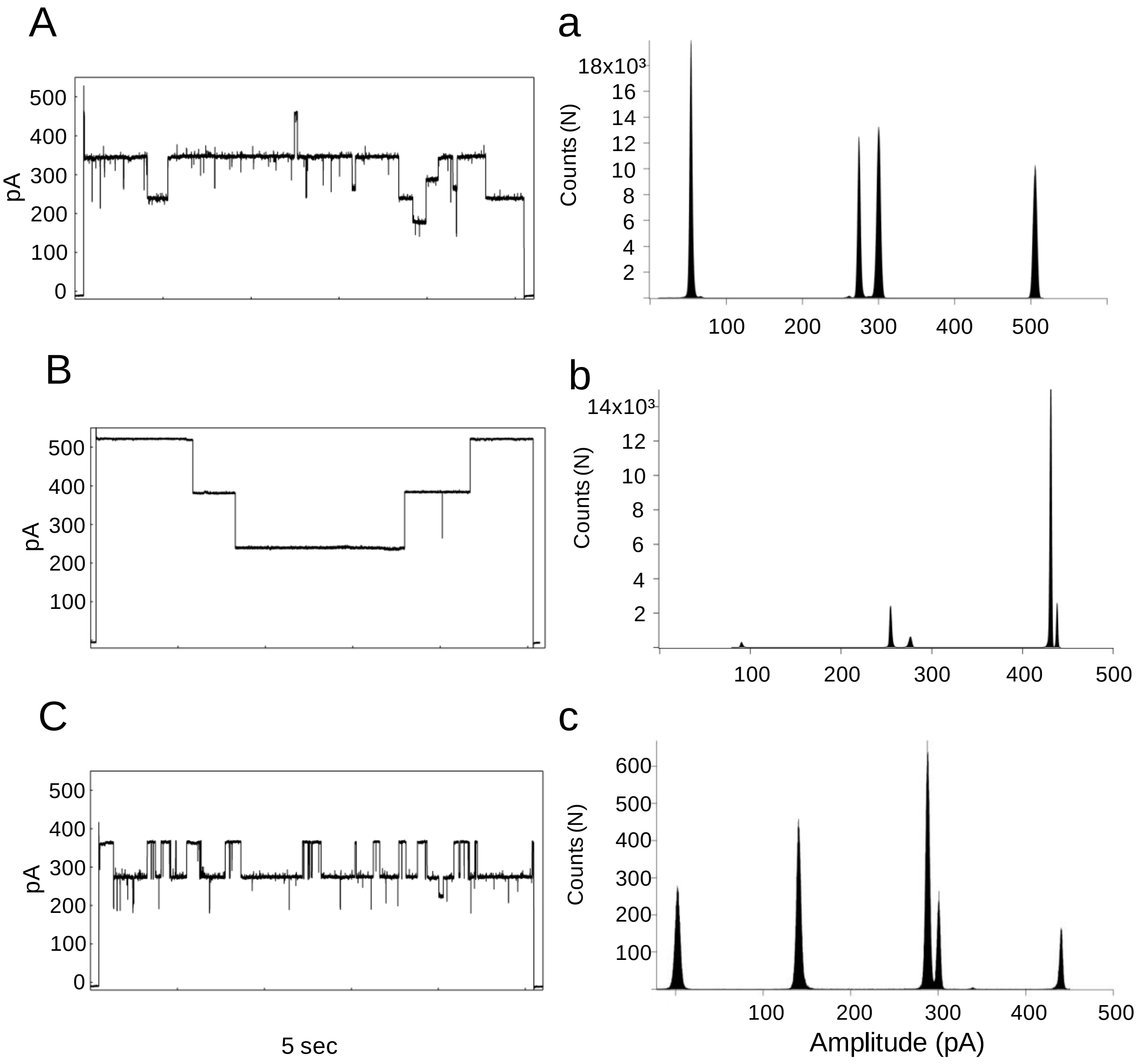

Figure 37: Channel activity of MspA. A. Wild-type, B. N-MspA, C. N-MspA ΔL6. *Left:* Representative current traces of single MspA channels in 1M KCl at a transmembrane potential of + 100 mV. *Right*: Current-amplitude frequency histograms collected from several distinct single-channel measurements. Different conductivity sub-states can be observed for MspA and the mutants.

As shown in Figure 37 we have analyzed the properties of single MspA channels in 1M KCl at pH 7.5. For all recordings, the maximal filtering frequencies and sampling rates were used (filtering frequency 10 kHz; sampling rate of 20 μsec (50 kHz)) to achieve high temporal resolution. The noise level for the current recordings was 2 pA rms using the settings described above.

Figure 37 shows single channel current traces of wild-type MspA, N-MspA and N-MspA ΔL6 recorded at a membrane holding potential of +100 mV (positive potential at the periplasmic side of the pore). Histogram analysis was made to determine the conductance levels (Fig. 37 *a* – *c*). The average single channel conductance was calculated from the slope of the fitted lines in the I/V-curves (Fig. 38). To accommodate the asymmetric behavior of the pores fitting was done separately for the positive and the negative potentials. The determined values are summarized in Table 16. The conductance value for wild-type MspA in 1M KCl is in agreement with other studies using a different experimental setup (Engelhardt et al., 2002; Huff et al., 2009). The data shows that removal of the charges inside has a stronger influence on the pore's conductivity than deletion of the periplasmic loop L6. Different sub-states of conductivity were observed for all three pores (Fig. 37 *a* – *c*). Similar results were also observed in previous investigations of wild-type MspA (Niederweis et al., 1999).

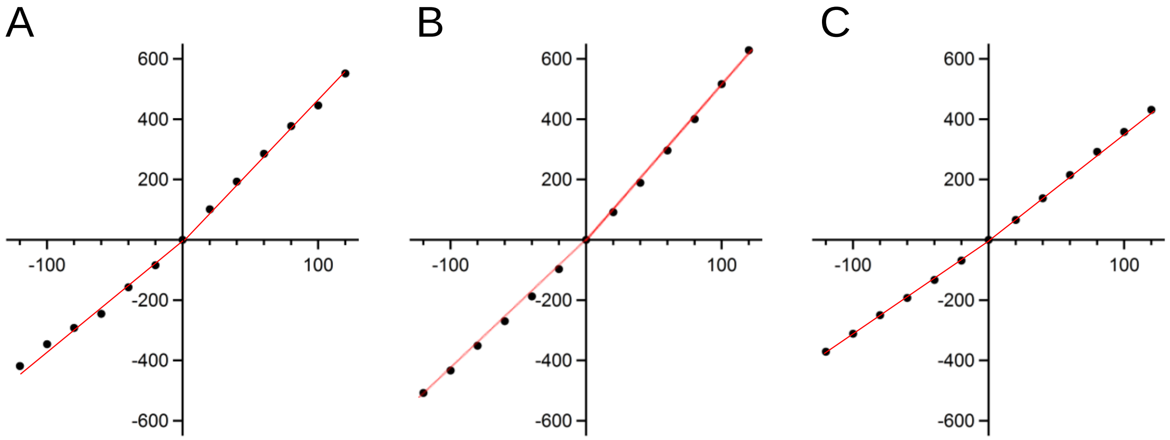

Figure 38: I-V relation of single MspA channels. A. wild-type MspA, **B.** N-MspA, **C.** N-MspA ΔL6. The average single-channel conductance was calculated separately for the sectors from the slope of the fitted lines.

Table 16: Average conductance values of MspA

Pore	Potential	
	+	-
wild-type MspA	4.7 nS	3.8 nS
N-MspA	5.1 nS	4.2 nS
N-MspA ΔL6	3.7 nS	3.0 nS

5.4.4 Gating behavior of MspA

In order to investigate the voltage-dependent gating behavior of MspA and its mutants, potentials from -120 mV to +120 mV were applied and the current of one channel was recorded (10 channels in the case of N-MspA ΔL6) (Fig. 39). As shown previously, the closing behavior of MspA is strongly asymmetric (Engelhardt et al., 2002; Huff et al., 2009). For wild-type MspA (Fig. 39 *A*) no closing of the channel was observed at low voltages independent of the polarity (*red curve*). Beyond a potential of +40 mV gating increased with the voltage, whereas the conductivity remained constant at potentials up to – 60 mV. The situation was significantly different for the ‘charge-free’ mutant N-MspA (Fig. 39 *B*). No asymmetry was observable with reference to the polarity. Gating only occurred at voltages beyond 80 mV. This behavior changed with the loop deletion mutant N-MspA ΔL6 (Fig. 39 *C*). Now, channel gating was observed at potentials of +60 mV and -80 mV, respectively.

To sum up, we could verify the previous results concerning the voltage depending gating observed for wild-type MspA (Engelhardt et al., 2002; Huff et al., 2009). Removal of the charges inside the pore (N-MspA) shifted the onset of gating to higher voltages and apparently eliminated the asymmetry with respect to the field polarity, whereas the additional deletion of the periplasmic loop (N-MspA ΔL6) again led to a slight asymmetric gating. These results give some clues as to the possible mechanisms of voltage dependent closing (see Ch. 6.4)

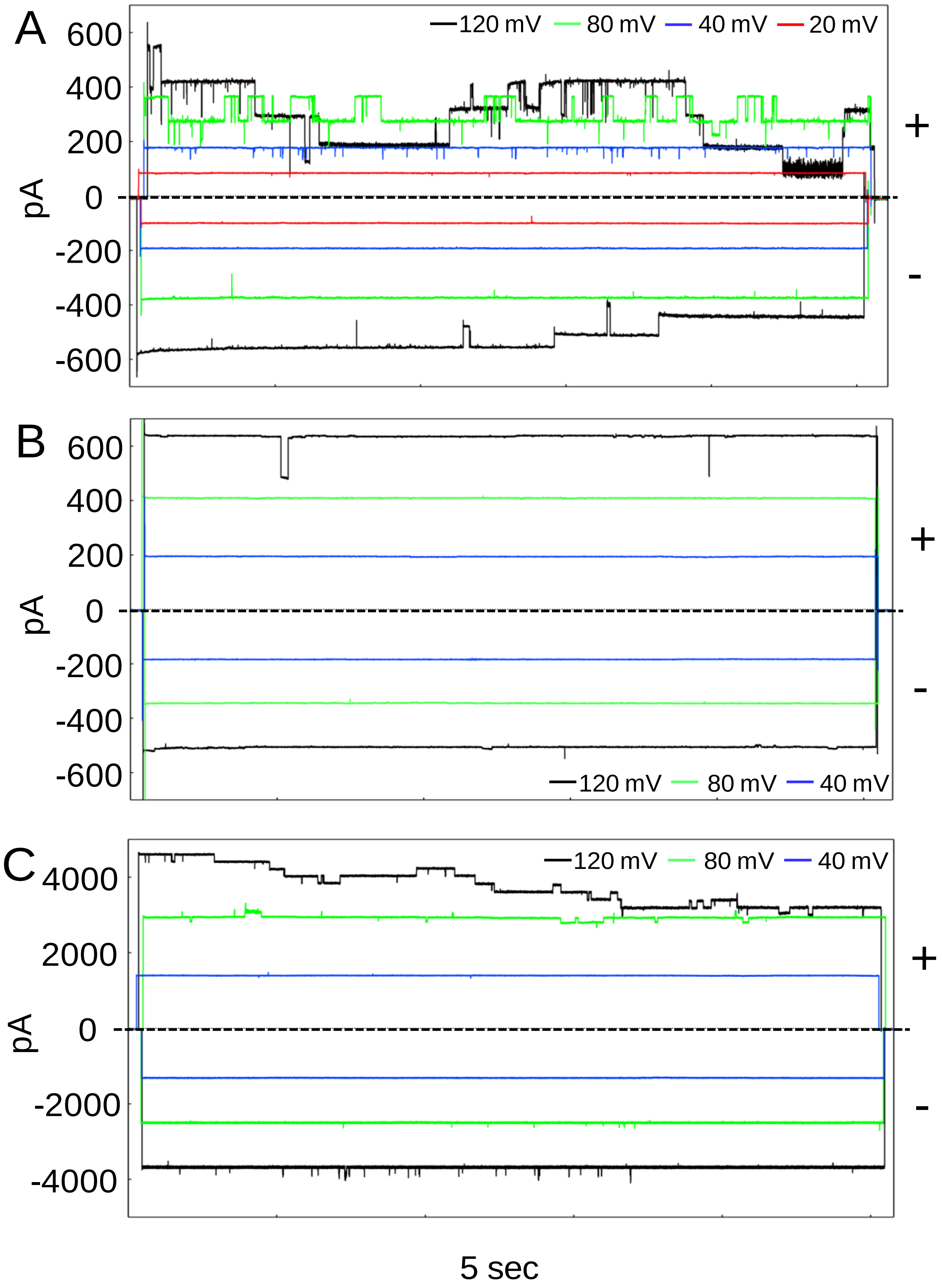

Figure 39: Representative current traces of the voltage gating properties of MspA. A. Wild-type MspA, **B.** N-MspA, **C.** N-MspA ΔL6. Potentials from -120 mV to +120 mV were applied to the membrane when one channel was reconstituted (10 in the measurements of N-MspA ΔL6).

6 Discussion

The results shown in this thesis demonstrate the way how the structure of microbial cell envelopes can be investigated by new strategies in sample preparation, data acquisition in CET and 3D-data analysis to improve the resolution and visualization of molecular structures in tomograms. In the following, I will discuss the major steps involved:

- Adaption of CET imaging parameters and resolution of membranes as bilayer as a prerequisite for the investigation of the cell envelope structure and composition.

- FIB thinning of samples without compression/artifacts for improved visualization of structural detail in tomograms.

- Reliable CTF correction by means of an expanded data acquisition scheme and improvement of resolution of structural detail in tomograms, particularly of proteins embedded in membranes.

Besides the structural investigations, a series of electrophysiological measurements addressed the functionality, i.e. voltage-dependent closing, of the mycobacterial porin MspA embedded in a lipid membrane.

6.1 CET of intact cells and vitreous sections

6.1.1 The outer cell wall layer is the mycobacterial outer membrane

The combination of cryo-electron tomography that preserves the architecture of cells and of vitreous cryo-sections that allows one to identify structures in cross-sections of ultrathin specimens in projection proved suitable for the investigation of mycobacterial cell envelopes. The study revealed the bilayer structure of lipid membranes in tomograms of intact bacteria, and thus opens the way to investigate cell envelopes and their macromolecular constituents by cellular CET in situ. The cryo-electron microscopical investigations in this study provided (i) direct evidence that the outermost layer in *M. smegmatis*, *M. bovis*, and *C. glutamicum* is an outer membrane with a bilayer structure, (ii) the insight that the layer of bound mycolic acids is leaky to amphiphilic molecules octyl β-glucoside once the integrity of the mycobacterial outer membrane has been affected by the detergent, and (iii) direct evidence for a multilayered cell wall organization in mycobacteria. The findings provide the molecular explanation for the existence of outer membrane proteins (Alahari et al., 2007; Faller et al., 2004) and periplasmic proteins, such as PhoA (Wolschendorf et al., 2007) in mycobacteria.

6.1.2 The structure of the mycobacterial outer membrane differs from current models

Numerous models for the mycobacterial cell envelope have been proposed (Barry and Mdluli, 1996; Brennan and Nikaido, 1995; Chatterjee, 1997; Dover et al., 2004; Lee et al., 1996; Nikaido et al., 1993; Rastogi et al., 1991), but electron microscope investigations neither proved nor disproved the suggested architectures. CET and vitreous cryo-sections now confirm the presence of a mycobacterial outer membrane. In addition, the results call into question other aspects of the current models. First, the head group regions show almost identical mass densities in tomograms and cryo-sections, which denotes that the average composition and distribution of head groups do not differ significantly with respect to their masses in either leaflet. By contrast, the asymmetry of the outer membrane of Gram-negative bacteria is clearly visible in cryo-sections (Matias et al., 2003; Zhang et al., 2004) as well as in tomograms of frozen-hydrated intact cells (Fig. 5.4). This result conflicts with the assumption that the inner leaflet of the mycobacterial outer membrane consists exclusively of mycolic acids with identical carbohydrate head groups and that the outer leaflet is a mixture of extractable lipids containing carbohydrates, peptides, and phosphorylated compounds. Second, the outer membrane is thinner than expected. Experiments with ultrathin sections of mycobacteria prepared by freeze substitution showed an electron-transparent zone of 7 – 12 nm that is thought to contain the bound mycolic acids and that is covered by the stained outer layer of ≈ 6 – 11 nm (Mineda et al., 1998; Paul and Beveridge, 1992, 1994; Wang et al., 2000) containing lipids (Etienne et al., 2005; Ortalo-Magne et al., 1996). The theoretical models suggest a hydrocarbon region of ≈ 9 nm with the lipid residues in an extended conformation. Taking into account that the α-chain region of bound mycolic acids is in the gel phase and the remainder, including extractable lipids, is in the fluid phase (Liu et al., 1995), the hydrocarbon region should be thinner. Based on the relative shrinkage of fluid membranes compared with those in the gel phase (Heller et al., 1993), a lower limit of ≈ 7 nm was assessed. However, the outer membrane has a measured total thickness of ≈ 8 nm or less, in perfect agreement with the porin MspA that serves as a molecular ruler. The hydrophobic surface of MspA is only 3.7 nm in height (Faller et al., 2004), and the porin (total length 9.8 nm) is inaccessible to surface labeling over 7 nm from the periplasmic end to the middle of the hydrophilic rim (Mahfoud et al., 2006). These distances correspond to the observed membrane dimensions, including headgroup regions. Moreover, the top part of MspA extends into the aqueous environment, as suggested by electron microscopy of isolated cell walls (Engelhardt et al., 2002).

6.1.3 Modified models of the mycobacterial outer membrane

Significant revisions are required to reconcile the current model of the mycobacterial outer membrane with the results of this study. The apparent symmetry suggests that similar (extractable) lipids are located in both leaflets of the mycobacterial outer membrane, which is in agreement with quantitative determinations (Nikaido et al., 1993). Accordingly, bound mycolic acids might not cover the cells completely. While this likely applies for corynebacteria (Puech et al., 2001), it was proposed to be different for mycobacteria (Nikaido et al., 1993). The smaller membrane thickness poses a more serious problem, unless the conformation of the hydrocarbon region is considerably different from the current view. Hence it is legitimate to look for alternative architectures with a reduced membrane thickness. Unfortunately, cryo-electron microscopy images do not give clues about the conformation of the lipids in the outer membrane, but two theoretical solutions with positional variations of mycolic acids are compatible with the results of this thesis. As mentioned before, mycolic acids consist of up to 90 carbon atoms that form a long branch, called meromycolate, and a shorter α-branch (Fig. 3 *A*). The meromycolate contains cyclopropane rings, substitutions, and/or double bonds that are characteristic for mycobacteria (Barry et al., 1998). If the meromycolate had an elongated conformation (Hong and Hopfinger, 2004; Nikaido et al., 1993), it would span the complete hydrophobic matrix, leaving space for free lipids to intercalate (Fig. 40 *A*), Interestingly, for corynebacteria, it was already discussed that the inner leaflet contains soluble lipids (Bayan et al., 2003; Puech et al., 2001), whereas the bound mycolates rather serve to “tether” the outer membrane in an arrangement similar to that in Figure 40 *A* (Dover et al., 2004). Or the meromycolates have a folded conformation and form the inner layer of the mycobacterial outer membrane together with extractable lipids (Fig. 40 *B*), what is supported by monolayer experiments and simulation data at moderate temperature and low lateral membrane pressure (Villeneuve et al., 2005; Villeneuve et al., 2007). The kinks are at positions of *cis* double bonds or *trans* cyclopropane rings. This conformation might be stabilized by keto or methoxy groups that were recently proposed to interact with lipid head groups (Zuber et al., 2008). The tentative models in Figure 40 are in accordance with other experimental findings. (i) The outer membrane possesses a hydrophobic interphase that would account for a fracture plane observed in freeze fracture experiments. (ii) Some extractable lipids are more intimately bound to mycolic acids than others. They might be located in the inner leaflet of the outer membrane (Etienne et al., 2005; Ortalo-Magne et al., 1996). (iii) They are consistent with the tight packing of mycolic acids and the results of Liu *et al*. (Liu et al., 1995), who observed that spin-labeled fatty acids partitioned into the region of extractable lipids in isolated cell walls. (iv). The models are compatible with recent data obtained by electron microscopy of *M. smegmatis* cells, postfixed with osmium tetroxide (OsO_4) (Zuber et al., 2008), which is considered to label predominantly lipids (White et al., 1976). After treatment of the cells with OsO_4 the bilayer structure of the mycobacterial outer membrane disappears, whereas the region of the periplasm below the membrane remains electron- transparent and is not altered. Assuming a possible conformation with the α-chain and the unpaired region of the meromycolate being located “outside” the membrane, as discussed previously (Hoffmann et al., 2008) these would have been stained by the OsO_4, too, and as a consequence, led to an increased thickness of the electron-dense layer, which is not the case. However, direct experimental evidence for the conformation of mycolic acids *in situ* does not exist.

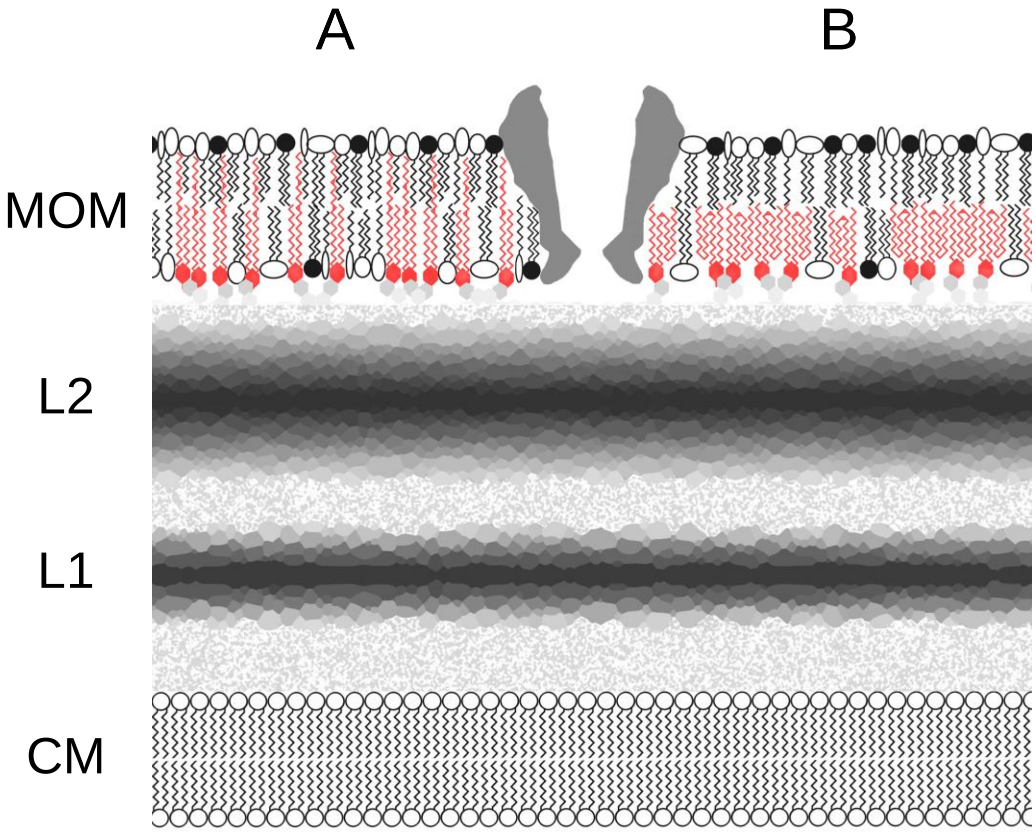

Figure 40: Theoretical models of the mycobacterial outer membrane exhibiting reduced thickness, consistent with the cryo-microscopical and -tomographical data. Mycolic acids are drawn in red and inserted either in the elongated conformation (*A*) or the folded conformation (*B*). The covalent bonding of mycolic acids to the arabinogalactan polymer is indicated. The symbols of lipid head-groups indicate that different free lipids could occur in both leaflets of the outer membrane. The profiles of the pore proteins drawn in gray correspond to MspA of *M. smegmatis* (length: 9.8 nm). **A.** The meromycolate of bound mycolic acids spans the hydrocarbon region. **B.** Mycolic acids in the folded conformation together with extractable lipids form the inner layer of the mycobacterial outer membrane. There is no direct experimental evidence for any of the suggested conformations of the mycolic acids *in situ*. The dimensions of the membranes and the periplasmic layers are in accordance with the cryo-microscopical and –tomographical data. CM, cytoplasmic membrane (membrane proteins are not shown); L1 and L2, periplasmic layers of still unknown identity (L2 represents at least part of the peptidoglycan-arabinogalactan polymer); MOM, mycobacterial outer membrane.

All outer membrane architectures discussed imply an indispensable role of the mycolic acids for the integrity and stability of the mycobacterial outer membrane. This implication is in agreement with the absence of the bilayer in the *C. glutamicum* mutant investigated here and the apparent loss of the mycobacterial outer membrane in species with impaired mycolate synthesis (Wang et al., 2000). These considerations suggest that it is essential to gain insight into the conformation of the hydrocarbon region (e.g., by means of molecular dynamics simulations of a complete membrane bilayer) and to localize the mycolic acids more precisely to gain a comprehensive view of the mycobacterial outer membrane.

The investigation of frozen-hydrated preparations rendered the periplasmic layers visible, as well as domains that likely represent the complex organization of the peptidoglycan-arabinogalactan-mycolate polymer. The discernible structures imply a more differentiated architecture than that derived from chemically fixed and stained material. Once it is possible to assign the layers L1 and L2 and their domains to known constituents of the cell wall, we should be able to establish a more comprehensive model of the cell wall architecture. Such a model will also provide a better basis to understand the peptidoglycan and arabinogalactan structure in mycobacteria (Crick et al., 2001; Dmitriev et al., 2000). In conclusion, proof of the existence of a mycobacterial outer membrane and, by inference, of a periplasmic space in mycobacteria, the structural features of the membrane and the confirmation that extractable lipids play an important role for the membrane properties will have an impact on the design and interpretation of experiments aimed at elucidating the translocation pathways for nutrients, lipids, proteins, and antimycobacterial drugs across the cell envelope.

6.2 FIB-micromachining of *M. smegmatis* cells for CET

A major challenge in cellular cryo-electron tomography is to push the resolution to a range where macromolecular structures can be clearly identified within the cellular context. Thus, sample preparation assuring maximal specimen preservation is a prerequisite. Especially for specimens exceeding a thickness of more than 1 μm efforts are required to thin the samples prior to imaging without affecting the biological structures. In the recent years, cryo-ultramicrotomy became the method of choice for obtaining thin frozen hydrated samples of large cells or tissues. Unfortunately, cryo-sectioning is afflicted with artifacts which apparently cannot be avoided (cf. Ch. 3.1; (Al-Amoudi et al., 2005)). Alternative approaches are necessary to produce undistorted thin cellular samples for CET. The use of a focused ion beam (FIB) seems to be a significant improvement over ‘conventional’ methods (Marko et al., 2007), especially due to the lack of mechanical deformation. Although the results from Marko and his coworkers were very promising, no other report describes the successful implementation of a FIB into a cryo-sample ‘preparation-pipeline’, which might reflect the technical challenges. The cryogenic conditions need to be maintained during the complete sample-transfer and the milling procedure, while the contamination caused by ‘frost’ has to be kept at a minimum. Accompanying this work, a cryo-sample stage for the FIB as well as a transfer system was designed and built in our department (Rigort et al., 2010). Since the cell envelope structure of *M. smegmatis* suffered from compression with cryosectioning (cf. Ch. 5.1.3; (Matias et al., 2003)) the application of the FIB milling approach was of interest. Two different milling geometries were considered: (i) a parallel approach, involving cutting the frozen grid into halves due to its ‘topology’ (Fig. 24 *C* and *D*), and (ii) milling at shallow ion-beam incidence angles, producing wedge-shaped areas (Fig. 24 *B*). The major advantage of the parallel approach is that the sample-thickness is constant over the whole area of interest, and loss of information in the z-dimension is limited. However, although it was possible to cut the grids into halves under cryogenic conditions and to mill reasonably thin (< 500 nm) parallel areas into the ice at the cutting edges, all attempts to preserve these areas during the transfer into the TEM failed. Due to the missing support of the grid bar at one side of the ‘mesh’ the fragile carbon film on the grid is weakened further and can not withstand the mechanical deteriorations while mounting the grid into the cartridge for the TEM. One solution to this problem could be a combined FIB/TEM-cartridge which allows final grid mounting before milling. In addition, milling could be done stepwise to avoid an abrupt change between thick and thin ice. Both ideas need to be developed further but it is already obvious that there are some major obstacles on the way to parallel milling. For example, designing a cartridge that allows parallel access of the ion beam as well as tilting over a reasonably wide angular range in the TEM still remains an unsolved technical challenge.

In contrast to the problems with the parallel milled samples, transfers of specimen with the wedge-shaped areas into the TEM were mostly successful. Here, the useable area for tomographic imaging, the so called ‘transparency length’, is limited depending on the incident angle of the milling beam (Fig. 23 *A*; (Rigort et al., 2010)). However, with grazing angles (< 10°) the area is sufficiently large (Fig. 23 *B*). Tomographic reconstructions confirmed the findings of Marko and his colleagues (Marko et al., 2007) and represent another successful example for the combination of specimen preparation by the FIB and cryo-electron tomography. It was possible to resolve structural features of the mycobacterial cell envelope at an unprecedented level of detail. In the approximately 300 – 400 nm thin regions the organization of the cytoplasmic membrane as well as the mycobacterial outer membrane, both appear as ‘symmetric’ bilayers. In addition the periplasmic layers can be clearly visualized without any indication of compression. The overall measures of the constituents are in good agreement with the data from tomograms of intact cells (Tab. 14). Though, L2 is thinner by 40% compared to the previous data. Tomograms of *M. bovis* BCG, originating from a culture in the stationary phase, show different measures for cell wall constituents compared to cells from the log-phase (Tab. 13), which denotes that the cell wall undergoes significant changes during the cell cycle. Variations in periplasmic structures are likely an effect of the maturity of the cell. More data from FIB-milled *M. smegmatis* will allow better statistics and elucidate this observation. Because of the thickness of the mycobacteria details from the cytoplasm could never be visualized in tomograms from intact cells. In cryosections, compression and the limited thickness (35 nm in case of mycobacteria and ~ 100 – 150 nm as a usable upper limit in general) weaken the information in the z-dimension. The tomograms of the *M. smegmatis* cells that were prepared by FIB milling to an ideal thickness contain a high degree of structural detail, and promise a quality step for further analyses of the undisturbed molecular organization of the cytoplasm.

Despite the obviously accurate preservation of structural details, the surface of the milled areas is non-uniform and exhibits a streak-like pattern along the milling direction (Fig. 24 *E*). These irregularities of surface topology probably originate from compositional heterogeneity of the ice-embedded specimen, which results in different sputtering rates and thus preferential milling of certain regions, referred to as ‘curtaining’ (Heymann et al., 2006). Since the samples did not exceed an initial thickness of approximately 1 μm, sputtering was accomplished relatively fast (5 minutes processing time; 30 keV ions) for the wedge shaped areas. Reasonable fast milling of thicker cellular samples requires correspondingly higher beam currents. However, low currents at shallow angles are preferable to avoid surface irregularities and to lessen the risk of thermal stress. Such conditions would increase milling times in inverse proportion to the beam current, at the risk of other unwanted sample alterations. Ion-induced structural alterations are still poorly understood. These involve local heating effects as well as the formation of a damage layer on the milled surface as a consequence of ion impact. Simulations indicate that a Ga^+ implantation zone should be restricted to a tolerable layer of 10 - 20 nm. Furthermore it has been shown, that FIB milling of vitreous ice with an ion current of 10 pA does not induce devitrification (Marko et al., 2006). However, the recently developed method of ‘cryoplaning’ (Rigort et al., 2010) holds great promise for pretrimming thick specimens directly on the vitrified grid by means of a diamond knife, before the sample is subjected to the FIB. By this way, the ion-exposure time of the sample can be significantly reduced.

Figure 41 outlines the progress of the cell wall analysis within this work. At the beginning of the project, all available data about the structure of the mycobacterial cell wall was derived from conventional EM preparations, suffering from typical artifacts and making a reliable assignment of cell wall components difficult (Fig. 41 *A*). Cryo-electron microscopy and tomography allowed us to disclose the native, undisturbed architecture of the cell envelope (Fig. 41 *B* and *C*). We proved that mycobacteria are surrounded, besides the cytoplasmic membrane, by a second 'symmetric' lipid-membrane, and thus differ significantly from the accepted models. Ultrathin cryosections of vitrified cells verified the results from intact cells and indicate the organization of the periplasmic layers in domains (Fig.41 *D*). Finally, we demonstrated the successful use of a focused ion beam for thinning vitrified cellular samples for CET (Fig. 41 *E*). Hence, mainly because compression artifacts from cryo-sectioning are avoided, it is now possible to produce high-quality preparations of mycobacteria and other microbes, suitable for the structural analysis of macromolecular complexes located in the cytoplasm and the cell envelope *in situ* by CET.

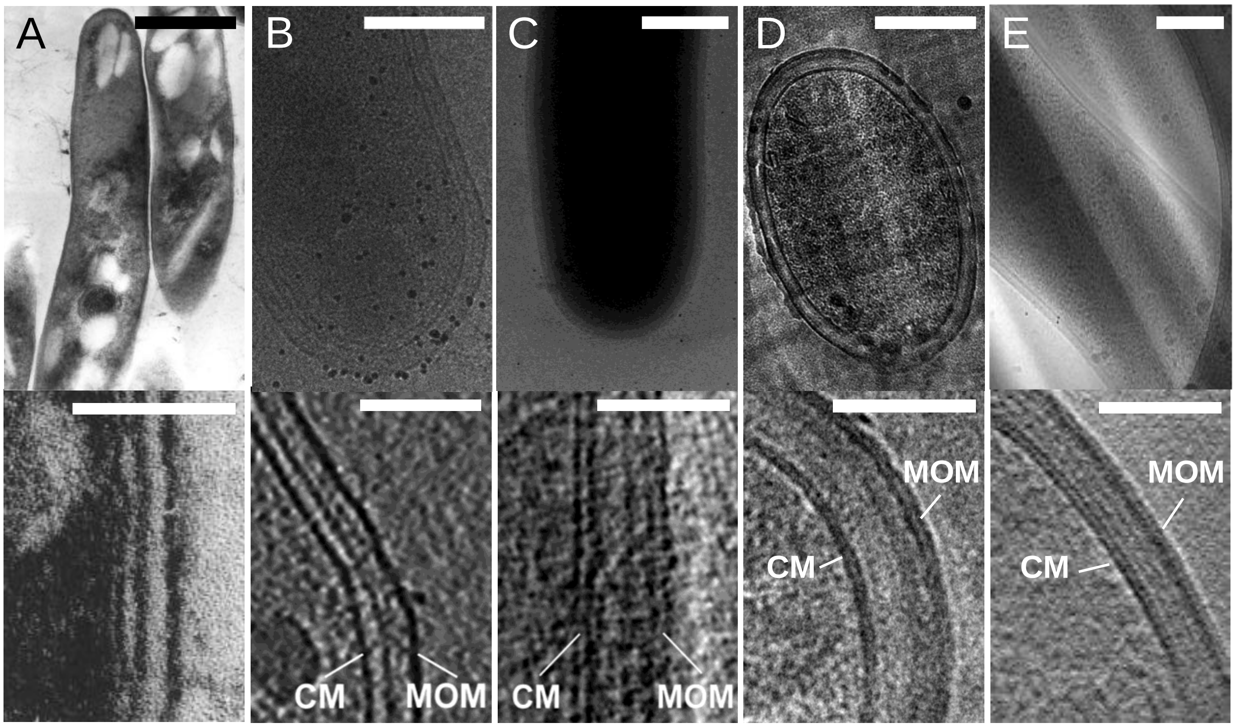

Figure 41: Progress in sample preparation and EM-imaging of mycobacterial cell walls. Upper row: TEM-projection images of different mycobacteria. (Scale bars: A, 1 µm; B – E, 250 nm.) Lower row: Enlargements from the upper row (A and D) or slices from tomographic reconstructions from the upper cells. (Scale bars: 50 nm.) **A**, *top*: Thin section of dehydrated, chemically fixed and resin embedded *M. tuberculosis*. *Bottom*: enlarged area from the upper image. The cell wall is visible as a multilayered structure, but finer details are destroyed by the harsh preparation. A reliable assignment of cell wall components is difficult. **B**, *top*: 0°-degree TEM-projection of a frozen-hydrated *M. bovis* BCG cell. *Bottom*: xy-slice from a tomographic reconstruction. The cell wall shows a multilayered appearance. Due to conventional imaging conditions for CET (high defocus and binning of the data to enhance contrast), the resolution does not allow to visualize the bilayer structure of membranes. **C**, *top*: 0°-degree TEM-projection of an 'intact' *M. smegmatis* cell, embedded in vitreous ice. The thickness and density of the cell hinders the analysis of the cytoplasm by CET. *Bottom*: xy-slice from a tomographic reconstruction. At lower defocus values and by exploiting the full resolution available, the CM as well as the MOM can be visualized as bilayers. The MOM appears symmetrical. **D**, *top*: TEM-projection of an ultrathin cryo-section of an *M. smegmatis* cell. Samples prepared by this technique are in agreement with the data collected from intact cells. *Bottom*: Enlarged area from the upper image. Because of the limited sample thickness (35 nm), the resolution of structural detail (x-y) is better, and it is possible to visualize structures in the cytoplasm, but at the expense of information in the z-direction. Furthermore, the unavoidable sample compression complicates the interpretation of the images, or in some cases, makes meaningful analysis of the data impossible. **E**, *top*: 0°- TEM-projection on an *M. smegmatis* cell, embedded in vitreous ice and thinned by a FIB. The sample has a thickness between 300 – 400 nm. Details from the cytoplasm become visible and the cells are free of compression artifacts. The irregularities in the surface topology arise from 'curtaining', but seem to have no influence on the structure of the specimen. *Bottom*: xy-slice from a tomographic reconstruction. The data of the cell wall fits the measures from tomograms of intact cells and cryosections, and mechanical compression and other effects are absent.

6.3 CET of reconstituted MspA as a model-system for *in situ* analysis of membrane proteins

Cryo-electron tomography combined with 3D image classification and averaging becomes an increasingly powerful method aiming at the analysis of the structure and interactions of macromolecular complexes in their natural context. A few examples already proved this approach successful for membrane complexes, e.g. the large nuclear pore complex (125 MDa) (Beck and Medalia, 2008), and the membrane-associated HIV-1 envelope glycoprotein (Liu et al., 2008). However, the *in situ* analysis of small and medium sized membrane proteins is hampered by a number of limitations. Chapters 5.1 and 5.2 address the problems concerning sample thickness and appropriate thinning techniques. Principal difficulties arise from the low signal-to-noise ratio and low contrast of proteins located in lipid membranes and the unfavorable focus conditions and variations in projections of tilted specimens. More appropriate focus conditions already rendered the lipid bilayer visible (cf. Ch. 5.1; (Hoffmann et al., 2008)), in contrast to all previous 3D reconstructions from microbial or other cells (Milne and Subramaniam, 2009). A more complete utilization of the 3D information in tomographical data sets is only possible by correcting the CTF for reconstruction purposes, an approach that is routinely applied in single particle EM meanwhile (Jiang et al., 2010; Sander et al., 2003). However, CTF determination and correction is not straightforward for tilted projections of notoriously low contrast. The approach described here is a methodical extension of cryo-electron tomography procedures that demonstrates that membrane protein complexes can be reliably reconstructed and how far a novel approach of correcting aberrations of the optical system can improve the attainable resolution. The size of MspA (~ 160 kDa) is representative for other membrane-bound complexes, and the results open the perspective that MspA can also be detected and investigated in tomograms of frozen-hydrated mycobacteria.

6.3.1 Reconstitution of MspA

Reconstitution of bacterial membrane proteins into lipid bilayers, either planar or vesicular, is a routine technique for functional studies (Varadhachary and Maloney, 1990). For example, Heinz and Niederweis characterized the pore-forming activity of MspA by reconstitution of the purified protein into planar lipid membranes (2000). In those special cases where a protein forms highly ordered arrays in lipid bilayers, electron crystallography (Raunser and Walz, 2009) became a standard method to image membrane proteins in their membrane environments. The structures, for instance, of bacteriorhodopsin (Kimura et al., 1997; Subramaniam and Henderson, 2000) and aquaporin-1 (Murata et al., 2000; Walz et al., 1995) were investigated by this method. A few cryo-EM studies already applied reconstitution techniques for structural analysis of membrane proteins without the need for 2D-crystallization , e.g. the work of Wang and Sigworth about the human large-conductance calcium and voltage-activated potassium channel (2009). However, to the best of my knowledge, it was not adopted for structural analysis of pore-forming bacterial outer membrane proteins by cryo-electron tomography before. Reconstitution of isolated membrane proteins that cannot be crystallized in two dimensions into lipid vesicles is advantageous insofar as problems and limitations originating from thick cellular samples (and their preparation) are bypassed. Preparation of vesicles by extrusion allows size control and an almost uniform size distribution, thus ensuring a thin ice layer. Low abundant proteins can be ‘concentrated’ on the vesicles and the time to collect a significant amount of data is reduced.

Several experimental approaches had to be tested to ensure reconstitution of MspA (cf. Ch. 5.3.1). Only one resulted in the formation of proteovesicles, where the choice of the lipid seemed to be the determining factor. The enormous variety of lipids in the mycobacterial outer membrane (Ortalo-Magne et al., 1996) precludes an exact copy *in vitro*. Only vesicles made of Diph-PC showed MspA inserted in the membrane. The four bound methyl groups of the acyl chains apparently weaken the packing of lipids and facilitate insertion of the protein. The carbon chains of the widely used lipids DMPC and DPPC are tightly packed and did not allow reconstitution, although the experiments were performed above the phase-transition temperatures of the lipids (cf. Tab. 15). The proteoliposomes obtained here represent a reproducible model system for the cryo-electron tomographical analysis of MspA, with the potential for application to other membrane proteins.

6.3.1 An extended exposure scheme for reliable CTF correction

In single particle projects, CTF correction is routinely performed in order to improve the interpretable resolution of a 3D structure (Jiang et al., 2010; Sander et al., 2003). The difficulty of detecting the Thon rings in images of low SNR and containing a defocus gradient across because of sample tilting has so far limited the implementation of CTF correction in CET. Several authors suggested promising attempts for handling these problems, but all the methods have drawbacks or limitations (Tab. 17). The performance of these methods is strongly dependent on the signal from the exposure area, thus the applied electron dose. A higher dose allows a more exact CTF correction but would damage the sample and reduce the resolution. We developed a novel approach for reliable defocus determination and subsequent CTF correction, which is completely uncoupled from the dose limitation on the exposure area. The method makes use of the geometrical relation of two positions, *f1* and *f2*, along the tilt axis of the specimen with the exposure area. High-dose images of these positions allow reliable determination of the distinct defocus values over the whole tilt-range and interpolation the subsequent CTF correction on the exposure image. The method was tested by generating 3D maps of the porin MspA embedded in the membrane of lipid vesicles, by sub-tomogram alignment and averaging. Datasets corrected for the CTF and for the MTF in addition showed an improvement in resolution, with respect to the uncorrected data, from 29.5 Å to 21.8 Å (Fig. 29). The membrane-spanning region of MspA is resolved in much more detail and the subunits can now be recognized (Figs. 30 and 31). The profits of the new method are obvious. ‘Simple’, but careful restoration of the information which is already present, led to a significantly refined resolution of structural detail. However, a more comprehensive comparison with the approaches of Fernandez (2006) and Xiong (2009) needs to be done.

Table 17: Current approaches for CTF correction in CET.

Author	Method of defocus detection	Defocus determination based on	Drawbacks and limitations	Reference
Winkler and Taylor	periodogram averaging	distinct images	better SNR than cryo- samples due to chemical fixation and plastic embedding	(Winkler and Taylor, 2003)
Fernandez	periodogram averaging	whole tiltseries	contributing information from high tiltangles inaccurate due to low SNR; CTF fluctuations of distinct images are corrected based on the average defocus value of the whole tiltseries	(Fernandez et al., 2006)
Zanetti	detection of magnification changes with the help of ice-embedded gold markers	distinct images	limited use for CET, due to electron beam induced movement of the gold markers	(Zanetti et al., 2009)
Xiong	periodogram averaging	stacks of distinct images	contributing information from high tiltangles inaccurate due to low SNR; CTF fluctuations of distinct images are corrected based on the average defocus of stacks of images	(Xiong et al., 2009)
This work	periodogram averaging on distinct images	determination of the defocus on the exposure area based on two high dose images along the tiltaxis at every tiltangle	to be analyzed	

6.3.2 Rigid body docking of the x-ray structure of MspA reveals additional densities in the corrected EM-map

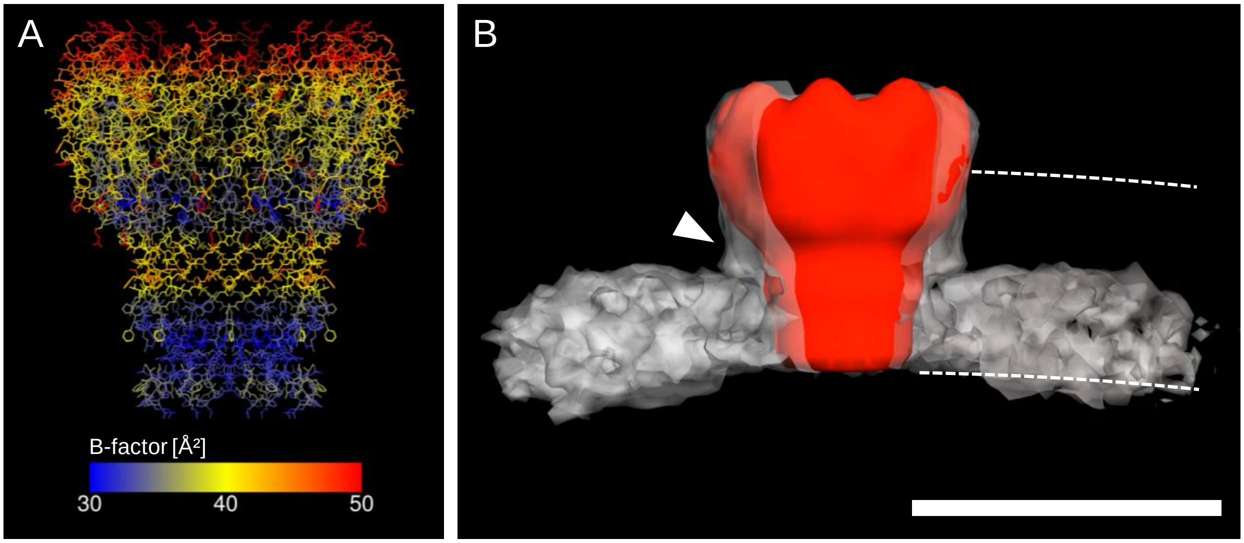

Figure 43 A.: Heat-map representation of the atomic flexibility (B-factor) of MspA. B. 'Difference map' of averaged MspA inserted in a lipid membrane with the x-ray structure filtered to a comparable resolution. The adjusted x-ray structure (*red*) docked into the average (*grey, semi-transparent*). Additional densities are visible around the stem domain at interface between the membrane and the aqueous environment (*white arrowhead*). Docking was performed with Chimera (Goddard et al., 2007). *White dashed lines* represent the dimensions of the mycobacterial outer membrane, as depicted from cryo-EM and drawn to scale.. (Scale bar: 10 nm.)

Rigid body docking of the crystal structure of MspA (Faller et al., 2004) into the EM density map shows good agreement of the overall dimensions. The upper rim of the molecule appears to be slightly smeared out (Fig. 31) which can be explained by the increased flexibility of loops in this region. This assumption is supported by the B-factor of the protein as shown in Figure 43 *A*. The indication of additional density around the stem domain of the porin (Figs. 30 and 43 *B*, *arrowhead*) is very likely not due to structure flexibility (Fig. 43 *A*), but might originate from bound material for the following reasons. The dimension (thickness) of the mycobacterial outer membrane (MOM), i.e the natural environment of MspA, and of the vesicle membrane used here as model system are different (Fig. 43 *B*). The thickness of the MOM was estimated to 7.0 to 7.5 nm (surface to surface), whereas the values for the DiphPC membrane of the vesicles are between 4.2 and 4.8 nm. Data of Mahfoud and coworkers (2006), who analyzed the topology of the porin *in situ* by labeling experiments (Fig. 5 *B*) , suggests that the base of MspA is flush with the inner surface of the MOM; similar to the situation in the model system. According to their data, the stem of MspA is entirely buried in the hydrophobic matrix of the outer membrane. In the thinner Diph-PC membrane, however, the upper part of this domain must be exposed to the aqueous surrounding. It is therefore likely that lipids and/or residual detergent molecules shield the remaining hydrophobic surface and thus contribute to the additional density in the EM-map.

This approach demonstrated that the structural analysis of proteins embedded in lipid membranes is possible; cryo-electron tomography and the application of the novel method for CTF correction leads to a significant improvement in the attainable resolution. This result is promising for investigating the topology of MspA and the structure of other protein complexes in the mycobacterial outer membrane. This goal becomes even more realistic if the quality of sample preparation is improved as discussed in chapter 6.2 (FIB).

6.3.3 Prospects for the structural analysis of other membrane proteins by CET

Reconstitution of the protein into the defined membrane of vesicles proved suitable to describe the conformation of MspA in a lipid environment resembling its natural habitat by CET. Carefully chosen settings for the acquisition (e.g. magnification, defocus, dose) allowed detection of single molecules and their reconstruction in 3D. MspA can be considered as a model for other membrane proteins exhibiting a similar size (~160 kDa). Once isolation of the protein and subsequent reconstitution into a defined membrane of lipid vesicles is established, there are no fundamental barriers preventing the investigation by CET. Here, a resolution in the range of ~ 20 Å was achieved. Increasing the number of averaged particles should improve this value even more. Even in cases where atomic models are available for some components, knowledge of their intact structures and especially their higher order organization in the plane of the membrane is of great interest (e.g. membrane receptors (Khursigara et al., 2008)). CET of reconstituted membrane proteins also facilitates the analysis of conformational variability (Liu et al., 2008). A high number of proteins in the vesicle membrane and the attainable resolution will ease detection of differences in conformational space.

The presented data clearly proved the potential of cryo-electron tomography for investigation of membrane proteins in their membrane environments. However, this method requires isolating the protein of interest. Some membrane protein complexes might be difficult to purify or to reconstitute. With continued advances on both the experimental and computational front, there is the exciting prospective that it will be possible in the near future to determine structures and structural changes of membrane protein complexes *in situ*.

6.4 Voltage-dependent gating of MspA

An interesting feature of porins is ‘gating’, i.e. closing and reopening of the channel under certain circumstances, we distinguish between ligand- and voltage-dependent channels (Jiang et al., 1997; Mobasheri and Lea, 2002; Popp et al., 1996).

Spontaneous gating of MspA at low voltages was occasionally observed (Niederweis et al., 1999) but is very rare. Gating of porins depends on the height and the polarity of the applied potential. For example, porins of *Mycobacterium chelonae* and *Mycobacterium phlei* closed in planar lipid bilayers asymmetrically at relatively low negative voltages of -40 mV and -20 mV, respectively (Riess et al., 2001; Trias and Benz, 1993). But closing events are more frequently obtained at higher voltages (Engelhardt et al., 2002). Until today, the mechanism of this phenomenon is not well understood. Different attempts were made to address the molecular determinants. When the atomic structure of MspA was solved (Faller et al., 2004), corresponding investigations focused on two possible factors responsible for the gating: the charged residues inside the pore and the periplasmic loop L6 of the porin. Studies addressing neutralization of charges were restricted to alterations in the constriction zone of MspA (Butler et al., 2008; Hoffmann, 2005). To analyze the cumulative effect of all charged residues, we constructed the mutant N-MspA, where seven aspartates (D) and two glutamates (E) along the pore’s inner lining were exchanged with the neutral amino acid asparagine (N). Asparagine was chosen because possible steric effects should be similar to that of aspartate and glutamate.

Recently, Huff et al. (2009) investigated the influence of the periplasmic loop L6 on the gating properties of MspA. Voltage gating of the *E. coli* porin OmpF was attributed to loops that collapse into the channel in response to a strong electrical field (Müller and Engel, 1999). After complete deletion of the loop L6 of MspA, the pore was still gating, even at a higher frequency (Huff et al., 2009). Large conformational changes of the loop L6 can be excluded as a factor for the closure of MspA, it rather has a stabilizing effect on the pore. To investigate the influence of the loop without the impact of charges, we constructed the mutant N-MspA ΔL6.

The conductance measurements revealed significant differences between N-MspA and N-MspA ΔL6. The average conductance of the neutral pore was slightly increased compared to that of the wild-type MspA, whereas the additional deletion of loop L6 decreased the value by ~ 25%. Interestingly, the loop mutants that still contained charged residues, showed the same average conductivity as the wild-type MspA (Huff et al., 2009). It is possible that, after deletion of the loops, the repellent forces of the 16 negative charges in the eyelet of the porin sustain its overall structure. However, removal of the charged residues and the stabilizing loop might cause a partial collapse of the constriction zone and thus a decreased conductivity. Our observations confirm the stabilizing role of the periplasmic loop of MspA since its removal led to an increased gating behavior. These results support the following assumptions: (i) The loop L6 is not responsible for the gating itself via large conformational changes, it rather has a stabilizing effect on the structure of the pore. (ii) Removal of the charges has a significant impact on the voltage-dependent closing of MspA. The exact role of the charges in the gating mechanism is still speculative. An explanation might be that the charged residues act as a ‘voltage sensor’, i.e. the external electrical field executes a force on them, reorients their average position and induces a conformation of the eyelet that is blocked for the passage of ions. Several subconductance states indicate the existence of different conformational conditions. These conformational states could represent more or less energetically favorable situations and thus could explain the different dwell times of the conductance states. Gating can also be observed for the neutral mutant N-MspA, however at a much higher potential. Asparagine residues are uncharged but polarized, thus exhibiting a dipole momentum. The force of the electric field could then change their orientation as well. These assumptions still need further experimental investigations before a clearer picture of the mechanism underlying the voltage-dependent closing of MspA can be drawn. Nevertheless, the results will be of interest for utilizing MspA for nanotechnical applications. Recently, MspA attracted interest by using it as a nanopore for the sequencing of DNA (Butler et al., 2008). The authors also addressed the voltage-dependent closing of MspA, which severely hampers the translocation experiments. N-MspA remains stable in an open state up to higher potentials compared to the wild-type, and appears to be a promising candidate for similar investigations.

Until today, it remains unclear whether the gating phenomenon that is observed for other porins as well (Liu and Delcour, 1998; Mathes and Engelhardt, 1998; Saxena et al., 1999) has a physiological meaning for the bacterial cell. It is conceivable that by variation of the membrane potential the number of open channels can be controlled. However, the existence of such a membrane potential could not be proven yet for mycobacteria, in contrast to *E. coli* (Sen et al., 1988). An asymmetric lipid distribution (intrinsic membrane potential) or an asymmetric charge distribution (Donnan potential) could lead to the formation of such a potential (Riess et al., 2001). If such a potential does not exist or is too low, the closing phenomenon of the channels might just be an *in vitro* effect.

.

7 Outlook

Classical electron microscopy of biological specimens poses serious difficulties for a reliable interpretation of structural details. Dehydrating, staining and embedding can alter and destroy the fragile molecular ensemble and the native state remains unrecognized. One example is the initial situation in the framework of this thesis. The model of the mycobacterial cell wall, derived mainly from conventional electron microscopical preparations, did not agree with the atomic structure of the porin MspA (Faller et al., 2004; Mahfoud et al., 2006). The aim of this work was to evaluate how and to what extent cryo-electron microscopy can be applied to explore the native state of MspA and its natural environment *in situ*.

Cryopreparation (i.e. thinning) of mycobacterial cells is a prerequisite for achieving a reasonable resolution of molecular assemblies. Cryosectioning is of limited use due to the inherent artifacts and compression effects (Al-Amoudi et al., 2005). The results obtained from mycobacteria thinned by a focused ion beam (FIB) were promising with regard to sample quality and structural preservation. Nevertheless, this approach is technically demanding and there are still aspects that need to be addressed and investigated in more detail. Further technical improvements of the cryo-transfer system, e.g., a sample holding cartridge that allows operation in the FIB as well as in the TEM, will reduce mechanical stress on the grids and ease transfer of the milled areas. Efforts in developing a setup suitable for preparing and handling lamellar or cylindrical samples will avoid limitations in tomographical data acquisition (‘missing wedge’) and increase the accessible areas of the cell compared to wedge-shaped milling. Three-dimensional reconstruction of a *M. smegmatis* cell thinned by FIB milling revealed structures at a so far unrivaled level of detail. With ongoing progress, this method of sample preparation shows great promise to achieve a quality of structural preservation that allows the *in situ* investigation of constituents of the microbial cell wall, and in particular of proteins embedded in membranes such as MspA by cryo-electron microscopy. Reconstitution of MspA in the membrane of defined lipid vesicles, thus circumventing the limitations of sample thickness, allowed the structural research of the porin in an environment resembling its native habitat by cryo-electron tomography. Extending the data acquisition scheme made a reliable CTF-correction possible, and significantly improved the attainable resolution. In order to speed up the acquisition, recording of the two additional high dose images has to be automated and implemented into the microscope control software. Combining the distinct routines involved in the post-processing (CTF fitting and correction) to a single program will further reduce the time and make the approach more user-friendly. Nevertheless, a comparative evaluation still has to prove the advantages of correcting the CTF in every single image of a tiltseries instead of assessing average defocus for the whole series (Fernandez et al., 2006) or for subsets (Xiong et al., 2009). The data itself also leaves room for improvement. Exploiting the full resolution available (i.e. unbinned images) as well as extending the number of MspA-containing subtomograms will further improve the level of structural detail. Extending the new method to other investigations of macromolecular complexes *in situ*, e.g. the 3D organization of ribosomes (Brandt et al., 2009), will further demonstrate its potential. The gain in resolution should be of advantage for template-matching in general.

MspA is the only mycobacterial pore protein whose function has been investigated in some detail. Nevertheless, the phenomenon of voltage-dependent closing is still not well understood. Conductivity measurements showed that charged residues inside MspA are a major determinant of the gating behavior, whereas the periplasmic loop L6 exerts a stabilizing effect on the pore. A more complete evaluation of the observed subconductance states and their dwell times, further conductance-salt and conductance-pH measurements should give more insight into the pore properties of MspA, as well as molecular dynamic simulations. But a final understanding of the mechanistic background of voltage-dependent closing of MspA will still remain a challenge. In terms of nanotechnical applications, the least voltage-sensitive mutant N-MspA represents a promising candidate. Translocation experiments will reveal its suitability for nanopore sequencing of DNA.

8 References

Al-Amoudi, A., Chang, J.J., Leforestier, A., McDowall, A., Salamin, L.M., Norlen, L.P., Richter, K., Blanc, N.S., Studer, D., and Dubochet, J. (2004). Cryo-electron microscopy of vitreous sections. *Embo* J *23*, 3583-3588.

Al-Amoudi, A., Studer, D., and Dubochet, J. (2005). Cutting artefacts and cutting process in vitreous sections for cryo-electron microscopy. *J Struct Biol 150*, 109-121.

Alahari, A., Saint, N., Campagna, S., Molle, V., Molle, G., and Kremer, L. (2007). The N-terminal domain of OmpATb is required for membrane translocation and pore-forming activity in mycobacteria. *J Bacteriol 189*, 6351-6358.

Angelova, M.I. (2001). Giant Vesicles. In Liposome electroformation, P.L. Luisi, and P. Walde, eds. (Chichester, John Wiley and Sons), pp. 27-36.

Ausubel, F.M., Brent, R., Kingston, R.E., Moore, D.D., Seidmann, J.G., Smith, J.A., and Struhl, K. (1987). *Current Protocols in Molecular Biology*.

Barry, C.E., 3rd, Lee, R.E., Mdluli, K., Sampson, A.E., Schroeder, B.G., Slayden, R.A., and Yuan, Y. (1998). Mycolic acids: structure, biosynthesis and physiological functions. *Prog Lipid Res 37*, 143-179.

Barry, C.E., 3rd, and Mdluli, K. (1996). Drug sensitivity and environmental adaptation of mycobacterial cell wall components. *Trends Microbiol 4*, 275-281.

Bayan, N., Houssin, C., Chami, M., and Leblon, G. (2003). Mycomembrane and S-layer: two important structures of Corynebacterium glutamicum cell envelope with promising biotechnology applications. *J Biotechnol 104*, 55-67.

Beck, M., and Medalia, O. (2008). Structural and functional insights into nucleocytoplasmic transport. *Histol Histopathol 23*, 1025-1033.

Bi, W., and Stambrook, P.J. (1997). CCR: a rapid and simple approach for mutation detection. *Nucleic Acids Res 25*, 2949-2951.

Bleed, D.M. (2001). Worldwide epidemiology of tuberculosis. Pediatr Pulmonol *Suppl 23*, 60.
Bouchet-Marquis, C., Dubochet, J., and Fakan, S. (2006). Cryoelectron microscopy of vitrified sections: a new challenge for the analysis of functional nuclear architecture. *Histochem Cell Biol 125*, 43-51.

Brandt, F., Etchells, S.A., Ortiz, J.O., Elcock, A.H., Hartl, F.U., and Baumeister, W. (2009). The native 3D organization of bacterial polysomes. *Cell 136*, 261-271.

Braun, V., Rotering, H., Ohms, J.P., and Hagenmaier, H. (1976). Conformational studies on murein-lipoprotein from the outer membrane of *Escherichia coli*. *Eur J Biochem 70*, 601-610.

Brennan, P.J., and Goren, M.B. (1979). Structural studies on the type-specific antigens and lipids of the mycobacterium avium.Mycobacterium intracellulare.Mycobacterium scrofulaceum serocomplex. Mycobacterium intracellulare serotype 9. *J Biol Chem 254*, 4205-4211.

Brennan, P.J., and Nikaido, H. (1995). The envelope of mycobacteria. *Annu Rev Biochem 64*, 29-63.

Butler, T.Z., Pavlenok, M., Derrington, I.M., Niederweis, M., and Gundlach, J.H. (2008). Single-molecule DNA detection with an engineered MspA protein nanopore. *Proc Natl Acad Sci U S A 105*, 20647-20652.

Chatterjee, D. (1997). The mycobacterial cell wall: structure, biosynthesis and sites of drug action. *Curr Opin Chem Biol 1*, 579-588.

Cole, S.T., Brosch, R., Parkhill, J., Garnier, T., Churcher, C., Harris, D., Gordon, S.V., Eiglmeier, K., Gas, S., Barry, C.E., 3rd, *et al.* (1998). Deciphering the biology of Mycobacterium tuberculosis from the complete genome sequence. *Nature 393*, 537-544.

Cowan, S.W., Schirmer, T., Rummel, G., Steiert, M., Ghosh, R., Pauptit, R.A., Jansonius, J.N., and Rosenbusch, J.P. (1992). Crystal structures explain functional properties of two E. coli porins. *Nature 358*, 727-733.

Crick, D.C., Mahapatra, S., and Brennan, P.J. (2001). Biosynthesis of the arabinogalactan-peptidoglycan complex of Mycobacterium tuberculosis. *Glycobiology 11*, 107R-118R.

Crowther, R.A., Amos, L.A., Finch, J.T., De Rosier, D.J., and Klug, A. (1970). Three dimensional reconstructions of spherical viruses by fourier synthesis from electron micrographs. *Nature 226*, 421-425.

Daffe, M., and Draper, P. (1998). The envelope layers of mycobacteria with reference to their pathogenicity. *Adv Microb Physiol 39*, 131-203.

Daniel, J., Deb, C., Dubey, V.S., Sirakova, T.D., Abomoelak, B., Morbidoni, H.R., and Kolattukudy, P.E. (2004). Induction of a novel class of diacylglycerol acyltransferases and triacylglycerol accumulation in Mycobacterium tuberculosis as it goes into a dormancy-like state in culture. *J Bacteriol 186*, 5017-5030.

Deshayes, C., Laval, F., Montrozier, H., Daffe, M., Etienne, G., and Reyrat, J.M. (2005). A glycosyltransferase involved in biosynthesis of triglycosylated glycopeptidolipids in Mycobacterium smegmatis: impact on surface properties. *J Bacteriol 187*, 7283-7291.

Dierksen, K., Typke, D., Hegerl, R., Koster, A.J., and Baumeister, W. (1992). Towards Automatic Electron Tomography. *Ultramicroscopy 40*, 71-87.

Dierksen, K., Typke, D., Hegerl, R., Walz, J., Sackmann, E., and Baumeister, W. (1995). Three-dimensional structure of lipid vesicles embedded in vitreous ice and investigated by automated electron tomography. *Biophys J 68*, 1416-1422.

Dmitriev, B.A., Ehlers, S., Rietschel, E.T., and Brennan, P.J. (2000). Molecular mechanics of the mycobacterial cell wall: from horizontal layers to vertical scaffolds. *Int J Med Microbiol 290*, 251-258.

Dover, L.G., Cerdeno-Tarraga, A.M., Pallen, M.J., Parkhill, J., and Besra, G.S. (2004). Comparative cell wall core biosynthesis in the mycolated pathogens, Mycobacterium tuberculosis and Corynebacterium diphtheriae. *FEMS Microbiol Rev 28*, 225-250.

Dubochet, J., Adrian, M., Chang, J.J., Homo, J.C., Lepault, J., McDowall, A.W., and Schultz, P. (1988). Cryo-electron microscopy of vitrified specimens. *Q Rev Biophys 21*, 129-228.

Dubochet, J., and Sartori Blanc, N. (2001). The cell in absence of aggregation artifacts. *Micron 32*, 91-99.

Dusch, N., Puhler, A., and Kalinowski, J. (1999). Expression of the Corynebacterium glutamicum panD gene encoding L-aspartate-alpha-decarboxylase leads to pantothenate overproduction in *Escherichia coli. Appl Environ Microbiol 65*, 1530-1539.

Engelhardt, H., Heinz, C., and Niederweis, M. (2002). A tetrameric porin limits the cell wall permeability of *Mycobacterium smegmatis. J Biol Chem 277*, 37567-37572.

Espinal, M.A., Kim, S.J., Suarez, P.G., Kam, K.M., Khomenko, A.G., Migliori, G.B., Baez, J., Kochi, A., Dye, C., and Raviglione, M.C. (2000). Standard short-course chemotherapy for drug-resistant tuberculosis: treatment outcomes in 6 countries. *Jama 283*, 2537-2545.

Etienne, G., Laval, F., Villeneuve, C., Dinadayala, P., Abouwarda, A., Zerbib, D., Galamba, A., and Daffe, M. (2005). The cell envelope structure and properties of Mycobacterium smegmatis mc(2)155: is there a clue for the unique transformability of the strain? *Microbiology 151*, 2075-2086.

Faller, M., Niederweis, M., and Schulz, G.E. (2004). The structure of a mycobacterial outer-membrane channel. *Science 303*, 1189-1192.

Farre, C., Haythornthwaite, A., Haarmann, C., Stoelzle, S., Kreir, M., George, M., Bruggemann, A., and Fertig, N. (2009). Port-a-patch and patchliner: high fidelity electrophysiology for secondary screening and safety pharmacology. *Comb Chem High Throughput Screen 12*, 24-37.

Farre, C., Stoelzle, S., Haarmann, C., George, M., Bruggemann, A., and Fertig, N. (2007). Automated ion channel screening: patch clamping made easy. *Expert Opin Ther Targets 11*, 557-565.

Fernandez, J.J., Li, S., and Crowther, R.A. (2006). CTF determination and correction in electron cryotomography. *Ultramicroscopy 106*, 587-596.

Fernandez, J.J., Sanjurjo, J.R., and Carazo, J.M. (1997). A spectral estimation approach to contrast transfer function detection in electron microscopy. *Ultramicroscopy 68*, 267-295.

Frangakis, A.S., and Hegerl, R. (2001). Noise reduction in electron tomographic reconstructions using nonlinear anisotropic diffusion. *J Struct Biol 135*, 239-250.

Frank, J. (1996). Three-Dimensional Electron Microscopy of Macromolecular Assemblies (San Diego, Academic Press).

Fu, L.M., and Fu-Liu, C.S. (2002). Is Mycobacterium tuberculosis a closer relative to Gram-positive or Gram-negative bacterial pathogens? *Tuberculosis* (Edinb) *82*, 85-90.

Gebhardt, H., Meniche, X., Tropis, M., Kramer, R., Daffe, M., and Morbach, S. (2007). The key role of the mycolic acid content in the functionality of the cell wall permeability barrier in Corynebacterineae. *Microbiology 153*, 1424-1434.

Giannuzzi, L.A., and Stevie, F.A.E. (2005). Introduction to focused ion beams (New York, Springer).

Goddard, T.D., Huang, C.C., and Ferrin, T.E. (2007). Visualizing density maps with UCSF Chimera. *J Struct Biol 157*, 281-287.

Gupta, R.S. (1998). Protein phylogenies and signature sequences: A reappraisal of evolutionary relationships among archaebacteria, eubacteria, and eukaryotes. *Microbiol Mol Biol Rev 62*, 1435-1491.

Gupta, S., and Chatterji, D. (2005). Stress responses in mycobacteria. *IUBMB Life 57*, 149-159.

Hanahan, D., Jessee, J., and Bloom, F.R. (1991). Plasmid transformation of Escherichia coli and other bacteria. *Methods Enzymol 204*, 63-113.

Hartmans, S., De Bont, J.A.M., and Stackebrandt, E. (2004). The Genus Mycobacterium-Nonmedical. The Prokaryotes, online edition.

Heinz, C., Engelhardt, H., and Niederweis, M. (2003a). The core of the tetrameric mycobacterial porin MspA is an extremely stable beta-sheet domain. *J Biol Chem 278*, 8678-8685.

Heinz, C., and Niederweis, M. (2000). Selective extraction and purification of a mycobacterial outer membrane protein. *Anal Biochem 285*, 113-120.

Heinz, C., Roth, E., and Niederweis, M. (2003b). Purification of porins from Mycobacterium smegmatis. *Methods Mol Biol 228*, 139-150.

Heller, H., Schaefer, M., and Schulten, K. (1993). Molecular dynamics simulation of a bilayer of 200 lipids in the gel and in the liquid crystal phase. *J Phys Chem 97*, 8343-8360.

Henderson, R. (1995). The potential and limitations of neutrons, electrons and X-rays for atomic resolution microscopy of unstained biological molecules. *Q Rev Biophys 28*, 171-193.

Henderson, R., Baldwin, J.M., Ceska, T.A., Zemlin, F., Beckmann, E., and Downing, K.H. (1990). Model for the structure of bacteriorhodopsin based on high-resolution electron cryo-microscopy. *J Mol Biol 213*, 899-929.

Heymann, J.A., Hayles, M., Gestmann, I., Giannuzzi, L.A., Lich, B., and Subramaniam, S. (2006). Site-specific 3D imaging of cells and tissues with a dual beam microscope. *J Struct Biol 155*, 63-73.

Hillmann, D., Eschenbacher, I., Thiel, A., and Niederweis, M. (2007). Expression of the major porin gene mspA is regulated in Mycobacterium smegmatis. *J Bacteriol 189*, 958-967.

Hoffmann, C. (2005). Construction and functional analysis of constriction zone mutants of *Mycobacterium smegmatis* porin A (MspA). In Institut für Mikrobiologie, Biochemie und Genetik (Erlangen, Friedrich-Alexander-Universität Erlangen-Nürnberg), pp. 105.

Hoffmann, C., Leis, A., Niederweis, M., Plitzko, J.M., and Engelhardt, H. (2008). Disclosure of the mycobacterial outer membrane: cryo-electron tomography and vitreous sections reveal the lipid bilayer structure. *Proc Natl Acad Sci U S A 105*, 3963-3967.

Honer zu Bentrup, K., and Russell, D.G. (2001). Mycobacterial persistence: adaptation to a changing environment. *Trends Microbiol 9*, 597-605.

Hong, X., and Hopfinger, A.J. (2004). Construction, molecular modeling, and simulation of Mycobacterium tuberculosis cell walls. *Biomacromolecules 5*, 1052-1065.

Hsieh, C.E., Leith, A., Mannella, C.A., Frank, J., and Marko, M. (2006). Towards high-resolution three-dimensional imaging of native mammalian tissue: electron tomography of frozen-hydrated rat liver sections. *J Struct Biol 153*, 1-13.

Hsieh, C.E., Marko, M., Frank, J., and Mannella, C.A. (2002). Electron tomographic analysis of frozen-hydrated tissue sections. *J Struct Biol 138*, 63-73.

Huff, J., Pavlenok, M., Sukumaran, S., and Niederweis, M. (2009). Functions of the periplasmic loop of the porin MspA from *Mycobacterium smegmatis. J Biol Chem 284*, 10223-10231.

Jackson, M., Crick, D.C., and Brennan, P.J. (2000). Phosphatidylinositol is an essential phospholipid of mycobacteria. *J Biol Chem 275*, 30092-30099.

Jarlier, V., and Nikaido, H. (1990). Permeability barrier to hydrophilic solutes in Mycobacterium chelonei. *J Bacteriol 172*, 1418-1423.

Jiang, L., Liu, Z., Georgieva, D., Kuil, M.E., and Abrahams, J.P. (2010). A novel approximation method of CTF amplitude correction for 3D single particle reconstruction. *Ultramicroscopy 110*, 350-358.

Jiang, X., Payne, M.A., Cao, Z., Foster, S.B., Feix, J.B., Newton, S.M., and Klebba, P.E. (1997). Ligand-specific opening of a gated-porin channel in the outer membrane of living bacteria. *Science 276*, 1261-1264.

Kaps, I., Ehrt, S., Seeber, S., Schnappinger, D., Martin, C., Riley, L.W., and Niederweis, M. (2001). Energy transfer between fluorescent proteins using a co-expression system in *Mycobacterium smegmatis. Gene 278*, 115-124.

Khursigara, C.M., Wu, X., Zhang, P., Lefman, J., and Subramaniam, S. (2008). Role of HAMP domains in chemotaxis signaling by bacterial chemoreceptors. *Proc Natl Acad Sci U S A 105*, 16555-16560.

Kimura, Y., Vassylyev, D.G., Miyazawa, A., Kidera, A., Matsushima, M., Mitsuoka, K., Murata, K., Hirai, T., and Fujiyoshi, Y. (1997). Surface of bacteriorhodopsin revealed by high-resolution electron crystallography. *Nature 389*, 206-211.

Kirk, E.C.G., Williams, D.A., and Ahmed, H. (1989). Cross-sectional transmission electron microscopy of precisely selected regions from semiconductor devices. *Institute of Physics Conference Series*, 501-506.

Knott, G., Marchman, H., Wall, D., and Lich, B. (2008). Serial section scanning electron microscopy of adult brain tissue using focused ion beam milling. *J Neurosci 28*, 2959-2964.

Koch, R. (1882). Classics in infectious diseases. The etiology of tuberculosis: Robert Koch. *Rev Infect Dis 4*, 1270-1274.

Koster, A.J., Grimm, R., Typke, D., Hegerl, R., Stoschek, A., Walz, J., and Baumeister, W. (1997). Perspectives of molecular and cellular electron tomography. *J Struct Biol 120*, 276-308.

Koster, A.J., Ruijter, W.J.d., Bos, A.v.d., and Mast, K.D.v.d. (1989). Autotuning of a TEM using minimum electron dose. *Ultramicroscopy 27*, 72.

Kreusch, A., and Schulz, G.E. (1994). Refined structure of the porin from Rhodopseudomonas blastica. Comparison with the porin from Rhodobacter capsulatus. *J Mol Biol 243*, 891-905.

Lakshminarayanan, A.V., and Lent, A. (1979). Methods of least squares and SIRT in reconstruction. *J Theor Biol 76*, 267-295.

Landt, O., Grunert, H.P., and Hahn, U. (1990). A general method for rapid site-directed mutagenesis using the polymerase chain reaction. *Gene 96*, 125-128.

Lawn, S.D., and Wilkinson, R. (2006). Extensively drug resistant tuberculosis. *Bmj 333*, 559-560.

Lee, R.E., Brennan, P.J., and Besra, G.S. (1996). Mycobacterium tuberculosis cell envelope. *Curr Top Microbiol Immunol 215*, 1-27.

Leis, A., Rockel, B., Andrees, L., and Baumeister, W. (2009). Visualizing cells at the nanoscale. *Trends Biochem Sci 34*, 60-70.

Lindsey, H., Petersen, N.O., and Chan, S.I. (1979). Physicochemical characterization of 1,2-diphytanoyl-sn-glycero-3-phosphocholine in model membrane systems. *Biochim Biophys Acta 555*, 147-167.

Liu, J., Bartesaghi, A., Borgnia, M.J., Sapiro, G., and Subramaniam, S. (2008). Molecular architecture of native HIV-1 gp120 trimers. *Nature 455*, 109-113.

Liu, J., Rosenberg, E.Y., and Nikaido, H. (1995). Fluidity of the lipid domain of cell wall from Mycobacterium chelonae. *Proc Natl Acad Sci U S A 92*, 11254-11258.

Liu, N., and Delcour, A.H. (1998). The spontaneous gating activity of OmpC porin is affected by mutations of a putative hydrogen bond network or of a salt bridge between the L3 loop and the barrel. *Protein Eng 11*, 797-802.

Lucic, V., Forster, F., and Baumeister, W. (2005). Structural studies by electron tomography: from cells to molecules. *Annu Rev Biochem 74*, 833-865.

Mahfoud, M., Sukumaran, S., Hulsmann, P., Grieger, K., and Niederweis, M. (2006). Topology of the porin MspA in the outer membrane of Mycobacterium smegmatis. *J Biol Chem 281*, 5908-5915.

Malis, T., Cheng, S.C., and Egerton, R.F. (1988). EELS log-ratio technique for specimen-thickness measurement in the TEM. *J Electron Microsc Tech 8*, 193-200.

Marko, M., Hsieh, C., Moberlychan, W., Mannella, C.A., and Frank, J. (2006). Focused ion beam milling of vitreous water: prospects for an alternative to cryo-ultramicrotomy of frozen-hydrated biological samples. *J Microsc 222*, 42-47.

Marko, M., Hsieh, C., Schalek, R., Frank, J., and Mannella, C. (2007). Focused-ion-beam thinning of frozen-hydrated biological specimens for cryo-electron microscopy. *Nat Methods 4*, 215-217.

Masich, S., Ostberg, T., Norlen, L., Shupliakov, O., and Daneholt, B. (2006). A procedure to deposit fiducial markers on vitreous cryo-sections for cellular tomography. *J Struct Biol 156*, 461-468.

Mastronarde, D.N. (1997). Dual-axis tomography: an approach with alignment methods that preserve resolution. *J Struct Biol 120*, 343-352.

Mathes, A., and Engelhardt, H. (1998). Voltage-dependent closing of porin channels: analysis of relaxation kinetics. *J Membr Biol 165*, 11-18.

Matias, V.R., Al-Amoudi, A., Dubochet, J., and Beveridge, T.J. (2003). Cryo-transmission electron microscopy of frozen-hydrated sections of Escherichia coli and Pseudomonas aeruginosa. *J Bacteriol 185*, 6112-6118.

McDowall, A.W., Chang, J.J., Freeman, R., Lepault, J., Walter, C.A., and Dubochet, J. (1983). Electron microscopy of frozen hydrated sections of vitreous ice and vitrified biological samples. *J Microsc 131*, 1-9.

McEwen, B.F., Downing, K.H., and Glaeser, R.M. (1995). The relevance of dose-fractionation in tomography of radiation-sensitive specimens. *Ultramicroscopy 60*, 357-373.

Milne, J.L., and Subramaniam, S. (2009). Cryo-electron tomography of bacteria: progress, challenges and future prospects. *Nat Rev Microbio*l *7*, 666-675.

Mindell, J.A., and Grigorieff, N. (2003). Accurate determination of local defocus and specimen tilt in electron microscopy. *J Struct Biol 142*, 334-347.

Mineda, T., Ohara, N., Yukitake, H., and Yamada, T. (1998). The ribosomes contents of mycobacteria. *New Microbiol 21*, 1-7.

Minnikin, D.E. (1991). Chemical principles in the organization of lipid components in the mycobacterial cell envelope. *Res Microbiol 142*, 423-427.

Minnikin, D.E., Minnikin, S.M., Goodfellow, M., and Stanford, J.L. (1982). The mycolic acids of Mycobacterium chelonei. *J Gen Microbiol 128*, 817-822.

MirAfzali, Z., Leipprandt, J.R., McCracken, J.L., and DeWitt, D.L. (2005). Fast, efficient reconstitution of the cyclooxygenases into proteoliposomes. *Arch Biochem Biophys 443*, 60-65.

Mobasheri, H., and Lea, E.J. (2002). Biophysics of gating phenomena in voltage-dependent OmpC mutant porin channels (R74C and R37C) of Escherichia coli outer membranes. *Eur Biophys* J *31*, 389-399.

Mulders, H. (2003). The use of a SEM/FIB DualBeam applied to biological samples. *GIT Imaging & Microscopy*, 8-10.

Müller, D.J., and Engel, A. (1999). Voltage and pH-induced channel closure of porin OmpF visualized by atomic force microscopy. *J Mol Biol 285*, 1347-1351.

Mullis, K., Faloona, F., Scharf, S., Saiki, R., Horn, G., and Erlich, H. (1986). Specific enzymatic amplification of DNA in vitro: the polymerase chain reaction. *Cold Spring Harb Symp Quant Biol 51 Pt 1*, 263-273.

Murakami, S., Nakashima, R., Yamashita, E., and Yamaguchi, A. (2002). Crystal structure of bacterial multidrug efflux transporter AcrB. *Nature 419*, 587-593.

Murata, K., Mitsuoka, K., Hirai, T., Walz, T., Agre, P., Heymann, J.B., Engel, A., and Fujiyoshi, Y. (2000). Structural determinants of water permeation through aquaporin-1. *Nature 407*, 599-605.

Nakae, T. (1976). Outer membrane of Salmonella. Isolation of protein complex that produces transmembrane channels. *J Biol Chem 251*, 2176-2178.

Nickell, S., Forster, F., Linaroudis, A., Net, W.D., Beck, F., Hegerl, R., Baumeister, W., and Plitzko, J.M. (2005). TOM software toolbox: acquisition and analysis for electron tomography. *J Struct Biol 149*, 227-234.

Niederweis, M. (2003). Mycobacterial porins--new channel proteins in unique outer membranes. *Mol Microbiol 49*, 1167-1177.

Niederweis, M., Ehrt, S., Heinz, C., Klocker, U., Karosi, S., Swiderek, K.M., Riley, L.W., and Benz, R. (1999). Cloning of the mspA gene encoding a porin from Mycobacterium smegmatis. *Mol Microbiol 33*, 933-945.

Nikaido, H. (1994). Porins and specific diffusion channels in bacterial outer membranes. *J Biol Chem 269*, 3905-3908.

Nikaido, H., Kim, S.H., and Rosenberg, E.Y. (1993). Physical organization of lipids in the cell wall of Mycobacterium chelonae. *Mol Microbiol 8*, 1025-1030.

Ortalo-Magne, A., Lemassu, A., Laneelle, M.A., Bardou, F., Silve, G., Gounon, P., Marchal, G., and Daffe, M. (1996). Identification of the surface-exposed lipids on the cell envelopes of Mycobacterium tuberculosis and other mycobacterial species. *J Bacteriol 178*, 456-461.

Parmar, M.M., Edwards, K., and Madden, T.D. (1999). Incorporation of bacterial membrane proteins into liposomes: factors influencing protein reconstitution. *Biochim Biophys Acta 1421*, 77-90.

Parrish, N.M., Dick, J.D., and Bishai, W.R. (1998). Mechanisms of latency in Mycobacterium tuberculosis. *Trends Microbiol 6*, 107-112.

Pascual, C., Lawson, P.A., Farrow, J.A., Gimenez, M.N., and Collins, M.D. (1995). Phylogenetic analysis of the genus Corynebacterium based on 16S rRNA gene sequences. *Int J Syst Bacteriol 45*, 724-728.

Paul, T.R., and Beveridge, T.J. (1992). Reevaluation of envelope profiles and cytoplasmic ultrastructure of mycobacteria processed by conventional embedding and freeze-substitution protocols. *J Bacteriol 174*, 6508-6517.

Paul, T.R., and Beveridge, T.J. (1994). Preservation of surface lipids and determination of ultrastructure of Mycobacterium kansasii by freeze-substitution. *Infect Immun 62*, 1542-1550.

Penczek, P., Marko, M., Buttle, K., and Frank, J. (1995). Double-tilt electron tomography. *Ultramicroscopy 60*, 393-410.

Pitulle, C., Dorsch, M., Kazda, J., Wolters, J., and Stackebrandt, E. (1992). Phylogeny of rapidly growing members of the genus Mycobacterium. *Int J Syst Bacteriol 42*, 337-343.

Popp, B., Court, D.A., Benz, R., Neupert, W., and Lill, R. (1996). The role of the N and C termini of recombinant Neurospora mitochondrial porin in channel formation and voltage-dependent gating. *J Biol Chem 271*, 13593-13599.

Portevin, D., De Sousa-D'Auria, C., Houssin, C., Grimaldi, C., Chami, M., Daffe, M., and Guilhot, C. (2004). A polyketide synthase catalyzes the last condensation step of mycolic acid biosynthesis in mycobacteria and related organisms. *Proc Natl Acad Sci U S A 101*, 314-319.

Puech, V., Chami, M., Lemassu, A., Laneelle, M.A., Schiffler, B., Gounon, P., Bayan, N., Benz, R., and Daffe, M. (2001). Structure of the cell envelope of corynebacteria: importance of the non-covalently bound lipids in the formation of the cell wall permeability barrier and fracture plane. *Microbiology 147*, 1365-1382.

Radermacher, M., Wagenknecht, T., Verschoor, A., and Frank, J. (1986). A new 3-D reconstruction scheme applied to the 50S ribosomal subunit of E. coli. J Microsc *141*, RP1-2.
Radon, J. (1917). Über die Bestimmung von Funktionen durch ihre Integralwerte längs gewisser Mannigfaltigkeiten. *Math Phys Klasse 69*, 262-277.

Rastogi, N., Hellio, R., and David, H.L. (1991). A new insight into the mycobacterial cell envelope architecture by the localization of antigens in ultrathin sections. *Zentralbl Bakteriol 275*, 287-302.

Rastogi, N., Legrand, E., and Sola, C. (2001). The mycobacteria: an introduction to nomenclature and pathogenesis. *Rev Sci Tech 20*, 21-54.

Raunser, S., and Walz, T. (2009). Electron crystallography as a technique to study the structure on membrane proteins in a lipidic environment. *Annu Rev Biophys 38*, 89-105.

Raynaud, C., Papavinasasundaram, K.G., Speight, R.A., Springer, B., Sander, P., Bottger, E.C., Colston, M.J., and Draper, P. (2002). The functions of OmpATb, a pore-forming protein of Mycobacterium tuberculosis. *Mol Microbiol 46*, 191-201.

Reimer, L., and Rossmessemer, M. (1989). Contrast In The Electron Spectroscopic Imaging Mode Of A TEM. 1. Influence Of Zero-Loss Filtering On Scattering Contrast *Journal of Microscopy-Oxford 155*, 169-182.

Rieder, H.L., Zellweger, J.P., Raviglione, M.C., Keizer, S.T., and Migliori, G.B. (1994). Tuberculosis control in Europe and international migration. *Eur Respir J 7*, 1545-1553.

Riess, F.G., Dorner, U., Schiffler, B., and Benz, R. (2001). Study of the properties of a channel-forming protein of the cell wall of the gram-positive bacterium *Mycobacterium phlei. J Membr Biol 182*, 147-157.

Rigort, A., Bauerlein, F.J., Leis, A., Gruska, M., Hoffmann, C., Laugks, T., Bohm, U., Eibauer, M., Gnaegi, H., Baumeister, W., *et al.* (2010). Micromachining tools and correlative approaches for cellular cryo-electron tomography. *J Struct Biol.*

Rogall, T., Wolters, J., Flohr, T., and Bottger, E.C. (1990). Towards a phylogeny and definition of species at the molecular level within the genus Mycobacterium. *Int J Syst Bacteriol 40*, 323-330.

Russell, D.G. (2001). *Mycobacterium tuberculosis*: here today, and here tomorrow. *Nat Rev Mol Cell Biol 2*, 569-577.

Sambrook, J., Fritsch, E.F., and Maniatis, T. (1989). Molecular cloning: a laboratory manual, 2nd edn (Cold Spring Harbor, N.Y., Cold Spring Harbor Laboratory Press).

Samei, E., Buhr, E., Granfors, P., Vandenbroucke, D., and Wang, X. (2005). Comparison of edge analysis techniques for the determination of the MTF of digital radiographic systems. *Phys Med Biol 50*, 3613-3625.

Sander, B., Golas, M.M., and Stark, H. (2003). Automatic CTF correction for single particles based upon multivariate statistical analysis of individual power spectra. *J Struct Biol 142*, 392-401.

Sanger, F., Nicklen, S., and Coulson, A.R. (1977). DNA sequencing with chain-terminating inhibitors. *Proc Natl Acad Sci U S A 74*, 5463-5467.

Saxena, K., Drosou, V., Maier, E., Benz, R., and Ludwig, B. (1999). Ion selectivity reversal and induction of voltage-gating by site-directed mutations in the *Paracoccus denitrificans* porin. *Biochemistry 38*, 2206-2212.

Schulz, G.E. (1993). Bacterial porins: structure and function. *Curr Opin Cell Biol 5*, 701-707.

Schuster, B., Pum, D., Braha, O., Bayley, H., and Sleytr, U.B. (1998). Self-assembled alpha-hemolysin pores in an S-layer-supported lipid bilayer. *Biochim Biophys Acta 1370*, 280-288.

Sen, K., Hellman, J., and Nikaido, H. (1988). Porin channels in intact cells of Escherichia coli are not affected by Donnan potentials across the outer membrane. *J Biol Chem 263*, 1182-1187.

Shi, S., Sun, S., Andrews, S.B., and Leapman, R.D. (1996). Thickness measurement of hydrated and dehydrated cryosections by EELS. *Microsc Res Tech 33*, 241-250.

Sigworth, F.J. (2004). Classical detection theory and the cryo-EM particle selection problem. *J Struct Bio*l *145*, 111-122.

Siroy, A., Mailaender, C., Harder, D., Koerber, S., Wolschendorf, F., Danilchanka, O., Wang, Y., Heinz, C., and Niederweis, M. (2008). Rv1698 of Mycobacterium tuberculosis represents a new class of channel-forming outer membrane proteins. *J Biol Chem 283*, 17827-17837.

Sitte, H. (1996). Advanced instrumentation and methodology related to cryoultramicrotomy: a review. *Scanning Microsc Supp*l *10*, 387-463; discussion 463-386.

Slot, J.W., and Geuze, H.J. (2007). Cryosectioning and immunolabeling. *Nat Protoc 2*, 2480-2491.

Snapper, S.B., Melton, R.E., Mustafa, S., Kieser, T., and Jacobs, W.R., Jr. (1990). Isolation and characterization of efficient plasmid transformation mutants of *Mycobacterium smegmatis. Mol Microbio*l *4*, 1911-1919.

Sorzano, C.O., Messaoudi, C., Eibauer, M., Bilbao-Castro, J.R., Hegerl, R., Nickell, S., Marco, S., and Carazo, J.M. (2009). Marker-free image registration of electron tomography tilt-series. *BMC Bioinformatics 10*, 124.

Stahl, C., Kubetzko, S., Kaps, I., Seeber, S., Engelhardt, H., and Niederweis, M. (2001). MspA provides the main hydrophilic pathway through the cell wall of Mycobacterium smegmatis. *Mol Microbiol 40*, 451-464.

Stephan, J., Bender, J., Wolschendorf, F., Hoffmann, C., Roth, E., Mailander, C., Engelhardt, H., and Niederweis, M. (2005). The growth rate of Mycobacterium smegmatis depends on sufficient porin-mediated influx of nutrients. *Mol Microbiol 58*, 714-730.

Stephan, J., Mailaender, C., Etienne, G., Daffe, M., and Niederweis, M. (2004a). Multidrug resistance of a porin deletion mutant of *Mycobacterium smegmatis. Antimicrob Agents Chemother 48*, 4163-4170.

Stephan, J., Stemmer, V., and Niederweis, M. (2004b). Consecutive gene deletions in Mycobacterium smegmatis using the yeast FLP recombinase. *Gene 343*, 181-190.

Stewart, P.L., Chiu, C.Y., Haley, D.A., Kong, L.B., and Schlessman, J.L. (1999). Review: resolution issues in single-particle reconstruction. *J Struct Biol 128*, 58-64.

Subramaniam, S., and Henderson, R. (2000). Molecular mechanism of vectorial proton translocation by bacteriorhodopsin. *Nature 406*, 653-657.

Taylor, K.A., and Glaeser, R.M. (1974). Electron diffraction of frozen, hydrated protein crystals. *Science 186*, 1036-1037.

Thomas, D., Morgan, D.G., and DeRosier, D.J. (2001). Structures of bacterial flagellar motors from two FliF-FliG gene fusion mutants. *J Bacteriol 183*, 6404-6412.

Toyoshima, C., and Unwin, N. (1988). Contrast transfer for frozen-hydrated specimens: determination from pairs of defocused images. *Ultramicroscopy 25*, 279-291.

Trias, J., and Benz, R. (1993). Characterization of the channel formed by the mycobacterial porin in lipid bilayer membranes. Demonstration of voltage gating and of negative point charges at the channel mouth. *J Biol Chem 268*, 6234-6240.

Trias, J., and Benz, R. (1994). Permeability of the cell wall of Mycobacterium smegmatis. *Mol Microbiol 14*, 283-290.

Trias, J., Jarlier, V., and Benz, R. (1992). Porins in the cell wall of mycobacteria. *Science 258*, 1479-1481.

van Duinen, G., van Heel, M., and Patwardhan, A. (2005). Magnification variations due to illumination curvature and object defocus in transmission electron microscopy. *Opt Express 13*, 9085-9093.

Varadhachary, A., and Maloney, P.C. (1990). A rapid method for reconstitution of bacterial membrane proteins. *Mol Microbiol 4*, 1407-1411.

Villeneuve, M., Kawai, M., Kanashima, H., Watanabe, M., Minnikin, D.E., and Nakahara, H. (2005). Temperature dependence of the Langmuir monolayer packing of mycolic acids from Mycobacterium tuberculosis. *Biochim Biophys Acta 1715*, 71-80.

Villeneuve, M., Kawai, M., Watanabe, M., Aoyagi, Y., Hitotsuyanagi, Y., Takeya, K., Gouda, H., Hirono, S., Minnikin, D.E., and Nakahara, H. (2007). Conformational behavior of oxygenated mycobacterial mycolic acids from *Mycobacterium bovis* BCG. *Biochim Biophys Acta 1768*, 1717-1726.

Volkert, C.A., and Minor, A.M. (2007). Focused ion beam microscopy and micromachining. *Mrs Bulletin 32*, 389-395.

Waltermann, M., and Steinbüchel, A. (2005). Neutral lipid bodies in prokaryotes: recent insights into structure, formation, and relationship to eukaryotic lipid depots. *J Bacteriol 187*, 3607-3619.

Walz, T., Typke, D., Smith, B.L., Agre, P., and Engel, A. (1995). Projection map of aquaporin-1 determined by electron crystallography. *Nat Struct Biol 2*, 730-732.

Wang, L., and Sigworth, F.J. (2009). Structure of the BK potassium channel in a lipid membrane from electron cryomicroscopy. *Nature 461*, 292-295.

Wang, L., Slayden, R.A., Barry, C.E., 3rd, and Liu, J. (2000). Cell wall structure of a mutant of Mycobacterium smegmatis defective in the biosynthesis of mycolic acids. *J Biol Chem 275*, 7224-7229.

Watanabe, M., Aoyagi, Y., Mitome, H., Fujita, T., Naoki, H., Ridell, M., and Minnikin, D.E. (2002). Location of functional groups in mycobacterial meromycolate chains; the recognition of new structural principles in mycolic acids. *Microbiology 148*, 1881-1902.

Wayne, L.G., and Hayes, L.G. (1996). An in vitro model for sequential study of shiftdown of *Mycobacterium tuberculosis* through two stages of nonreplicating persistence. *Infect Immun 64*, 2062-2069.

White, D.L., Andrews, S.B., Faller, J.W., and Barrnett, R.J. (1976). The chemical nature of osmium tetroxide fixation and staining og membranes by X-ray photoelectron spectroscopy. *Biochim Biophys Acta 463*, 577-592.

WHO (2006). Tuberculosis fact sheet N°104.

WHO (2009). Global tuberculosis control - epidemiology, strategy, financing. WHO report 2009.

Winkler, H., and Taylor, K.A. (2003). Focus gradient correction applied to tilt series image data used in electron tomography. *J Struct Biol 143*, 24-32.

Wolschendorf, F., Mahfoud, M., and Niederweis, M. (2007). Porins are required for uptake of phosphates by *Mycobacterium smegmatis*. *J Bacteriol 189*, 2435-2442.

Xiong, Q., Morphew, M.K., Schwartz, C.L., Hoenger, A.H., and Mastronarde, D.N. (2009). CTF determination and correction for low dose tomographic tilt series. *J Struct Biol 168*, 378-387.

Zanetti, G., Riches, J.D., Fuller, S.D., and Briggs, J.A. (2009). Contrast transfer function correction applied to cryo-electron tomography and sub-tomogram averaging. *J Struct Biol 168*, 305-312.

Zhang, P., Bos, E., Heymann, J., Gnaegi, H., Kessel, M., Peters, P.J., and Subramaniam, S. (2004). Direct visualization of receptor arrays in frozen-hydrated sections and plunge-frozen specimens of E. coli engineered to overproduce the chemotaxis receptor Tsr. *J Microsc 216*, 76-83.

Zhu, J., Penczek, P.A., Schroder, R., and Frank, J. (1997). Three-dimensional reconstruction with contrast transfer function correction from energy-filtered cryoelectron micrographs: procedure and application to the 70S Escherichia coli ribosome. *J Struct Biol 118*, 197-219.

Zuber, B., Chami, M., Houssin, C., Dubochet, J., Griffiths, G., and Daffe, M. (2008). Direct visualization of the outer membrane of mycobacteria and corynebacteria in their native state. *J Bacteriol 190*, 5672-5680.

Zuber, B., Nikonenko, I., Klauser, P., Muller, D., and Dubochet, J. (2005). The mammalian central nervous synaptic cleft contains a high density of periodically organized complexes. *Proc Natl Acad Sci U S A 102*, 19192-19197.

Danksagung

Die vorliegende Arbeit wurde von Januar 2006 bis April 2010 in der Abteilung Molekulare Strukturbiologie des Max-Planck-Institutes für Biochemie, Martinsried, durchgeführt. Ich möchte mich bei allen Mitgliedern der Abteilung für das gute Arbeitsklima bedanken.

Herrn Prof. Dr. Wolfgang Baumeister danke ich für die Möglichkeit, meine Promotion in seiner Abteilung anfertigen zu können.

Mein besonderer Dank gilt Herrn Dr. Engelhardt für die stets hervorragende Betreuung dieser Arbeit, seinen wissenschaftlichen Rat und sein motivierendes, unerschütterliches Gemüt. In gleicher Weise möchte ich mich bei Herrn Dr. Jürgen Plitzko für die Betreuung des technischen Teils dieser Arbeit bedanken, für die Hilfe bei der Lösung von zahlreichen Problemen an den Elektronenmikroskopen und die vielen Diskussionen, auch nach ‚Dienstschluss‘.

Mathias Eibauer möchte ich für die großartige Zusammenarbeit während des CTF-Korrektur-Projekts danken. Für seine Geduld beim erklären der Algorithmen und die ausführlichen Dokumentationen seiner Programme, sowie zahllose interessante Diskussionen.

Großer Dank gilt auch Günter Pfeifer für die Unterstützung bei der Datenaufnahme in der initialen Phase der Arbeit und Andrew Leis für das Beibringen des Cryoschneidens.

Alex Rigort und Felix Bäuerlein danke ich für das Anfertigen der FIB-Proben, Inga Wolf, Florian Beck und Stefan Nickell für ihre Hilfe bei zahlreichen Computerproblemen.

Danke auch an meinen Büronachbarn Jan Lubieniecki für seine Hilfe im Labor.

Parul Garg, Alina Levchuk und Raphael Roccor danke ich für ihre Mitarbeit bei der Konstruktion der MspA-Mutanten.

Besonderer Dank gilt auch der Firma Nanion, vor allem Mohamed Kreir und Niels Fertig für die enorme Unterstützung bei den Leitfähigkeitsmessungen.

Großer Dank auch an die Mitglieder der Werkstatt der Abteilung Molekulare Strukturbiologie, Rudolf Gatz, Tim Laugks, Thomas Matthes, Manfred Baumgartner und Alexander Schwarz, für die Anfertigung mehrerer Bestandteile von Versuchsaufbauten, sowie die Ratschläge bei so manchem ‚Heimwerkerproblem'.

Danke auch den vielen anderen, für die unzähligen kleinen Dinge: Florian Brandt, Karoline Bopp, Manuela Gruska, Ulrike Maurer, Christoph Hagen, Dennis Thomas, Andreas Korinek, Kay Grünewald, Stefan Bohn, Birgit Book, Lars-Anders Carlson, Sarah Breuer, Leonie Waanders, Juha Huiskoonen, Christine Kofler, Oana Mihalache, Ruben Fernandez, Elke Glasmacher, Roland Knispel, Michael Niederweis, Reiner Hegerl, Sabina von Polenz, Andreas Sonnen, Nina Hubner, Wiliam Delnet, Radosav Pantelic

Danke an Alina für ihre Nachsicht, Motivation, das Korrekturlesen und so vieles mehr.

Am meisten Danke ich meinen Eltern, die mir meine gesamte Ausbildung ermöglicht haben und mich in deren Verlauf unentwegt gefördert haben.

Publications:

Hoffmann, C., Leis, A., Niederweis, M., Plitzko, J.M., and Engelhardt, H. (2008). Disclosure of the mycobacterial outer membrane: cryo-electron tomography and vitreous sections reveal the lipid bilayer structure. *Proc Natl Acad Sci U S A 105*, 3963-3967.

Rigort, A., Bauerlein, F.J., Leis, A., Gruska, M., Hoffmann, C., Laugks, T., Bohm, U., Eibauer, M., Gnaegi, H., Baumeister, W., *et al.* (2010). Micromachining tools and correlative approaches for cellular cryo-electron tomography. *J Struct Biol.*

Niederweis, M., Danilchanka, O., Huff, J., Hoffmann, C., Engelhardt, H. (2010). Mycobacterial outer membranes: in search of proteins. *Trends Microbiol. 18,* 109-116.